Gas-Condensate Flow Modelling for Shale Gas Reservoirs

Ismail Labed

A thesis submitted in partial fulfilment of the requirements of the

Robert Gordon University

for the degree of Doctor of Philosophy

October 2016

ABSTRACT

In the last decade, shale reservoirs emerged as one of the fast growing hydrocarbon resources in the world unlocking vast reserves and reshaping the landscape of the oil and gas global market. Gas-condensate reservoirs represent an important part of these resources. The key feature of these reservoirs is the condensate banking which reduces significantly the well deliverability when the condensate forms in the reservoir below the dew point pressure. Although the condensate banking is a well-known problem in conventional reservoirs, the very low permeability of shale matrix and unavailability of proven pressure maintenance techniques make it more challenging in shale reservoirs.

The nanoscale range of the pore size in the shale matrix affects the gas flow which deviates from laminar Darcy flow to Knudsen flow resulting in enhanced gas permeability. Furthermore, the phase behaviour of gas-condensate fluids is affected by the high capillary pressure in the matrix causing higher condensate saturation than in bulk conditions. A good understanding and an accurate evaluation of how the condensate builds up in the reservoir and how it affects the gas flow is very important to manage successfully the development of these high-cost hydrocarbon resources.

This work investigates the gas Knudsen flow under condensate saturation effect and phase behaviour deviation under capillary pressure of gas-condensate fluids in shale matrix with pore size distribution; and evaluates their effect on well productivity.

Knudsen flow in shale matrix under the effect of condensate saturation is investigated using pore network modelling with a random log-normal pore size distribution. The multi-scale gas flow model of Beskok-Karniadakis was used to model the gas flow in shale pore level and the apparent gas permeability was calculated for the whole network. A new parameter, "Relative Correction Factor" defined as the ratio of Knudsen dry gas permeability to Knudsen gas-condensate permeability, was introduced to evaluate the change of condensate saturation effect on Knudsen flow.

The phase behaviour of gas-condensate fluids in shale matrix was examined through combination of modified Peng-Robinson Equation of State (PREOS) and pore size distribution. An iterative algorithm is used to model the interaction of EOS and capillary pressure as a function of pore size distribution and to provide dew point and condensate saturation calculation in Constant Volume Depletion (CVD) simulations.

The performance of shale gas-condensate reservoirs was studied using a semi-analytical model in Laplace domain of single matrix block with constant fracture pressure. The Knudsen effect under two-phase flow and phase behaviour deviation were incorporated to this model. In addition, numerical compositional simulation was used to investigate the whole matrix-fracture system using logarithmic grid refinement technique.

Results showed that Knudsen flow under condensate banking effect is not only a function of condensate saturation; it is also affected by pressure and pore size distribution. The reduction of Knudsen flow under condensate banking is higher at low pressure and in more dispersed pore size distribution (at high standard deviation values). The semi-analytical models showed that the effect of condensate saturation and pressure is significant (about 25% of the production gained by Knudsen flow). Hence, assumption of a constant mean effective pore size in gas apparent permeability calculation in shale matrix with condensate banking results in overestimation of Knudsen flow contribution in well productivity.

The phase behaviour calculation showed a significant impact of the pore size distribution on dew point and condensate drop out. In addition, the phase behaviour deviation is more pronounced in lean condensates than rich condensate due to the lower pore size at which the gas-condensate interface forms resulting in a higher capillary pressure. Furthermore, using a single pore radius leads to inaccurate estimation of phase behaviour deviation (lower for lean condensate and higher for rich condensate). The effect of this phase behaviour on well deliverability can cause a moderate production loss from 2.5% to 5%.

As result, it is highly recommended that the analysis of pore structure and distribution of shale matrix are incorporated into the reservoir evaluation workflow on a routine basis during exploration and development phases of shale gas-condensate reservoirs. Thus, the apparent gas permeability under reservoir conditions in terms of pressure and condensate saturation and the phase behaviour deviation can be predicted accurately.

This thesis contributes to the existing knowledge of gas-condensate reservoir engineering by improving the understanding and proposing a new modelling approaches of gas-condensate flow behaviour and phase behaviour in shale matrix. The effect of condensate saturation and pressure on Knudsen enhanced permeability is identified and formulated using 3D pore network modeling. Besides, a new modeling approach of phase behaviour deviation in a pore size distribution using PREOS is introduced in this work where the effect of pore sizes variation on phase behaviour is incorporated more accurately than the average pore size model.

DEDICATION

This thesis work is dedicated to my parents, Cheikh and Yamina, my wife, Ahlem and my daughter, Marwa for their endless love and support during my study years.

ACKNOWLEDGEMENTS

Firstly, I would like to express my sincere gratitude to Professor Babs Oyeneyin of the School of Engineering in Robert Gordon University, for the continuous support of my PhD study and related research, for his patience, motivation, and immense knowledge. His guidance helped me in all the time of research and writing of this thesis. My sincere thanks also goes to Dr Gbenga Oluyemi Lecturer in the School of Engineering, RGU, for his insightful comments and encouragement.

I thank my colleagues from school of engineering specially Favour, Slimane, Reza, Hussein and Kelani for the stimulating discussions and for all the fun we have had in the last four years.

I would also like to take this opportunity to thank the Aberdeen Formation Evaluation Society (AFES) for the partial funding of this PhD and all the AFES members specially Dr Giancarlo Rizzi for their priceless feedback and comments during my presentations at the AFES.

I am also indebted to my colleagues Laurent Schirrer and Isabelle Vervoort from Oilgen in Aberdeen for their continuous encouragement.

Special thanks go to my brothers, sisters, my mother and father for their prayers and encouragement. I would also like to thank all my family-in-law who provided my family with support and reassurance. At the end I would like express appreciation to my beloved wife Ahlem and my little princess Marwa who were always my support in the difficult moments.

Ismail Labed

TABLE OF CONTENTS

LIST OF TABLES

LIST OF FIGURES

NOMENCLATURE

Symbols

b	:	Empirical slip coefficient
C_f	:	Hydraulic fracture conductivity, md.ft
C_g	:	Langmuir gas content, scf/ton
C_m^{δ}	:	Class Contribution in gas flow
c_f	:	Compressibility factor, psi^{-1}
D_i	:	Nominal decline rate
f_{ic}	:	Fugacity of condensate for a component i, psi
f_{ig}	:	Fugacity of gas for a component i, psi
f	:	Probability density function of long-normal distribution
G_{ij}^{c}	:	Condensate conductivity of nanotube ij
G_{ij}^{g}	:	Gas conductivity of nanotube ij
I_0 and I_1	:	Modified Bessel functions
K_i	:	Equilibrium ratio
k_{∞}	:	Intrinsic permeability, mD
$k_{D,GC}$	:	Darcy permeability with condensate blockage, mD
k_D	:	Darcy pore network permeability, mD
$k_{app,GC}$	:	Knudsen permeability with condensate blockage, mD
k_{app}	:	Apparent permeability, mD
$k_{eff.g}$	:	Gas effective permeability, mD
k_f	:	Fracture permeability, mD
k_{rg}	:	Darcy relative permeability
Kn	:	Knudsen number
L	:	Channel length, m

M	:	Average molecular mass, kg/kmol
n, a and b	:	Pore distribution parameters of ξ_{rel} model
P_D	:	Dimensionless pseudo-pressure
P_L	:	Langmuir pressure, psi
P_c	:	Pressure in condensate phase, psi
P_{cap}	:	Capillary pressure, psi
P_d	:	Dew point pressure, psi
P_g	:	Pressure in gas phase, psi
P_i	:	Pore network inlet pressure, psi
P_o	:	Pore network outlet pressure, psi
P	:	Reservoir pressure, psi
$P(p)$	:	Pseudo-pressure, psi^2/cp
q_{app}	:	Apparent gas flowrate, Mscf/d
R_{avg}	:	Average pore size, m
R_{eff}	:	Effective average pore size, m
R_{max}	:	Maximum pore size, m
R_{min}	:	Minimum pore size, m
r_D	:	Dimensionless coordinate, r-direction
r_e	:	Matrix radius of equivalent matrix cross section, ft
Rg	:	Universal gas constant = 8314 J/kmol/K
$R_{g,min}$	:	Gas minimum pore size, m
R	:	Nanotube hydraulic radius, m
r	:	Radial coordinate, ft
S_c	:	Condensate saturation
s	:	Standard deviation of log-normal distribution
t_D	:	Dimensionless time
T	:	Reservoir temperature, K

t : Time, days

V_L : Langmuir volume, scf/ton

V_{rel} : Condensate relative volume

w_∞ : Intrinsic fracture width, ft

w_{eff} : Effective fracture width, ft

x_e : Matrix block dimension in X-direction, ft

x_i : Mole fraction of component i in condensate

y_e : Matrix block dimension in Y-direction, ft

y_i : Mole fraction of component i in gas

Z : Gas compressibility factor

Greek Symbols

ΔC_m : Relative Chang Class Contribution in gas flow

ΔP : Pressure difference, psi

ΔP_{thr} : Differential pressure threshold

α : Dimensionless rarefaction coefficient

α : Biot's coefficient

β : Forchheimer parameter

β_∞ : intrinsic Forchheimer parameter

β_{eff} : Effective fracture Forchheimer parameter

ε_f : Equilibrium error tolerance

ε_σ : IFT error tolerance

η : Diffusivity constant

θ : Gas-condensate contact angle

μ : Fluid viscosity, cp

μ_{avg} : Pore network average viscosity

v : Mean of log-normal distribution

λ : Average minimum free path, nm

ξ : Micro channels correction factor

ξ_{DG} : Enhancement factor for dry gas

ξ_{rel} : Relative Correction Factor

ρ_c : Condensate molar density

ρ_g : Gas molar density

σ_{eff} : Effective stress, psi

σ_{gc} : Gas-condensate interfacial tension

σ_n : Normal stress σ_n, psi

τ : Tortuosity

ϕ : Rock porosity

ϕ_{ic} : Fugacity coefficient of condensate for a component i

ϕ_{ig} : Fugacity coefficient of gas for a component i

Subscripts

∞ : Intrinsic property

c : Condensate

cap : Capillary

DG : Dry gas

eff : Effective

f : Fracture

gc : Gas-condensate

g : Gas

i : Integer from 1 to N

CHAPTER 1: INTRODUCTION

1.1 Background

In the last decade, shale plays emerged as one of the most important oil and gas resources in the world. As at 2014, shale gas accounted for 51% of all US natural gas reserves (EIA 2015). Shale reservoirs are characterised by very small pore size (from 3 to 100 nm) and a very low matrix permeability which ranges in nano-Darcy. Hydraulic fracturing is required to make this type of resources commercially valuable.

The gas-condensate flow in hydrocarbon reservoirs has long been recognized as having the most complex fluid flow dynamics in reservoir engineering (Hinchman and Barree 1985, Barnum, et al. 1995, Du, Guan and Bai 2004). A condensate buildup can rapidly occur around a producing well when the bottom hole flowing pressure falls below dew-point. The condensate accumulation reduces the gas relative permeability resulting in a brisk decline of well productivity and reduction of heavy components fraction at the wellhead. This phenomenon is usually referred to as condensate banking or condensate blockage. The condensate banking is controlled by three factors: the flow behaviour, the phase behaviour and the development strategy.

The flow behaviour represents the interaction of gas-condensate flow with condensate saturation in the reservoir. The phase behaviour consists of the variation of the PVT properties of gas-condensate (dew point, condensate saturation and phases molecular composition) fluids as function of fluid composition and reservoir conditions (pressure and temperature). The development strategy is defined by the drilling and completion practices and the production control of the well.

In conventional reservoirs, the condensate banking effect can be alleviated by pressure maintenance to be able to produce at a bottomhole pressure above the dew point. In shale reservoirs, due to the very low permeability, wells start to produce under a bottomhole pressure below the dew point in the few first days or months of production. As no method is available to maintain pressure in shale reservoirs, this type of resources remains producing under condensate banking effect for all production period.

1.2 The Knowledge Gap in Shale Gas-Condensate Reservoir Engineering

After a decade of extensive development of shale reservoirs in the US and Canada, gas-condensate flow in shale matrix still represents a basic scientific question. The key points of the knowledge gap in shale gas-condensate reservoir engineering can be addressed in terms of the three factors that control the condensate banking phenomena as discussed in the following Sections.

1.2.1 Multiphase Flow Behaviour in Shale Matrix

In conventional reservoirs, the effect of condensate banking on gas flow is interpreted by using relative permeability models. The apparent gas permeability at a condensate saturation is adjusted using the gas relative permeability as a correction factor.

However, in shale reservoirs at the nanopore level, the gas flow deviates from conventional Darcy flow to Knudsen flow resulting in an enhanced apparent gas permeability. The Knudsen flow is well-established theory in fluid dynamics (Steckelmacher 1986) and it is mainly applied for single phase gas flow in fabricated micro and nano-channels with applications ranging from membrane gases separation to MEMS (Microelectromechanical systems) (Koros and Fleming 1993, Copic 2008).

For shale gas reservoir engineering, although the dry gas flow under Knudsen conditions in shale matrix has been the subject of numerous research studies (Javadpour 2009, Civan 2010, Freeman, et al. 2012, Mehmani, Prodanović and Javadpour 2013), the effect of multiphase gas-condensate flow is still not well addressed in terms of the effect of condense saturation on the apparent gas permeability. As Knudsen flow is highly dependent on pore size, the effect of condensate accumulation alters the range of pore sizes that are accessible by gas flow which affects Knudsen flow at the macroscale level. Therefore, the understanding of how Knudsen flow is affected by condensate banking is essential to evaluate accurately the shale gas-condensate well performance. Using the dry gas Knudsen flow models can lead to an overestimation of recovery of wells under the condensate banking effect.

1.2.2 Phase Behaviour in Shale Matrix

For PVT calculation in conventional reservoirs, the difference of pressure between liquid and pressure at pore level under capillary forces effect is not taken into consideration when applying Equation of State (EOS) as its effect is assumed to be insignificant (Sigmund et al.

1973). Results from PVT experiments in laboratory at bulk condition (i.e. no capillary pressure) are routinely used to tune the EOS for compositional reservoir simulations.

Conversely, in shale gas condensate reservoirs, phase behaviour deviation due to capillary condensation in nanopore shale matrix is a key factor for reserves estimation and well performance calculation. The condensate starts forming in matrix nanopores at higher pressure and reaches higher saturation levels than at bulk conditions. The phenomenon has been investigated theoretically in the past using single nanotube with average pore radius as an equivalent of shale matrix (Brusilovsky 1992, Espósito, Tavares and Castier 2005, Firincioglu, Ozkan and Ozgen 2012, Pang, et al. 2013, Nojabaei, Johns and Chu 2013, Jin and Firoozabadi 2015). Nevertheless, different pore sizes in shale matrix exhibit different phase behaviour deviation as the capillary pressure depends on pore radius. Thus, different pore sizes contribute differently to the macroscale phase behaviour. In order to improve the modelling of phase behaviour deviation of gas-condensate fluids in shale matrix, it is essential to represent the porous media in terms of their pore size distribution instead of the average pore radius.

1.2.3 Performance of Shale Gas-Condensate Reservoirs

As mentioned in Sections 1.2.1 and 1.2.2, the shale gas-condensate reservoirs are characterised by deviation of flow behaviour and phase behaviour compared to conventional reservoirs. The evaluation of effect of this deviation on well performance is imperative to achieve an accurate prediction of ultimate well recovery.

Moreover, the development strategy of shale wells is different from that of conventional wells. Conventional reservoirs are developed using vertical, deviated or horizontal wells with or without vertical hydraulic fracture. The multistage hydraulic fracturing combined with horizontal well in shale well development creates separate matrix blocks resulting into two porous media with several magnitude difference of permeability. As a result, the condensate generation and propagation is more complex than in conventional wells; this needs to be well addressed and assessed.

1.3 Research Objectives

This thesis aims to provide an improved modelling of gas-condensate flow and phase behaviour in shale matrix with focus on the condensate banking effect through the following objectives:

- To model the enhanced gas permeability by the Knudsen flow under the effect of condensate situation in the shale matrix with pore size distribution and to develop a formulation of Knudsen flow in gas-condensate two phase flow.
- To investigate the key parameters that control the reduction of Knudsen flow as function of condensate saturation.
- To model the phase behaviour deviation of gas-condensate fluids under the capillary pressure effect in shale matrix with pore size distribution and to determine the impact of pore size distribution on the phase behaviour deviation.
- To evaluate the condensate saturation, Knudsen flow and phase behaviour deviation on shale gas-condensate well performance.
- To investigate the accumulation and propagation of condensate banking in multistage fractured horizontal well and how it affects the well productivity.

1.4 Research Approach

The research initially started with reviewing published data of shale reservoirs characteristics and current development practices in the shale industry. A literature review of the research in flow behaviour and phase behaviour was conducted as the subject is one of the most active research areas in petroleum engineering. Relevant research studies from material science multiphase flow and PVT in nanotubes were investigated for possible adoption in the shale gas condensate reservoir modelling.

The gas-condensate flow in shale matrix was investigated numerically by using pore network modelling. The pore network was modelled using log-normal pore size distribution and Knudsen flow was used to model gas flow in individual pores. A code was developed in Matlab to solve the equations system. The apparent gas permeability under different flow types; Darcy and Knudsen was calculated for the whole pore network. The effect of condensate banking on Knudsen flow was evaluated and a relative correction factor was proposed to assess the relationship between Knudsen flow and condensate saturation. The effect of pore size distribution on the relative correction factor was investigated by running numerical simulations with varying log-normal distribution in terms of mean (v) and standard deviation (s).

The phase behaviour deviation of gas-condensate fluids in shale matrix was evaluated using a pore size distribution and modified Peng-Robinson equation of state. The VLE (Vapour Liquid Equilibrium) calculation was modelled at the nanotube scale using different gas and

condensate pressure as a function of the capillary pressure. The macro-scale phase behaviour was calculated by upscaling the PVT results (e.g. dew point and condensate saturation) from nanotube to pore network using the log-normal distribution. The CVD (Constant Volume Depletion) experiment under capillary pressure effect was simulated and compared to bulk CVD in order to evaluate the phase behaviour deviation. The effect of pore size distribution on the phase behaviour deviation was investigated as well and compared to the single tube method (where pore network is simplified into a single tube with average pore radius). In addition, the phase behaviour deviation of rich condensate versus lean condensate is compared.

The effect of both flow behaviour deviation and phase behaviour deviation of gas-condensate fluids on the well performance was investigated using a semi-numerical model of a single shale matrix block. The fluid flow in the matrix from the centre to the edge which is in contact with fracture at constant pressure. The model equation was solved in Laplace domain which is capable of reflecting both transient and pseudo-steady states in the matrix. As the flow behaviour deviation and the phase behaviour occur only in the shale matrix, it was assumed that this model results were representative of how the deviation affect the well proactivity.

In order to understand the interaction between the matrix and hydraulic fracture, numerical compositional simulator was used to investigate how the condensate banking generates and propagates in the reservoir and how it affects the well productivity. The commercial software package does not include the flow behaviour and phase behaviour models presented in this work but it provides a basic understanding of the performance of shale gas-condensate wells.

Furthermore, the well design optimisation in terms of the hydraulic fracture spacing was addressed using numerical simulation and economic evaluation with a view to maximizing the NPV (Net Present Value) of the asset.

1.5 Contributions to Knowledge

This work has made substantial contributions to the subject of shale gas-condensate reservoir engineering. These contributions are discussed in the following Sections:

1.5.1 Knudsen Flow Under Condensate Banking Effect

This work proposed a pore network modelling of Knudsen flow reduction under condensate banking. The concept relative permeability in Darcy flow was extended to Knudsen flow by

introducing a new parameters called "*Relative Correction Factor*" (ξ_{rel}). The new parameters can be easily introduced in reservoir engineering tools to calculate the gas effective permeability $k_{eff.g}$ as function of saturation and pressure.

$$k_{eff.g}(S_c, P) = \xi_{rel}\, \xi_{DG}\, k_{rg}\, k_{\infty} \tag{1.1}$$

where S_c is condensate saturation, P is the reservoir pressure, ξ_{DG} is the correction factor for dry gas Knudsen flow, k_{rg} is Darcy relative permeability for Darcy flow and k_{∞} is the intrinsic permeability.

ξ_{rel} can be incorporated directly into the existing reservoir engineering tools to correct the gas apparent permeability under Knudsen flow and condensate banking saturation.

The output of this work demonstrated that ξ_{rel} is not only a function of condensate saturation but also reservoir pressure and pore size distribution. While the condensate saturation controls the effective pore size of gas Knudsen flow, pressure affects the degree of contribution of each pore size range. This relationship can be formulated as

$$\xi_{rel} = 1 - \frac{a}{P^b}\,(S_c)^n \tag{1.2}$$

where n, a and b are parameters of the pore distribution which can be determined theoretically by pore network modelling.

These findings can be extended to the gas-water flow in shale matrix where the variation of water saturation in the reservoir generates similar effect on Knudsen flow.

1.5.2 Phase Behaviour in Shale Matrix

This work proposed a new modelling of phase behaviour of gas-condensate fluids in shale matrix which takes into consideration the pore size distribution. The results of this model demonstrated the effect of pore size distribution on phase behaviour deviation under the effect of capillary pressure. Numerical CVD simulations showed that the deviation in lean condensate is more pronounced than in rich condensate due to effect of changing pore radius of gas-condensate interphase. Furthermore, these simulations showed that use of single pore radius to evaluate the phase behaviour deviation can lead into an inaccurate estimation of phase behaviour in terms of dew point and condensate saturation.

1.5.3 Shale Gas-Condensate Well Performance

This study contributes to the existing understanding of the performance of shale gas-condensate wells by examining the effect of flow behaviour and phase behaviour deviation

on well production. This study revealed the importance of taking into consideration the effect of condensate banking on Knudsen flow and how significantly it affects the well production calculation. Knudsen flow minimises the negative effect of condensate banking, the correction of Knudsen flow to the effect of condensate saturation and pressure should be taken into consideration to not overestimate its contribution to the well production.

Moreover, this work concluded that although the high capillary pressure in shale matrix induces the phase behaviour deviation of gas-condensate fluids resulting in higher dew point and higher condensate saturation, its effect on the well recovery is limited (less than 5%).

1.6 Arrangement of Thesis

Chapter 1 provides a brief presentation of the research background, the knowledge gap in shale gas-condensate reservoir engineering, the project objectives and the approach adopted.

Chapter 2 provides an overview of shale resources and presents the key shale reservoirs characteristics such as Total Organic Matter (TOC), porosity structure and permeability. In addition, current drilling and completion practices in shale reservoir development, drive mechanism and recovery factor levels are reviewed.

Chapter 3 covers the flow behaviour modelling of gas-condensate fluids in shale matrix. It starts with the review of the gas and liquid flow in nanotubes separately. Previous work on liquid saturation effect on slip/Knudsen flow is also reviewed. The second part of Chapter 3 presents the modelling of gas condensate flow through pore network modelling with random pore radius distribution with log-normal law. The Knudsen flow was used to model gas flow in nanotube and macroscale permeability was calculated by solving the flow equation. Moreover, Chapter 3 provides the simulation results in terms condensate trapping, effect of condensate saturation on gas apparent permeability and the effect of pore size distribution on relative correction factor.

0 describes the modelling of phase behaviour deviation of condensate in shale matrix using modified Peng-Robinson EOS. It provides the developed algorithms for the numerical CVD simulation in pore network. Additionally, it discusses the effect of capillary pressure and pore size distribution on condensate drop out in CVD experiments.

Chapter 5 includes a gas-condensate flow model in single block of shale matrix with the integration of results from Chapter 3 and 0. This chapter describes the model used to study

the effect of condensate banking, Knudsen flow and deviated phase behaviour on shale matrix performance.

Chapter 6 investigates the performance of shale gas-condensate wells through 3D numerical reservoir simulation. It starts with a review of the limitations of the available reservoir engineering tools for shale gas-condensate well performance evaluation including Decline Curve Analysis (DCA), semi-analytical models and 3D numerical reservoir simulations. The key features of the numerical model of ¼ SRV (Stimulated Reservoir Volume) are described. The numerical simulation results are discussed in terms of condensate banking propagation and its effect on productivity, the effect of Non-Darcy flow and the stress-dependent permeability effect. The hydraulic fracture spacing optimisation using numerical simulation results and economic calculation are also presented in this Chapter.

Chapter 7 summarises the key findings of the research and its contributions to knowledge in shale gas-condensate reservoir engineering and presents the recommendations for the development of shale gas-condensate resources. In Chapter 8, the suggestions for future research are proposed in order to continue the improvement of the modelling of gas–condensate flow in shale reservoirs.

CHAPTER 2: REVIEW OF GAS CONDENSATE SHALE RESERVOIRS

2.1 Introduction

For a long time, shale formations were considered only as source rocks for hydrocarbon systems and they were rarely targeted for hydrocarbon production due to their very low permeability. In the past decade shale plays emerged in the US and Canada thanks to horizontal drilling and multistage fracturing technologies. In spite of shale industry success in North America, the cost of extraction remains one of the highest among oil and gas resources where fields are developed with industrial drilling; i.e. replicating the same well design for the whole field. The main reason behind this approach is the lack of understanding of shale reservoirs performance where the rock fabric, pore system, storage, flow behaviour and phase behaviour are different from conventional sandstone and carbonate reservoirs.

For shale gas-condensate reservoirs, condensate banking effect adds more complexity to the problem. Good understating of well performance and customised well design optimisation and production strategy are therefore key to economic development of shale plays.

This chapter aims to review the shale reservoir characteristics in terms of fluid storage and fluid flow that make shale resources different from the other reservoirs. More comprehensive review of flow behaviour and phase behaviour are carried out in Chapters 3 and 4. On the other hand, development strategies and reservoir mechanisms are reviewed in order to understand how the shale matrix interacts with hydraulic fracture and wellbore. Thus an appropriate modelling of shale matrix and well derivability is completed in Chapter 5 and Chapter 6 respectively.

2.2 Shale Resources

2.2.1 Shale Formations

Shale is the most common sedimentary rock. It is a fine-grained rock composed mainly of clay-sized particles and silt-sized particle (Speight 2013, Schön 2011). Shale rocks show fine

bedding from mm-scale to cm-scale and they are more laminated and fissile than sandstones and carbonates and readily splits in thin sheets (Tucker 2009). Figure 2.1 illustrates an example of core photos of a fine layered shale compared to a clean sandstone.

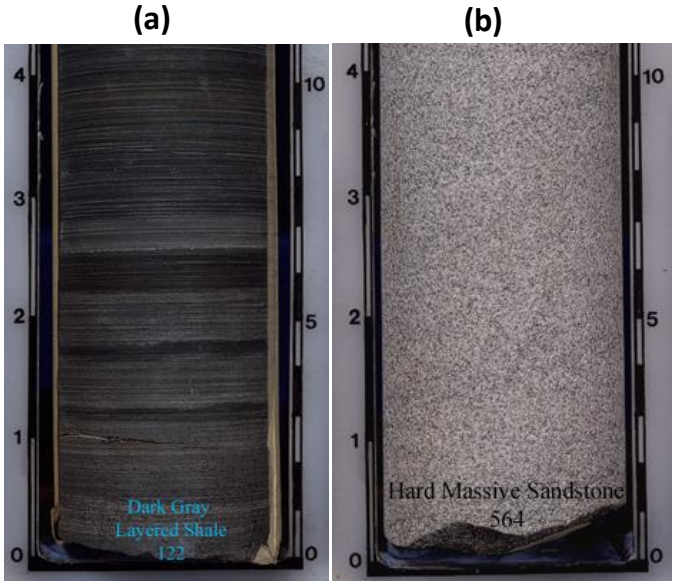

Figure 2.1: Photos of core examples of a) layered dark grey shale rock and b) hard sandstone (source: University of Kentucky)

There are two types of shale; the dark organic-rich and the light organic-lean. Dark shale formations were deposited in low or no oxygen conditions preserving organic material from decay. Under high pressure and high temperature, hydrocarbons were generated in the shale formation called *source rock* and small volume of these hydrocarbons were expelled and migrated upward to sandstones or carbonate formation known as *Conventional Reservoirs*. When a shale formation is produced economically using horizontal drilling and hydraulic fracturing it becomes a source rock and reservoir rock at the same time known as *shale reservoir*. Shale reservoirs along with coal bed methane and tight gas are named *Unconventional Reservoirs*.

Unlike conventional reservoirs, shale reservoirs are continuous auto-trap formations (see Figure 2.2). Usually, shale reservoirs are associated with low exploration risk due to their geographic extent however they exhibit a high horizontal heterogeneity where sweet spots are related to high productivity. The water contact is absent and water is present mainly as capillary-bound and clay-bound water (Passey et al. 2010).

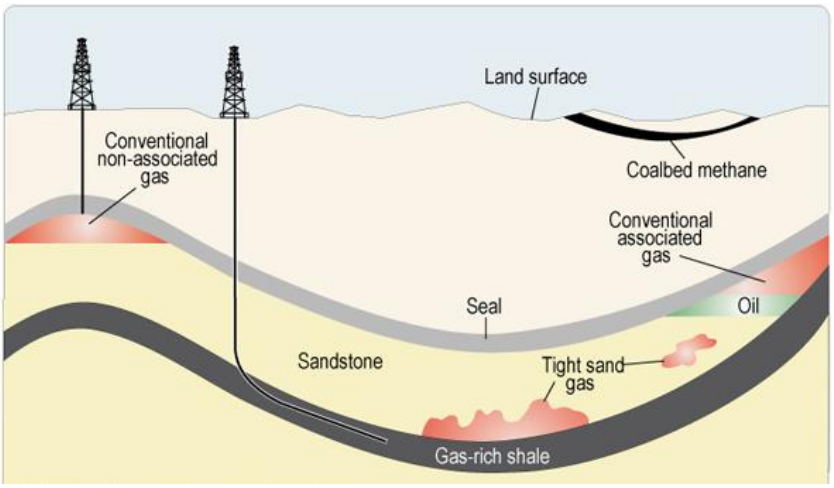

Figure 2.2: Schematic Geology of Natural Gas Resources (US Energy Information Administration (EIA). 2012)

2.2.2 Prospective Shale Resources outside North America

Shale reservoirs are the most abundant hydrocarbon resources in the world. US Energy Information Administration (EIA) (2013) published a report of the most prospective shale formations in 41 countries with sufficient amount of geologic data for resources assessment. Figure 2.3 shows the results of this report in terms of basin locations and regions assessed. Only the red colour areas in Figure 2.3 represent the basins with necessary data to evaluate technically recoverable resources.

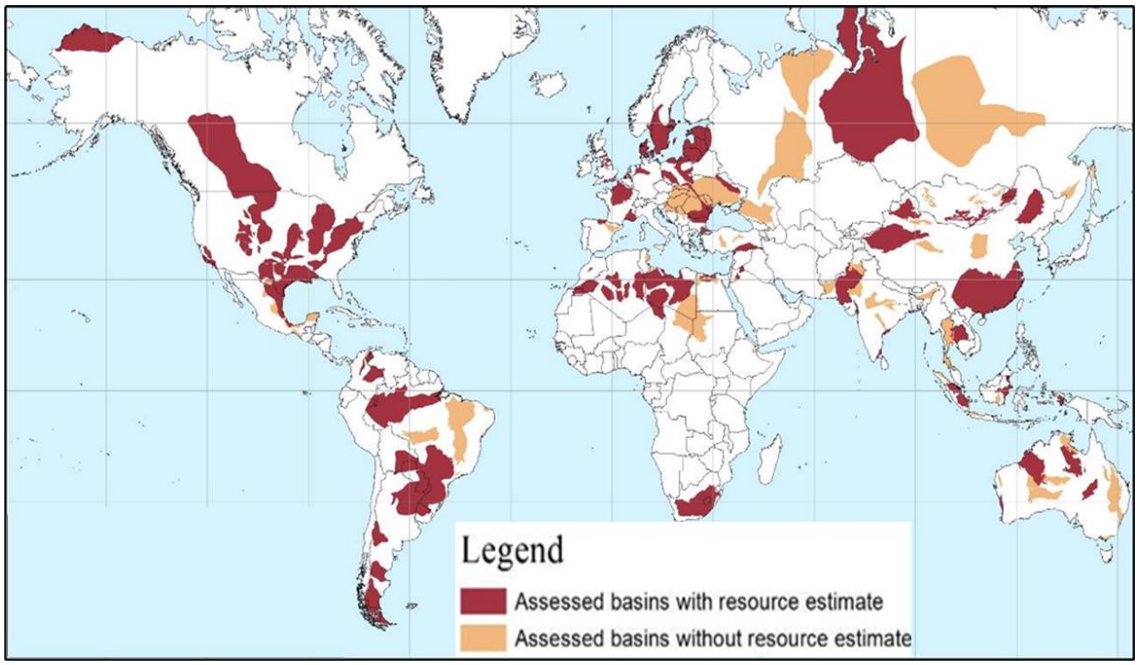

Figure 2.3: Map of assessed shale oil and gas formations (EIA 2013)

Table 2.1 lists the 10 countries with the largest technically recoverable resources of shale gas based on the EIA assessment of shale resources in 41 countries. Technically recoverable resources are defined as the volumes that can be produced irrespective of oil and natural gas prices and development costs. Table 2.1 and 2.2 shows that the top 5 countries: China, Argentina, Algeria, USA and Canada hold more than 50% of the world total technically recoverable shale gas resources. It is expected that the American shale experience will be replicated in other parts of the world in the near future allowing some countries to emerge as major producers. China and Argentina are leading the shale development outside North America with commercial production already underway. Other countries like Saudi Arabia, Australia, Algeria and Russia are still at exploration stage and yet to obtain commercial development.

Table 2.1: Top 10 countries with technically recoverable shale gas resources (EIA 2014)

Rank	Country	Shale gas (trillion cubic feet)
1	China	1,115
2	Argentina	802
3	Algeria	707
4	U.S.	665
5	Canada	573
6	Mexico	545
7	Australia	437
8	South Africa	390
9	Russia	285
10	Brazil	245
	World Total	**7,299**

2.2.3 Development of Shale Plays in North America

The shale oil and gas revolution started almost ten years ago in the United States and Canada due to the continuous improvement of horizontal drilling and multistage hydraulic fracturing technologies. The existing and well developed midstream and downstream facilities in oil and gas industry in North America were also a key factor in the shale industry success. Currently, only USA and Canada have significant commercial production from shale reservoirs. The major producing shale plays in North America are Marcellus, Bakken, Barnett, Eagle Ford and Haynesville (Hughes 2014, Wang et al. 2014). Figure 2.4 shows current shale plays, some prospective plays and basins. Shale plays rarely cover all basin area due to the high reservoir heterogeneity that affects the well productivity from one region to another.

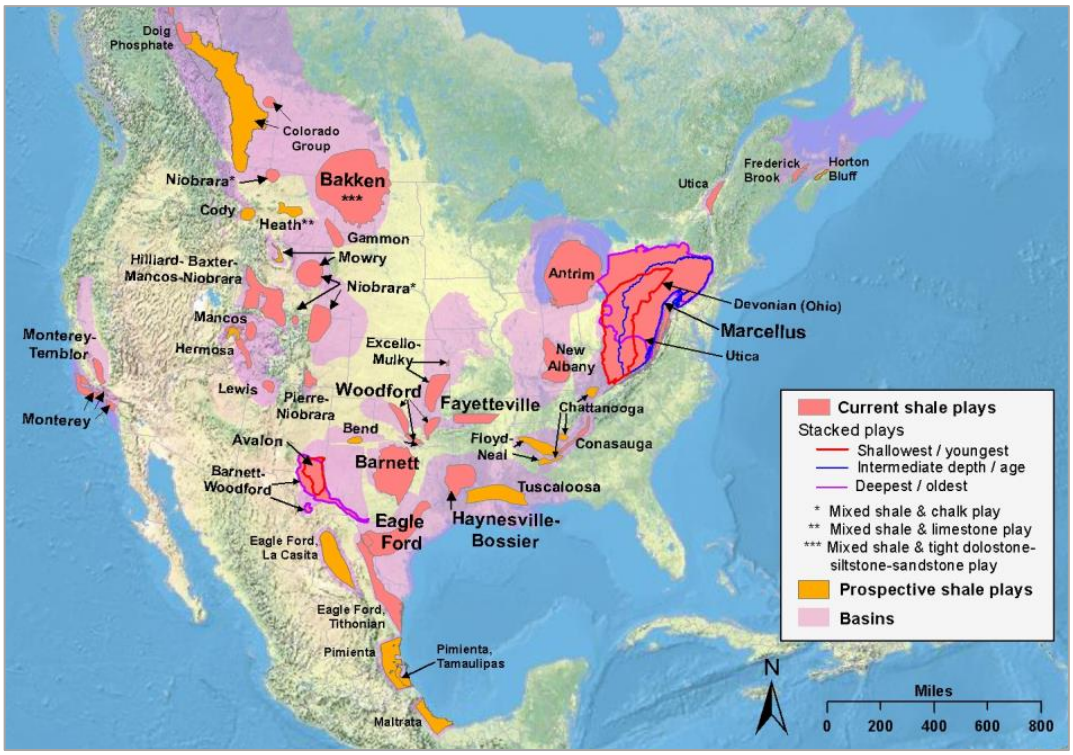

Figure 2.4: Shale gas and oil plays in North America showing current shale plays, perspective plays and basins (EIA 2011).

U.S. Energy Information Administration (IEIA) (2016) estimated the US shale gas proven reserves by the end of 2013 was 159 Tcf amounting to 45% of total proved reserves. In 2013 shale gas wells became the largest sources of total gas production in the United States representing 40% with a production increase from 4 Bcf/d in 2007 to 43 Bcf/d in 2016 (see Figure 2.5).

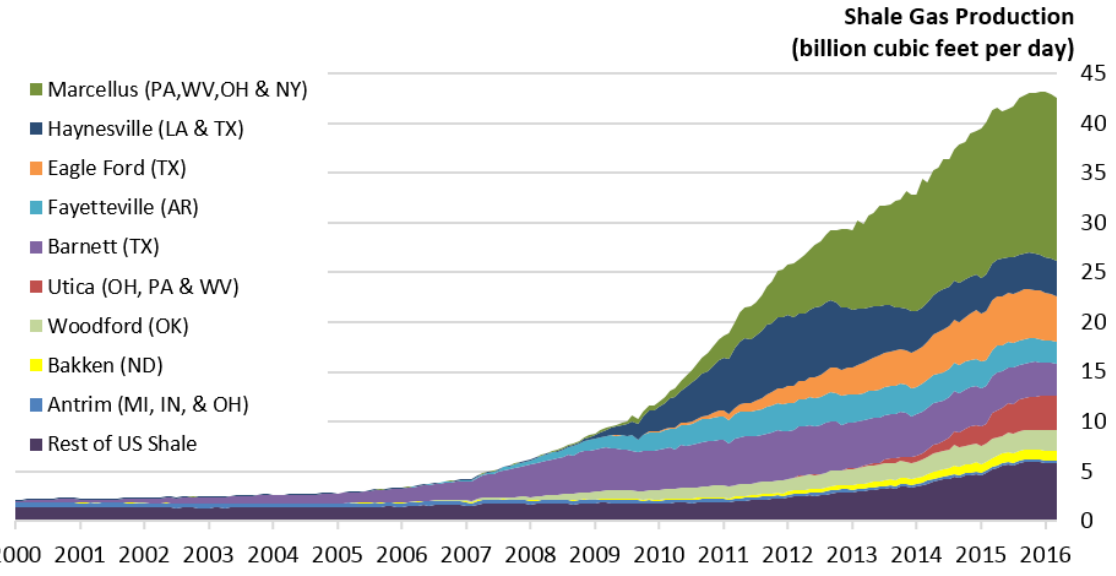

Figure 2.5: US shale gas production (EIA 2016)

2.2.4 Gas Condensate Shale Plays

Although several shale plays are producing in USA and Canada, Eagle Ford is the most important play that is producing significant condensate volumes (EIA 2011). The Eagle Ford Shale is the primary source rock for Austin Chalk hydrocarbon reservoirs (Pearson 2012). Shale formations depth ranges from 4,000 ft to 14,500 ft TVD (True Vertical Depth) with reservoir thickness from 40 to 400 ft (Halliburton 2016a). Figure 2.6 shows the Eagle Ford map with the three distinctive areas oil, wet/condensate and dry gas. According to the Texas Railroad Commission, the condensate production of Eagle Ford in 2014 consists of 20% of the field liquids production.

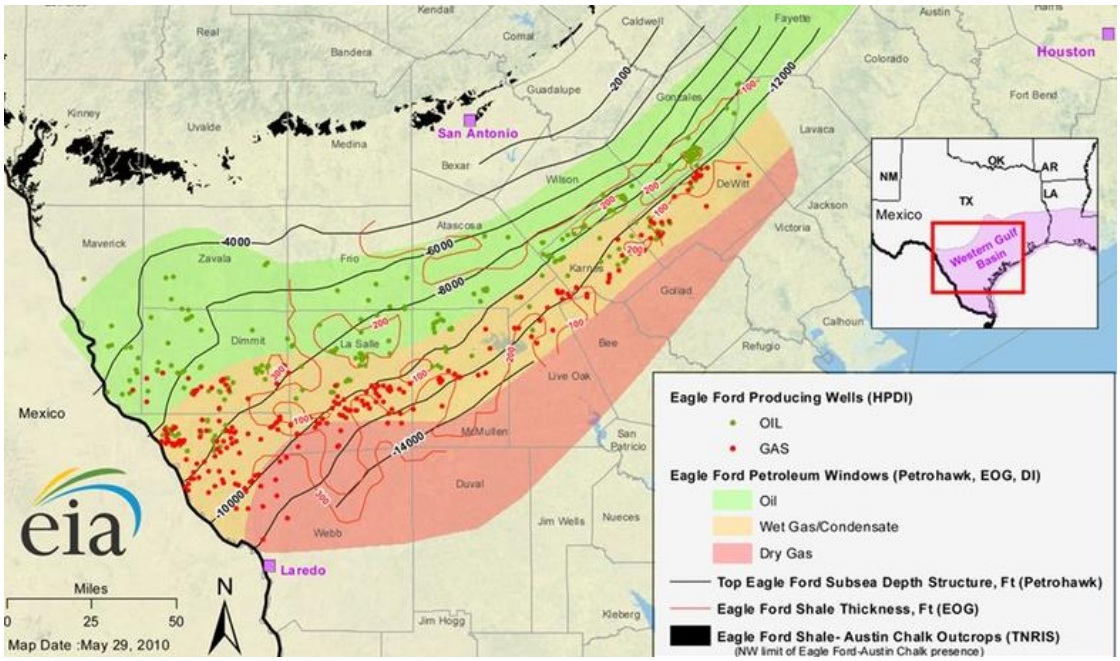

Figure 2.6: Eagle Ford map showing three distinctive areas: oil, condensate and dry gas (EIA 2010)

2.3 Shale Reservoir Characteristics

A comprehensive reservoir characterisation of shale resources is essential for a better understanding of fluid storage, fluid flow and phase behaviour for gas-condensate systems. Contrary to other reservoir types, shale reservoir are self-sourced reservoirs. Besides, porosity and permeability, the key parameters that characterise shale reservoirs are: Kerogen, TOC, (Total Organic Content) and thermal maturity. Moreover, gas is stored as free gas, adsorbed gas and dissolved gas in organic matter. These parameters are explored further in the following Sections.

2.3.1 Kerogen

The ability of source rocks to generate and store hydrocarbons is determined by its kerogen content. Kerogen is a solid mixture of heavy organic compounds; when subjected to heat some types of kerogen generates oil and/or gas. There are four types of kerogen classified according to carbon hydrogen ratio and carbon/oxygen ratio (see Figure 2.7). Three of them can generate hydrocarbon: type I generates oil, type II generates wet gas and type III generates dry gas. Understanding the kerogen type helps to determine the type of hydrocarbon (oil, wet gas or dry gas) (Glorioso and Rattia 2012).

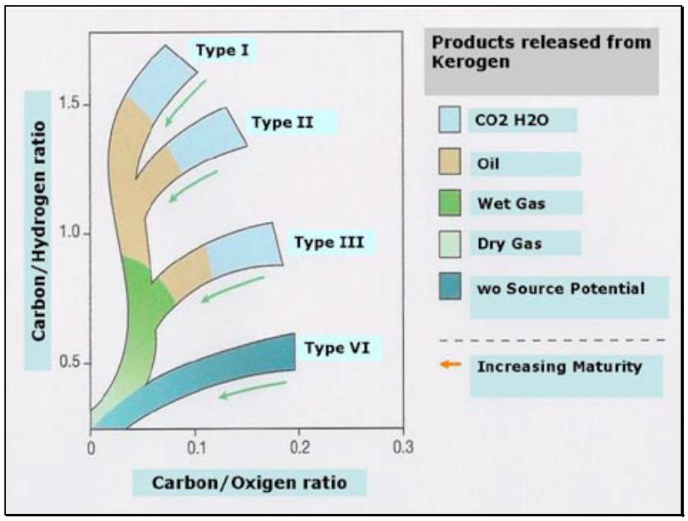

Figure 2.7: Carbon hydrogen ratio and carbon/oxygen ratio classification of kerogen types (Glorioso and Rattia 2012)

2.3.2 Total Organic Content (TOC)

Total Organic Content (TOC) is the amount of material available to be converted to hydrocarbon depending on kerogen type; it is expressed as a percentage of weight or volume of the rock. For conventional reservoirs, TOC is considered as a qualitative measurement of a source rock potential. However, for shale reservoirs, TOC is a key parameter for formation evaluation because it holds a significant part of the reservoir porosity (see Section 2.3.4). A number of synthetic logs and real-time measurement while drilling methods have been developed recently to improve shale reservoir characterization (Zhao, et al. 2015, Rodriguez, et al. 2015, Joshi, et al. 2015). For oil and gas source rocks, the porosity ranges between 1% (poor content) to 10% (excellent content). Table 2.2 gives the average value of TOC for some active shale plays.

Table 2.2: TOC of currently active shale gas reservoirs (modified from Glorioso 2012).

Play	Marcellus	Barnett	Haynesville	Fayetteville
Average TOC	6%	5%	4%	4%

2.3.3 Thermal Maturity

Thermal maturity is a critical element for shale reservoir to determine reservoir quality and type of hydrocarbon. Thermal maturity is defined by the degree to which a source rock has been exposed to high heat needed to break down the organic matter and generate hydrocarbons (Tiab and Donaldson 2015). The heat is a function of the formation depth in the earth's crust. Figure 2.8 shows the generation windows of hydrocarbons. Thermal maturity is a key parameter that can facilitate the understanding of the potential of shale formation. A higher thermal maturity can indicate an improved permeability through nanopores in organic matter (Kuuskraa et al. 2011). The thermal maturity is determined by vitrinite reflectance (R_o) which is measured through microscopic reflectivity of rock sample. R_o values range from 0% to 3%: values below 0.6% indicate immature kerogen without hydrocarbon generation. R_o range between 0.6% and 0.8% indicates oil and range between 0.85 and 1.1% indicates wet gas. Values above 1.5% are sign of potential generation of dry gas (Alexande et al. 2011)

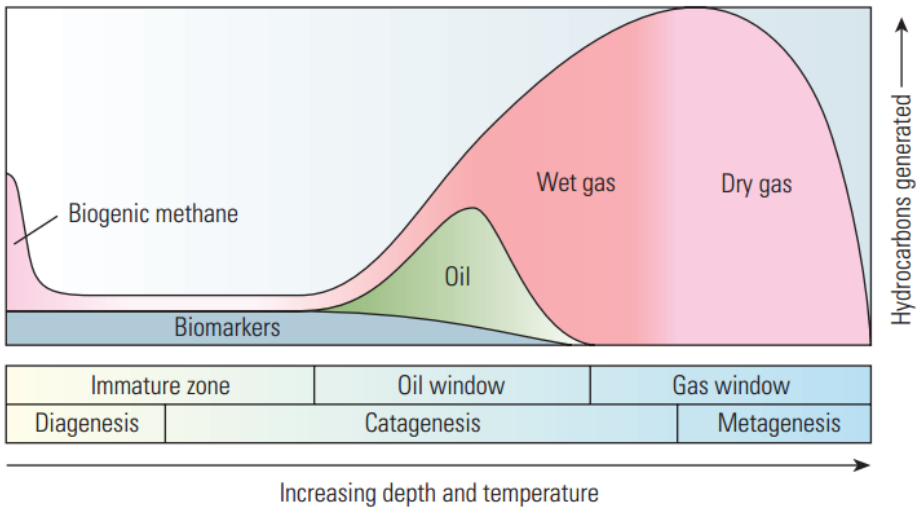

Figure 2.8: Thermal maturity and hydrocarbon generation (Alexander et al. 2011)

Contrary to conventional reservoirs, in the same shale reservoir dry gas can be found in deep area while oil is located in shallower levels and wet gas in-between accordingly with hydrocarbon generation windows depending on conditions of pressure and temperature.

2.3.4 Porosity

Three types of porosity can be found in shale reservoirs: a) clay porosity, b) porosity in no-clay matrix and c) kerogen porosity.

Clay porosity consists of crack-like pores (linear features) with preferred alignment. In no-clay matrix, pores appear around grain particles in triangle and crack shapes. Figure 2.9 gives an example of the three types of porosity determined by Curtis, Ambrose and Sondergeld (2010) through BSE (Backscattered Electron) imaging of shale samples from Haynesville and Barnett plays. Pores in kerogen are round in shape; they are of few nanometres to tens of nanometres in diameter and some up to hundreds of nanometres. Curtis, Ambrose and Sondergeld (2010) reported up to 50% of porosity in Barnett kerogen samples is present within kerogen which makes TOC quantification essential for shale potential evaluation.

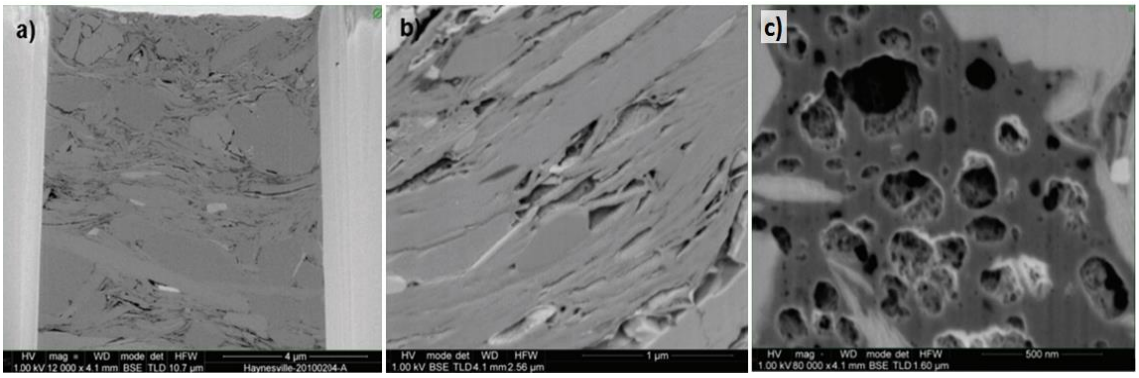

Figure 2.9: BSE (Backscattered Electron) images of porosity types in shale reservoirs. a) shows intergranular porosity in Haynesville sample. b) shows clay porosity in Haynesville sample c) shows kerogen porosity with varying diameter with smaller pores in inner walls. (modified after Curtis, Ambrose and Sondergeld (2010))

The most common technique for shale total porosity measurement is the Gas Research Institute (GRI) method (also known as Crushed Shale Analysis) where crushed small samples, instead of conventional cores, are used in order to accelerate helium expansion to pore space (Kuila 2013). Currently, intensive research activities are ongoing in order to establish adequate techniques to measure porosity, grain density and water saturation in the laboratory. The main issues related to shale reservoirs are (Glorioso and Rattia 2012):

- Removal of water and hydrocarbons from the pore space,
- Problem of full access of gases and liquids (helium, nitrogen, methane, mercury and water) to the pore system due to the low permeability,
- Adsorption effect,

- Presence of natural fracture.

These challenges affect similarly the ability to carry out laboratory experiment of multiphase core flooding on shale samples (e.g. gas-condensate, oil-gas and oil-water) where the control and the measurement of phase saturation is problematic.

2.3.5 Gas Storage

In Shale reservoir, gas is stored in three ways as (see Figure 2.10):

- **Free gas**: stored in kerogen pores and non-organic pores and natural fracture;
- **Adsorbed gas**: resides in layers of gas molecules adhered to kerogen and mineral surfaces under the effect of surface energy. The very small pore size in shales furnishes large inner pore surface area, thus they have a higher adsorption capacity than conventional reservoirs.
- **Dissolved gas**: in organic matter (bitumen). Dissolved gas molecules are taken by the organic matter volume rather than the surface of organic and non-organic matter as adsorbed gas molecules.

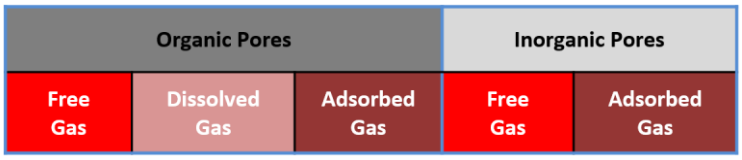

Figure 2.10: Gas storage in shale reservoirs.

The adsorbed gas in shale reservoir can be described by Langmuir Isotherm in equation 2.1 (Langmuir 1918)

$$C_g = \frac{V_L\, P}{P_L + P} \tag{2.1}$$

where C_g is the gas content measured (scf/ton), and V_L is Langmuir volume defined as the maximum volume of gas that can be adsorbed on the shale surface at infinite reservoir pressure (scf/ton), P_L is Langmuir pressure (psi) corresponding to pressure at half Langmuir volume, V_L and P is reservoir pressure (psi). Longmuir Isotherms are routinely generated using core analysis.

Figure 2.11 depicts an example of gas content (free, adsorbed and total) of Barnett shale vs. pressure resulted from core sample measurements (Lewis, et al. 2004). This Figure shows that adsorbed gas can contribute to the production only at low reservoir pressure (under 1000 psi).

Using 3D Barnett shale reservoir model, Cipolla et al. (2010) concluded that desorbed gas represents only 5-15% of the ultimate gas production mainly during later life of the well when the average reservoir pressure is low enough to allow gas desorption. Thus adsorbed gas has insignificant impact on development economics of shale reservoirs.

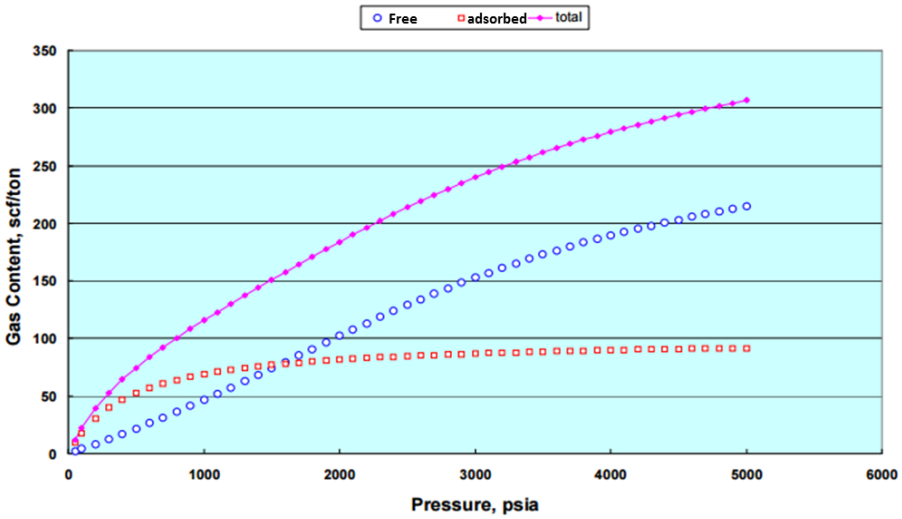

Figure 2.11: Example of Barnett gas content. The red dots indicate adsorbed gas content, the blue is free gas, and the pink line is the total gas content (Lewis, et al. 2004).

2.3.6 Water Saturation

Water can be present in shale matrix only in inorganic matter as capillary bound water and clay bound water (Glorioso and Rattia 2012). Shale reservoirs are characterised by low initial water saturation known as *subirreducible initial water saturation* (Wang and Reed 2009). At this saturation connate water is immobile due to high capillary pressure forces. The produced water during first year of well life is as a result of extended flowback of injected fracturing water (Zolfaghari, et al. 2015) (see Section 2.4).

2.3.7 Permeability

Due to the small pore size in shale reservoirs, matrix permeability is very low. It ranges from 40 to 1000 nano-Darcy. A hydraulic fracturing operation is required to make this type of resources commercially valuable. Javadpour (2009), presented a summary of measured permeability data for 152 samples from nine shale reservoirs in Figure 2.12. From this Figure, we observe that 90% of the measured permeability is less than 150 nD.

To measure permeability of shale gas reservoirs, steady-state methods are not practical because of the long times needed to establish a steady-state flow due to the nano-Darcy permeability ranges. The pulse decay technique is usually used to determine permeability

in shales(Cui, Bustin and Bustin 2009). In this technique, a slight differential pressure is applied on the upstream and the downstream on the core sample and the pressure variation with time on both ends and through the sample is observed. The rock permeability is estimated using analytical or numerical methods.

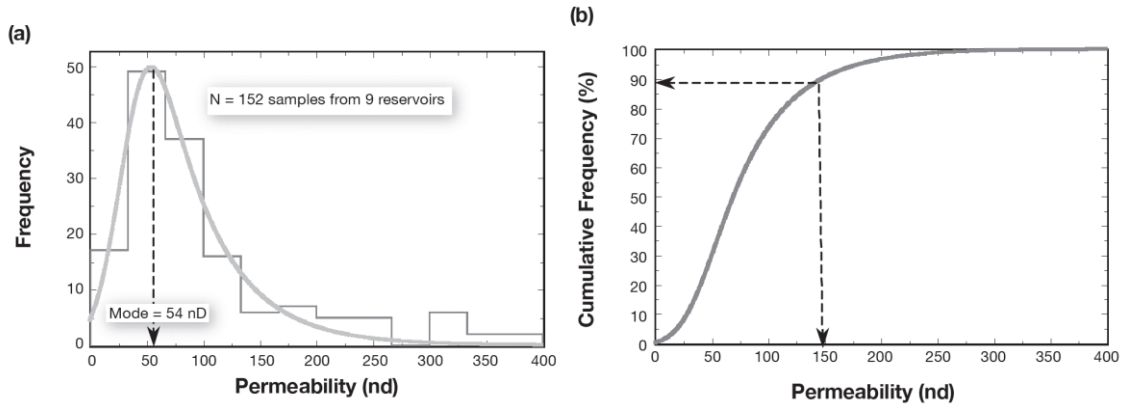

Figure 2.12: Frequency versus permeability of 152 shale gas samples from nine reservoirs. (a) Permeability distribution, (b) cumulative frequency distribution (Javadpour 2009).

Crushed Shale Analysis (sometimes referred to as GRI-method) is another technique developed by the Gas Research Institute (GRI) to measure shale permeability of crushed samples (0.5-0.85mm) by using gas expansion (Luffel, Hopkins and Schettler Jr 1993). This technique provides the advantage of eliminating the risk of overestimation the matrix permeability in the pulse decay technique caused by the existence of micro-fractures in core samples. However, it is usually conducted at very low pressure which does not reflect the overburden pressure effect on shale permeability.

2.4 Current Drilling and Completion Practices in Shale Gas Reservoirs

As a result of the recent technical advance in horizontal drilling and hydraulic fracturing, shale reservoirs can be economically developed. The horizontal length of the well is drilled into the shale formation and it is cemented and cased. The multistage fracturing starts from the well toe to the heel. Every stage segment is isolated with a plug from the previous fractured stage and perforations are created at the centre of the stages at 100-300 ft apart (see Figure 2.13). Then, the hydraulic fractures are initiated from the perforation by pumping fracturing fluid and proppant at high pressure through the wellhead using high horse power pumps. At the end of the fracturing process, the plugs are drilled or milled out. This technique is the most common completion process used in shale wells and it is usually referred to as Plug and Perf. completion.

Another completion technique called Sliding Sleeves has been used recently instead of Plug and Perf. This technique consists of placing a permanent system combined with movable sleeves at each stage. The main advantage of Sliding Sleeves is the reduction of the completion time where all stages are fractured in one session without carrying on the "plug, perf, repeat" process (Shaw 2011).

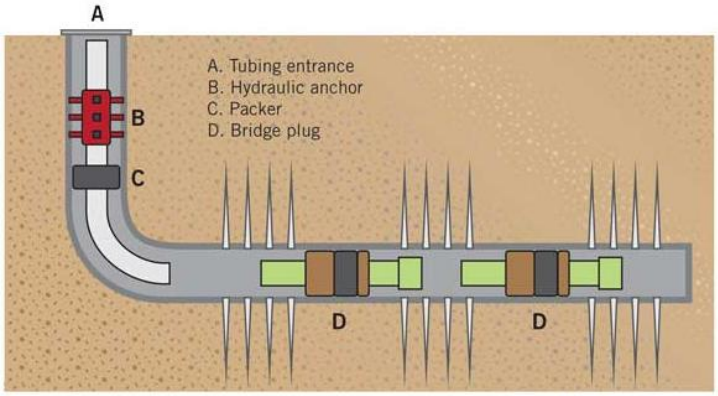

Figure 2.13: Schematic of Plug and Perf. completion(Zhao, Yang and Li 2013).

About 2-10 million gallons (1,000-4,000 m3) of water and 2.5-5.5 MMlbs of proppant is used during hydraulic fracturing of one horizontal well. The role of the proppant is to keep the fracture open when the pumping is stopped. In addition, a number of chemical additives with low concentration of 1-2% are mixed with the fracturing fluid to minimise friction, to carry the proppant, to reduce corrosion and to prevent micro-organism growth (Gallegos and Varela 2015, Patel, et al. 2014). Figure 2.14 gives an example of volumetric composition of a fracture fluid used by Haliburton in South Texas wells.

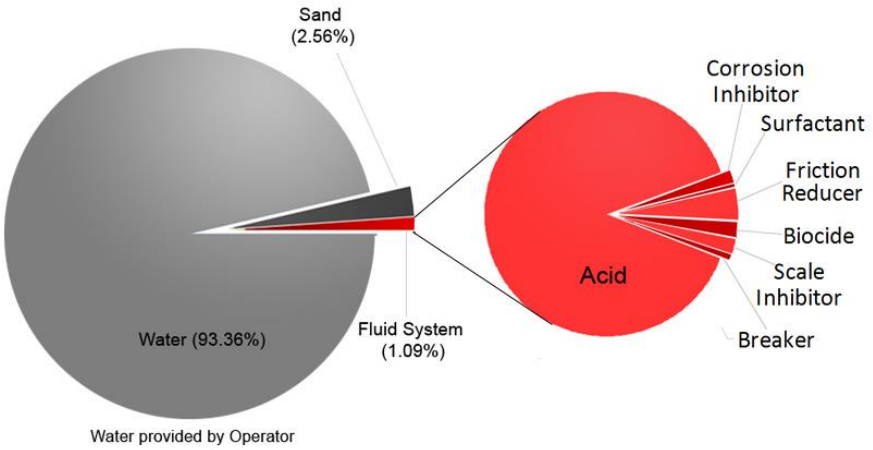

Figure 2.14: Example of volumetric composition of a fracture fluid used by Haliburton in South Texas wells (Halliburton 2016b)

In order to increase the contact between the wellbore and the reservoir, multi-stage fracturing aims to maximise the Stimulated Reservoir Volume (SRV) by creating successive fractured zone along the well path (Figure 2.15). This well stimulation technique is known as multi-stage fractured horizontal wells (MFHW).

A shale well can extend horizontally up to 6500 ft with 10 to 40 fracture stages with fracture spacing of 150-500 ft and half-length of 300-600 ft. Well spacing varies from 60 to 85 acre. Practically, the well lateral length is determined by the economics of drilling and completion operations and wellbore stability.

Shale wells are usually drilled perpendicular to the maximum principal stress to maximise the fracture propagation in the reservoir. Initiated fractures tend to open against the minimum principal stress. The fracture propagation in vertical direction is carefully monitored so that it does not reach other formations below or above the shale formation. If this happens, it can cause a decrease in the well productivity or lead to fresh water contamination by fracturing fluids. Microseismic surveys are used routinely to monitor the fractures propagation in 3D and to establish an estimated SRV (Stimulated Reservoir Volume).

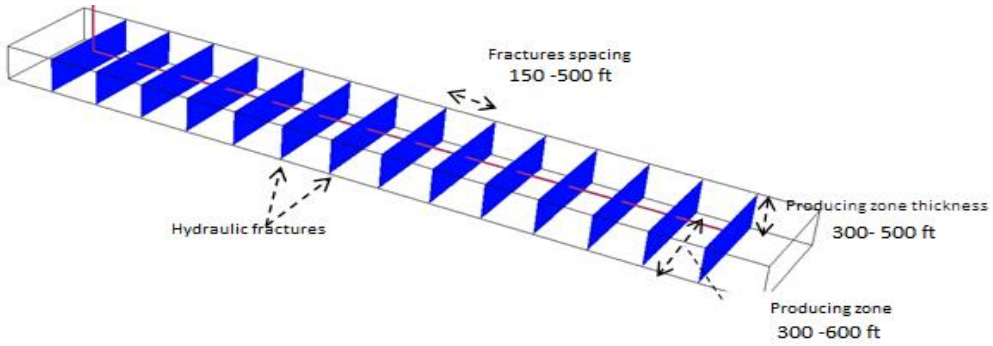

Figure 2.15: Schematic illustration of multi-stage fractured horizontal well

In shale reservoir development, several wells (usually 6 wells) are drilled from a single pad to reach large reservoir area with minimum surface use. Figure 2.16 illustrates a schematic of the top view of shale wells in Eagle Ford in Webb County, Texas and it shows that 3 to 6 wells are drilled from a single pad.. This practice reduces significantly the footprint of shale fields where extensive drilling is needed to develop shale plays economically. In addition, well pads contributed to the shale revolution by cutting the drilling cost (by reducing the rig move time from a well to another in the same pad) and facilities cost.

In the past few years, the activity of the extensive hydraulic fracturing in shale plays caused a public debate about the environmental risks that can be caused by this technique. The most important debated risk was the underground water contamination by the fracturing fluids (Arthur, Bohm and Layne 2009, Vengosh et al. 2014). Hydraulic fracturing has been used in the industry for more than six decades and it is a well-controlled process (King 2014). The contamination of ground water by fracturing fluid through induced fracture is negligible as the fractures extend less than 600 m above the well perforation(Torres, Yadav and Khan 2016, Flewelling, Tymchak and Warpinski 2013).

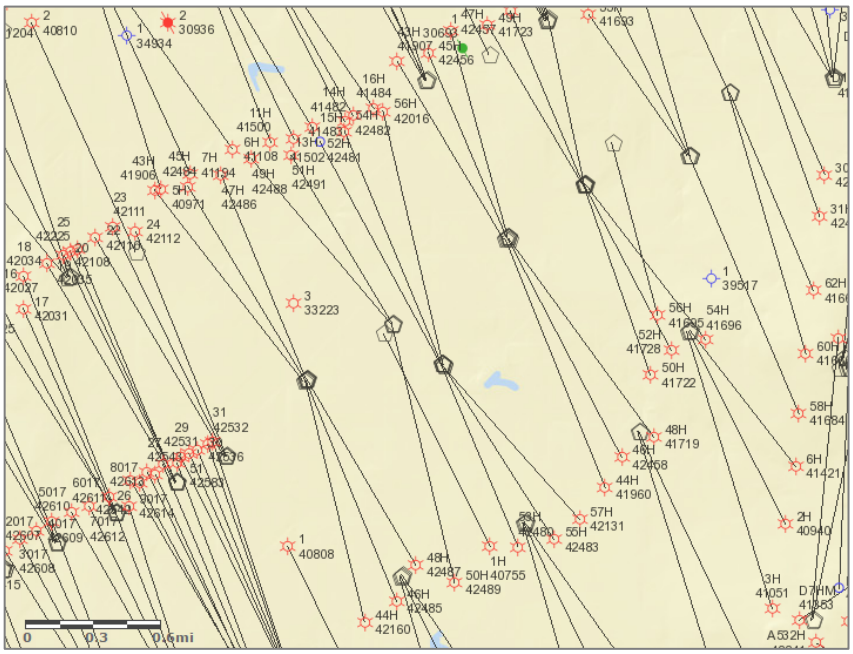

Figure 2.16: Map of horizontal well drilling from single pad in Eagle Ford in Webb County, Texas (Texas RRC).

Different types of fracturing fluids are used in shale reservoirs: water based fluids, oil based fluids, energised fluids, multi-phase emulsions and acid fluids.

In shale gas reservoirs, when water is pumped to initiate hydraulic fractures, it penetrates outer layers of shale matrix by imbibition under high capillary pressure between gas and water and remains trapped as the initial water saturation is *subirreducible*. Usually, only a small fraction of injected water is recovered during production. For instance, Vidic et al. (2013) reported that only 10% in average of injected water is recovered from Marcellus wells. This phenomenon is referred to as *capillary wicking* or *phase trapping* (Mahadevan, Sharma and Yortsos 2007, Bertoncello, et al. 2014). In order to alleviate the effect of water

blocking, the industry is using more and more "*water-free*", particularly CO_2 or N_2 energized fracturing fluids (Rassenfoss 2013, Asadi, et al. 2015).

2.5 Challenges in Development of Shale Gas-Condensate Reservoirs

2.5.1 Condensate Banking Effect

Condensate banking has been long considered a major challenge in gas-condensate reservoir development projects. Gas-condensate fluids are characterised by retrograde condensation phenomenon where at high initial reservoir pressure the fluids is in gas phase but when the pressure drops below the dew point, liquid condensate starts to form in the reservoir and continues to accumulate with decreasing pressure. Figure 2.17 illustrates results of a CCE (Constant Composition Experiment) of a gas-condensate sample from Pearsall Shale formation in La Salle County, Texas. The condensate begins to accumulate at a dew point of 5123 psig and reaches a maximum dropout of 5.2 % of pore volume.

The increasing condensate saturation in the reservoir reduces the gas relative permeability thus reducing the well productivity. The condensate banking effect on well productivity is controlled by three factors:

- Phase behaviour: the condensate buildup and compositional change as function of pressure;
- Flow behaviour: the effect of condensate saturation on gas permeability;
- Well completion: the contact between the wellbore and the reservoir (e.g. vertical/horizontal, fractured/not fractured completion)

In conventional reservoirs, the production loss due to the condensate banking can be significant (Hinchman and Barree 1985, Barnum, et al. 1995, El-Banbi and Wattenbarger 1998, Du, Guan and Bai 2004) but pressure maintenance technique or producing at bottomhole pressure above the dew point can alleviate its effect.

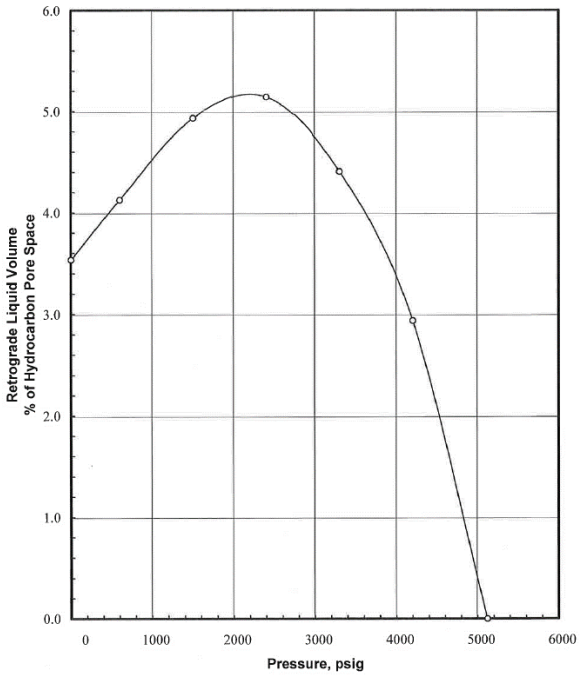

Figure 2.17: Condensate liquid volume vs. pressure (source: RRC Texas)

For shale reservoirs, the situation is more complex. As a result of the extremely low reservoir permeability, wells start to produce at a bottomhole pressure under dew point after few days or months of production. Besides, the pressure maintenance techniques have not yet been developed for shale reservoirs (see Section 2.5.3). Hence, shale gas-condensate wells remain under the effect of condensate banking for almost all their entire production period.

Consequently, an accurate quantification of how the condensate forms in the reservoir and how it affects the gas permeability is crucial to predict the production of planned wells in field development projects and to analyse the performance of existing wells for reservoir management purposes.

2.5.2 Reservoir Drive Mechanisms and Recovery Factors

Due to the very low permeability of shale reservoirs, only the Stimulated Reservoir Volume (SRV) are connected to the wellbore through natural and induced fractures. Thus, the gas expansion is the major drive mechanism during the first stage of production. Gas desorption from organic matter and non-organic surface can contribute to production only at late production stages.

Figure 2.18 shows the average well gas production rate vs. time for major US shale plays.

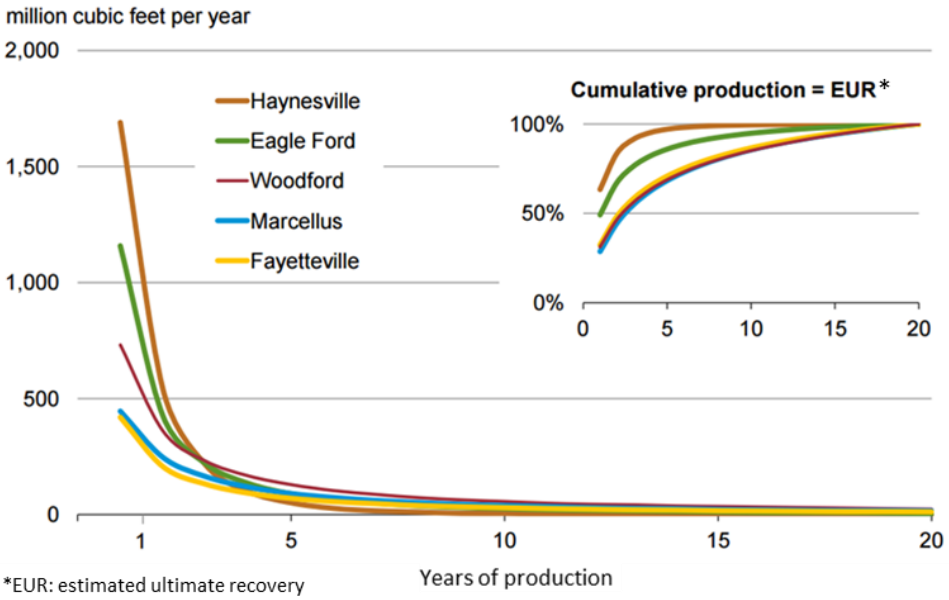

Figure 2.18: Average production profiles for shale gas wells in major U.S. shale (Adam 2013)

Production from shale gas wells can be divided into three stages: 1) first short period with high initial production rate from hydraulic and natural fractures due to low storage capacity and high conductivity, 2) Production from matrix where flowrate is much lower than first period but with lower decline rate, 3) Late production stage where gas desorption starts to contribute as the average reservoir pressure is low enough to allow desorption of considerable gas volumes. The current shale development techniques have an estimated recovery factor of 28-40% while conventional reservoirs recovery factor ranges between 60 to 80%.

2.5.3 Enhanced Recovery

Secondary recovery techniques such as water and gas injection are difficult to deploy because of the 4 to 5 orders of magnitude of permeability difference between fractures and matrix. Recently, utilisation of CO_2 Huff-n-Puff for shale gas-condensate wells has gained interest from researchers and operators (Sheng 2015, Eshkalak, et al. 2014). In absence of proven enhanced recovery techniques for gas and gas-condensate reservoirs, the only available means to maximise recovery is by optimising the well design in terms of hydraulic fracture spacing, well spacing and lateral length (This is discussed in detail in Chapter 6).

2.6 Shale Reservoirs vs. Conventional Reservoirs

What makes shale reservoirs so different from other reservoir types is the extremely low permeability as a result of the very small pore size. Figure 2.19 provides a good comparison

of permeability and pore sizes between shales, tight sands, sandstones and limestones (Williams 2012). Shale reservoirs are situated in the extreme bottom of pore size scale which is less than 300 nm while pore size in tight sands range from 300 nm up to 1 µm and in conventional reservoirs from 1 µm to few tens of µm. Consequently, shale permeability is less than few hundreds of nD. Porosity of shale reservoirs is mainly less than 10% which is relatively lower than other reservoir types.

This nanoscale pore size range in shale reservoirs implies a very different gas flow regime that deviates from the laminar Darcy flow to slip flow and Knudsen flow. Moreover, the high capillary forces due to very small pore size dominate the gas-condensate flow. The gas single-phase flow and gas-condensate two-phase flow are investigated in Chapter 3.

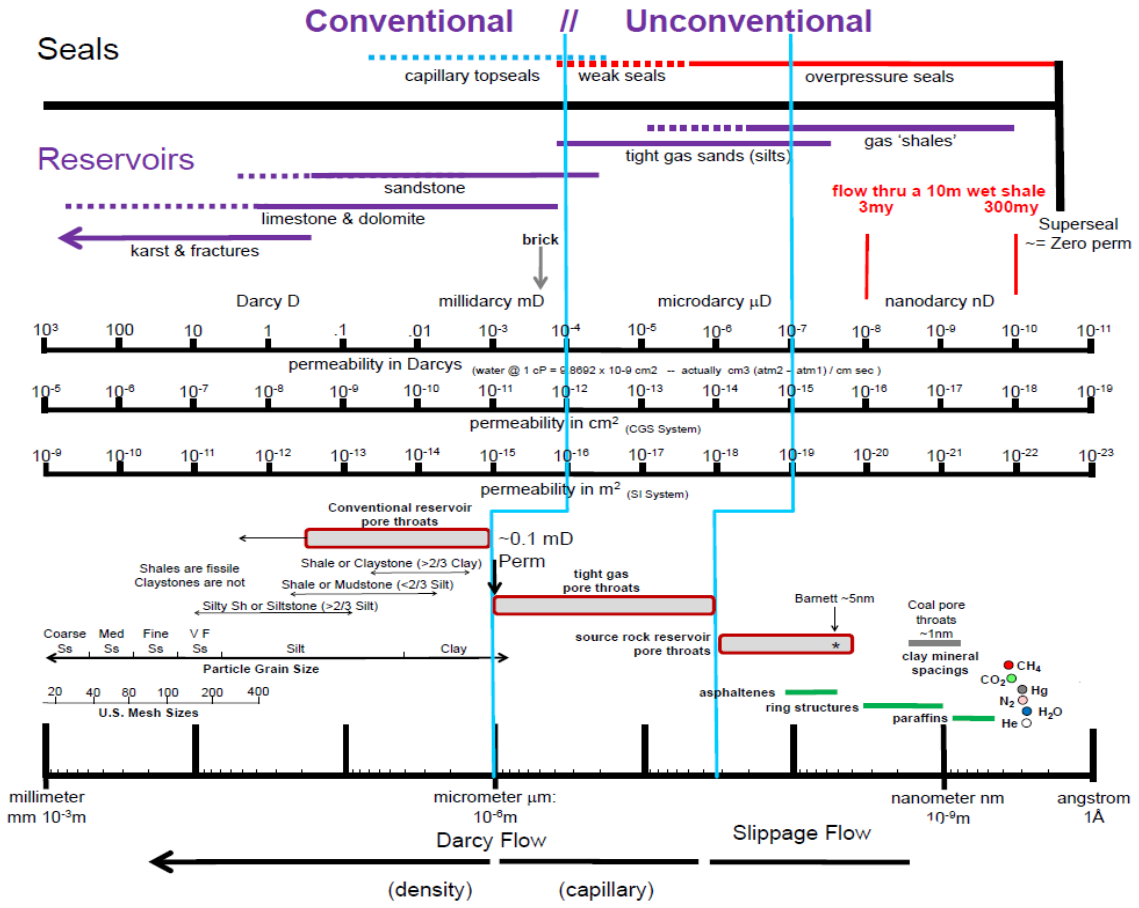

Figure 2.19: Pore size and permeability of shale vs. tight sands and conventional reservoirs (Williams 2012)

The high capillary pressure in shale matrix affects, as well, the phase behaviour of gas-condensate fluids in shale matrix. Condensate tends to start forming at higher dew point pressure and to reach higher saturations than in conventional reservoirs. This phase behaviour deviation is examined in Chapter4 whilst the effect of the deviation of flow

behaviour and phase behaviour of gas-condensate fluids in shale matrix is evaluated in Chapter 5.

Table 2.3 gives a more extensive comparison between shale reservoirs, tight sands and conventional reservoirs.

Table 2.3: Comparison between shale gas, tight gas and conventional reservoirs

	Shale reservoirs	Tight Gas	Conventional reservoirs
Reservoir Extent	Continuous	Lenticular/Blanket/Layer	Lenticular/Blanket/Layer
Source	Self/sourced	No /Migrate in	No /Migrate in
Trap	Auto trap	Buoyancy trap	Buoyancy trap
Depth, ft	2000 -15000	To 20000	Shallow to deep
Thickness, ft	50-600	200-4500	100's-1000's
Pore Size	3×10^{-2} µm ≥ d_{pore}	1µm ≥ d_{pore} ≥ 3×10^{-2} µm	d_{pore} ≥ 1µm
Porosity, %	<10% Barnett 8%	7-15	14 – 25+
Permeability	< 1000 nD	< 0.1 mD	> 0.1 mD
Fluid storage	Pore space Adsorbed to organic matter or clay particles Dissolved in organic matter	Pore space	Pore space
Reservoir mechanism	Diffusion / Solution	Solution	Solution
Wettability	water (no-organic matter) or hydrocarbon (organic matter)	water	water
Water production	No / insignificant	Can produce	Can produce
TOC	Yes	No	No
Wells	Horizontal	Horizontal / Deviated/ Vertical	Horizontal /Deviated/ Vertical
Completion	OH/CH	OH/CH	Primarily CH/OH Carbonates
Fracturing	For commercial / Multi-stage	For commercial	To increase production

2.7 Summary

Shale resources consist of the most abundant hydrocarbon resources in the world. Shale oil and gas development in USA and Canada have demonstrated the importance of this type of hydrocarbon resources and how they have been reshaping the energy landscape.

Shale gas-condensate reservoirs are very different from conventional reservoirs in terms of rock properties, gas storage, gas-condensate two-phase flow and phase behaviour. Due to very low permeability condensate banking effect is severer due to high drawdown from reservoir to wellbore and affects well productivity almost throughout the entire life of the well. Better understanding of how condensate forms in the reservoir and how it affects the well productivity is crucial for well performance estimation and field development studies.

As enhanced recovery technologies for shale gas-condensate reservoir are still to be developed, the only available means to maximise production is well design optimisation by choosing the best hydraulic fracture spacing and well spacing to minimise condensate banking effect.

CHAPTER 3: GAS-CONDENSATE FLOW MODELLING IN SHALE MATRIX

3.1 Introduction

Condensate banking is the most challenging engineering problem in gas-condensate reservoir development where condensate accumulation in the reservoirs reduces dramatically the gas permeability resulting into loss of well productivity. Assessment of condensate banking effect is important to predict well productivity and to diagnose well performance.

Traditionally, Darcy law combined with relative permeability models have been used for flow behaviour modelling in conventional reservoirs and it is widely adopted in reservoir engineering commercial tools. For shale gas-condensate reservoirs, the gas flow deviates from Darcy flow to micro-flow known as Knudsen flow due to the very small pore size in shale matrix (1-300 nm) compared to conventional reservoirs (10 -200 μm). The Knudsen flow is highly dependent on pore size distribution and reservoir pressure (see Section 3.2.1).

When condensate forms in shale matrix it blocks the lowest range of pore size to the gas flow and only the remaining range of free pore sizes is accessible to gas flow. Thus, Knudsen flow is affected by condensate saturation. Disregarding this effect can lead to overestimation of Knudsen flow contribution in well production under condensate banking effect.

Although, the gas single phase flow modelling in shale reservoirs using Knudsen flow has attracted researchers interest in recent years, the effect of liquid saturation (water, oil or condensate) on Knudsen flow has not yet been well addressed.

In this Chapter, the effect of condensate saturation on Knudsen flow is evaluated using a 3D pore network with random pore size distribution. The Knudsen flow is incorporated at the pore level and gas permeability is evaluated for the whole network. In addition, the pore distribution effect in terms of log-normal median and standard deviation is investigated.

3.2 Gas Single-phase Flow in Shale Matrix

Shale reservoirs are dual porosity/dual permeability systems containing two media: matrix and fracture network. The fluid flows from matrix into the fracture and to the wellbore. The

matrix plays two roles; fluid storage and conductivity to the fractures while fractures serve only as connection between matrix and wellbore. Fluid flow in fractures in shale reservoirs is similar to conventional reservoirs where the same technique is used to create propped fractures. The main difference of fluid dynamics between shale reservoirs and conventional reservoirs resides in shale matrix where Darcy law fails to describe the gas flow in pores at nano and micro-scale.

3.2.1 Gas Flow Regimes

The gas flow in nanopores deviates from the standard continuum flow due to the interaction between molecules-molecules and molecules-pore walls (Javadpour 2007). Three non-Darcy flow regimes: slip flow, transition flow and free-molecular flow, are distinguished using Knudsen number which is defined as a measure of the degree of density rarefaction of gas flow in micro and nano-channels. It is mathematically expressed as:

$$Kn = \frac{\lambda}{R} \tag{3.1}$$

Where R is the hydraulic radius (m) and λ is the average minimum free path (m)

$$\lambda = \frac{\mu Z}{P}\sqrt{\frac{\pi R_g T}{2M}} \tag{3.2}$$

Where μ is the viscosity, Z is the compressibility factor, τ is the tortuosity, P is the absolute gas pressure (Pa), T is the absolute temperature (K), M is the average molecular mass (kg/kmol) and Rg = 8314 J/kmol/K is the universal gas constant.

Table 3.1 illustrates the classification of flow conditions according to the Knudsen number limits in pipes as the continuum, slip, transition, and free molecular flow regimes (Roy et al. 2003).

Table 3.1: Classification of flow conditions in pipes according to the Knudsen number limits (Roy et al. 2003)

Knudsen number	$Kn < 0.01$	$0.01 < Kn < 0.1$	$0.1 < Kn < 10$	$Kn > 10$
Flow regime	Continuum	Slip	Transition	Free molecular

a) Continuum Flow (Kn < 0.01)

Continuum flow occurs at *Kn* values under 0.01 where molecule-molecule interaction is the dominant force. Hagen–Poiseuille law describes continuum flow in channels as

$$q = \frac{\pi}{8}\frac{R^4 \Delta P}{\mu\, L} \tag{3.3}$$

Where q is fluid rate (m^3/s), R is the radius of the channel (m), ΔP is pressure difference (Pa), μ is the fluid viscosity (cp) and L is the channel length (m).

b) Slip Flow ($10^{-3} < Kn < 10^{-1}$)

At $10^{-3} < Kn < 10^{-1}$ range the molecule-wall effect is more pronounced but molecule-molecule is still dominant. Slip flow to slip flow regime dominates when gas molecules near to the channel walls don't exhibit a zero velocity (slip). Navier-Stokes equation is still valid to describe this flow regime with a velocity discontinuity at channel walls. Klinkenberg (1941) model is routinely used to correct permeability measurement in gas core flooding at laboratory conditions.

c) Transition Flow ($10^{-1} < Kn < 10$)

Transition flow occurs with increasing Kn numbers ($10^{-1} < Kn < 10$) translated by a transition from slip flow to free molecular flow. At this range of Kn, traditional flow dynamics laws start break down.

d) Free Molecular Flow ($Kn > 10$)

In free molecular flow, molecule-wall interaction is dominant when average minimum free path is higher than channel radius ($\lambda \gg R$). Molecules are more likely to collide with the channel wall than colliding with other molecules. Figure 3.1 summaries the flow regimes according to Knudsen number.

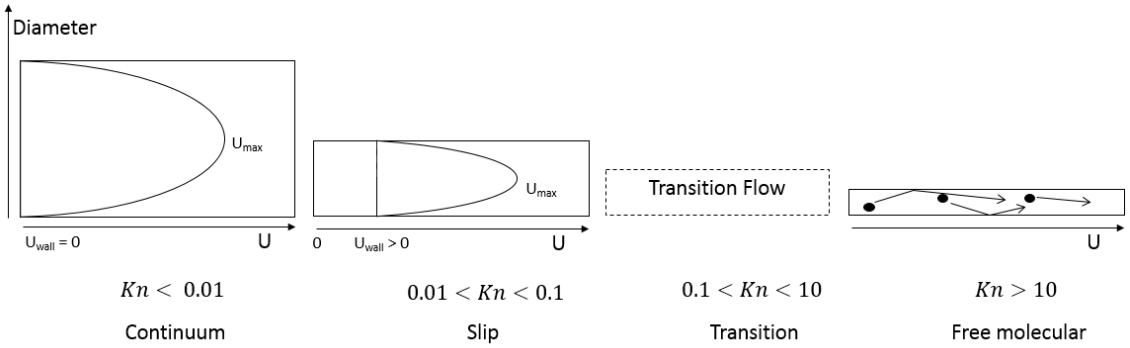

Figure 3.1: Different gas flow regimes as function of Knudsen number (not to scale, adapted from Javadpour (2009))

3.2.2 Microflow Correction Factor

Using Direct-simulation of Monte Carlo (DSMC) and Linearized Boltzmann solution (LBS) results, Beskok and Karniadakis (1999) proposed a general flow model that covers all gas flow regimes in micro channels using a correction factor ξ where

$$\xi = (1 + \alpha K_n)(1 + \frac{4K_n}{1 - bK_n}) \tag{3.4}$$

Therefore, Hagen–Poiseuille equation can be modified to

$$q = \xi \frac{\pi}{8} \frac{R^4 \Delta P}{\mu L} \tag{3.5}$$

Where α is the dimensionless rarefaction coefficient, and b is the empirical slip coefficient independent of the gas properties that can be determined experimentally or using direct-simulation of Monte Carlo (b = -1 for fully-developed slip flow through channels and tube).

The rarefaction coefficient α is a characteristic of gas flow (similar to Knudsen number K_n) where the large values correspond to continuum flow and the large values correspond to free molecular flow.

Beskok and Karniadakis (1999) used Loyalka and Hamoodi (1990) experimental data and proposed the following correlation of the rarefaction coefficient α in function of Knudsen number.

$$\alpha = \frac{128}{15\,\pi^2}\, tan^{-1}(4\, {K_n}^{0.4}) \tag{3.6}$$

Civan (2010) using the same set of data provided another correlation

$$\alpha = \frac{1.358}{1 + \frac{0.170}{Kn^{0.4348}}} \tag{3.7}$$

Figure 3.2 illustrates an example of the correction factor, ξ for methane at a reservoir temperature of 250˚F as a function of pore radius at different pressure values and it indicates that Knudsen flow increases with decreasing pore radius and decreasing pressure and at pressure values more than 2000 psi the correction factor is less significant. The continuous lines represent results using Beskok and Karniadakis correlation for the dimensionless rarefaction coefficient, α in Equation (3.6) and dashed lines are results Civan correlation in Equation (3.7). The two α correlation give very similar values for the correction factor.

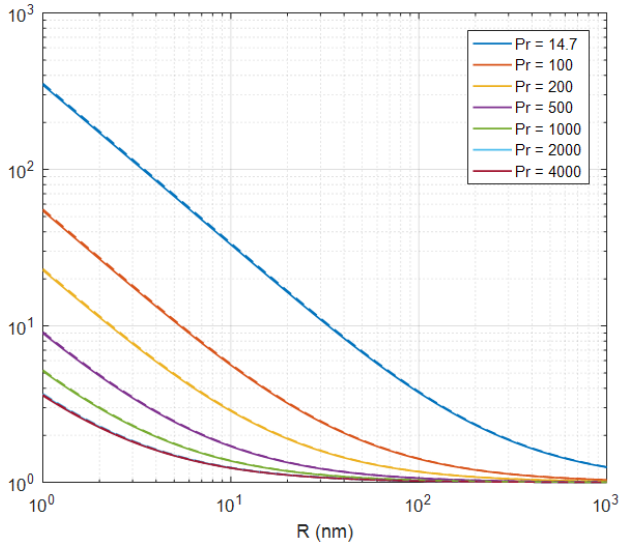

Figure 3.2: Log-log plot of correction factor vs pore radius for different pressure values. The continuous lines represent results using Beskok and Karniadakis correlation for the dimensionless rarefaction coefficient, α and dashed lines are Civan correlation.

3.2.3 Gas Flow Regimes by Reservoir Type

In order to identify the contribution of each flow regime in the gas flow in porous media regarding the three different reservoirs types: conventional reservoirs, tight gas reservoirs and shale gas reservoirs, the gas flow regimes limits were calculated as function of pore size and reservoir pressure for methane at an average gas and gas-condensate reservoirs temperature of 250°F. CH_4 gas represents the dominant component of free gases which allows for the building of a reference case for different gas compositions.

Results of these calculations are presented in Figure 3.3. In shale matrix, the gas flow is dominated by both slip flow regime and transition regime. Within the same shale reservoirs, the two flow regime can occur at different pore sizes.

Slip flow can occur in tight reservoirs with continuum flow at different reservoir pressures and pore sizes. In conventional reservoirs (sandstones and carbonates), gas flow is controlled only by continuum regime (see Figure 3.3). Slip flow can be observed only at very low pressure and temperature ranges usually at lab conditions where permeability correction are carried out using Klinkenberg (1941) model.

In this work, for more clarity, the Knudsen flow refers to multi-scale flow that can occur in shale reservoirs which include slip and transition flows.

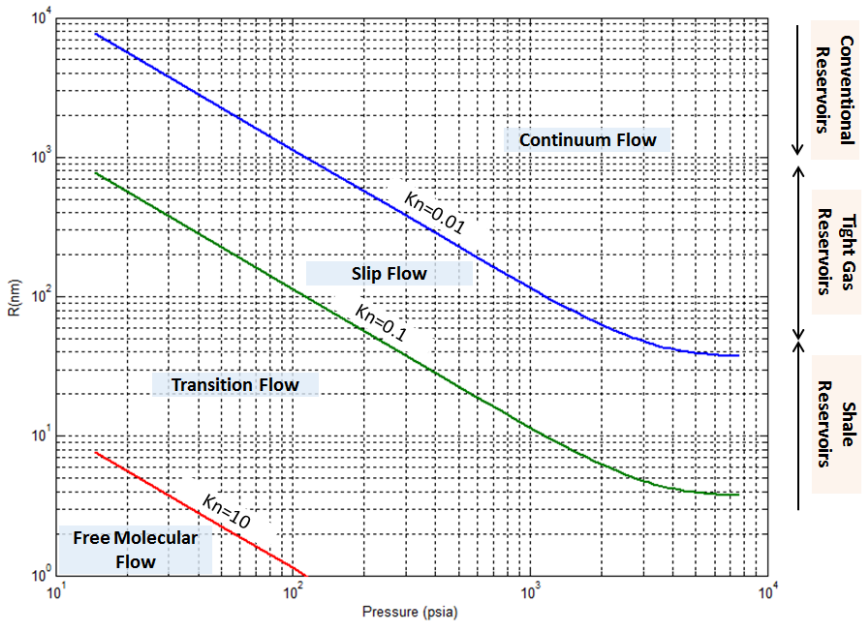

Figure 3.3: The range of gas flow regimes as function of reservoir pressure and pore size for Methane at 393°F. Gas flow in shale reservoirs is controlled mainly by slip flow and transition flow regimes while free molecular flow is unlikely to occur in productive shale reservoirs. Tight gas reservoirs are dominated by both slip flow and continuum flow regimes. In conventional reservoirs, only continuum flow regime can be appearing at reservoir condition.

3.2.4 Gas Flow Modelling in Shale Porous Media

For shale gas reservoir calculation, many authors adopted Beskok and Karniadakis (1999) model in order to correct matrix permeability from Darcy law to more accurate microflow permeability under slip and transition flow regimes as

$$k = \xi\, k_{\infty} \tag{3.8}$$

Where k is the gas apparent permeability, k_{∞} is the intrinsic permeability of shale matrix and ξ is the microflow correction factor defined in equation (3.4). The shale matrix is modelled as a bundle of capillary pressure with the same pore size equivalent to the average pore size R_{avg}.

R_{avg} is inserted in equation (3.1) to calculate ξ as function of pressure. A correlation is used to estimate R_{avg} from intrinsic permeability, k_{∞}, porosity, ϕ and tortuosity, τ as:

$$R_{avg} = A\,\tau^{a}\,\frac{{k_{\infty}}^{b}}{\phi^{c}} \tag{3.9}$$

Where A, a, b and c are constants parameters. For example, Civan et al. (2011) used Carman (1956) correlation

$$R_{avg} = \sqrt{8\tau}\sqrt{\frac{K_\infty}{\phi}} \tag{3.10}$$

And Ziarani and Aguilera (2012) used Windland's correlation (published by Kolodzie (1980))

$$R_{avg} = 5.395\frac{{k_\infty}^{0.588}}{(100\,\phi)^{0.864}} \tag{3.11}$$

Although this method gives a quick and simple model to be applied in shale gas calculation, the representation of shale matrix with a constant pore size can give inaccurate estimation of apparent gas permeability.

Michel et al. (2011) gave a significant contribution by deriving a correction factor for log normal pore size distribution. They proposed an effective average pore size as

$$R_{eff} = v\,e^{3s^2} \tag{3.12}$$

where v is the median and s is the standard deviation log normal distribution. This correlation is applicable only for free gas flow where all pore sizes contribute to the flow and no condensate blockage is considered. A gas-condensate two-phase flow modelling is needed to describe the well performance in shale gas-condensate reservoirs. Hence a model of Knudsen flow under two-phase is provided in Section 3.6.

3.3 Gas-Condensate Two-phase Flow in Shale Matrix

3.3.1 Liquid Flow in Nanotubes

Condensate flow in shale matrix is still a very active subject in nanochannels research. In the research community a liquid flow is always a continuum flow governed by Hagen–Poiseuille equation as the rarefaction effect does not extend to liquids (Mattia and Gogotsi 2008). Many researchers (Günther and Jensen 2006, Gogotsi, Libera and Yoshimura 2000) emphasised the similarity of the slug flow of gas-liquid fluids between microscale and nanoscale. Figure 3.4 represents water vapour-liquid in carbon nanotube showing a similar meniscus gas-liquid interface observed in macrochannels (Gogotsi, Libera and Yoshimura 2000). Experimental studies for hydrocarbon fluids (e.g. gas-condensate fluids) flow in nanotube have not been reported in the literature.

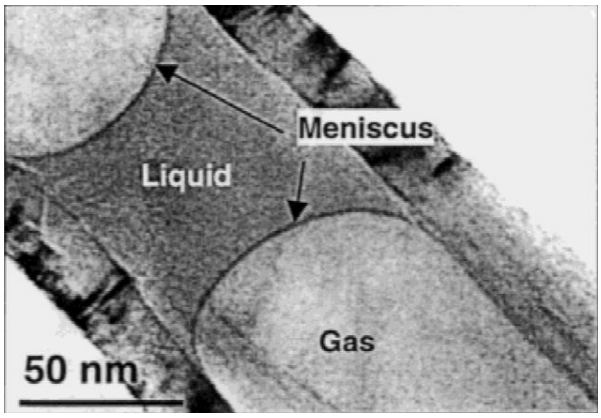

Figure 3.4: TEM (Transmission Electron Microscope) micrographs of water trapped in closed carbon nanotube showing a similar meniscus gas-liquid interface (Gogotsi, Libera and Yoshimura 2000)

3.3.2 Condensate Blockage in Shale Gas Reservoirs

In conventional gas-condensate reservoirs, Fevang and Whitson (1996) divided a drainage area during depletion into three flow regions (see Figure 3.5). A single-phase gas region (Region N°3) far away from the producing well and its average pressure is above the dew-point; condensate buildup region (Region N°2) where condensate starts to drop out but the flowing phase is only single gas due to critical condensate saturation; and near well region (Region N°1) constraining two phase flow (gas + condensate). Due to pressure drop, the liquid phase saturation exceeds the critical saturation and becomes mobile. According to Fevang and Whitson (1996) the well deliverability impairment due to condensate banking is influenced mainly by relative permeability of gas and condensate.

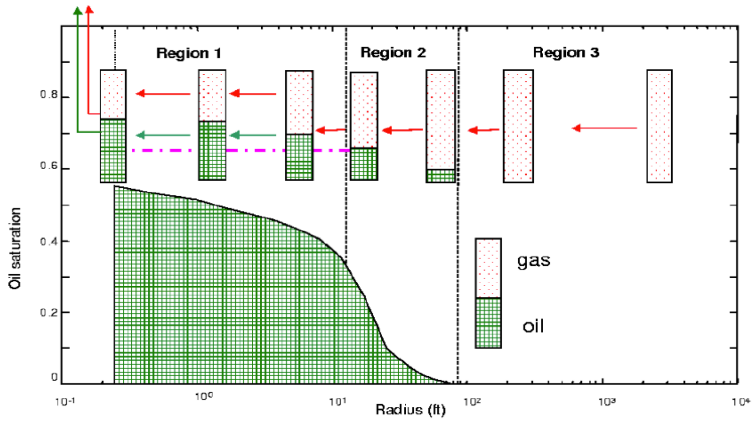

Figure 3.5: The three regions model of well drainage area under condensate banking effect (Fevang and Whitson 1996)

In shale gas systems, the three flow regions can be used for natural or propped fracture network. However, in shale matrix, only two regions can exist when the natural/propped fracture near to the matrix is below dew point: single-phase gas region (Region N°3) and condensate build-up region (Region N°2) due to the very low condensate relative permeability in shale matrix (see Figure 3.6). Due to high capillary pressure in nano-scale pores in shale matrix, all condensate formed in reservoir under dew point remains *immobile* or *trapped* (see Section 3.7.3). When pressure in central zone of matrix reaches dew point, all matrix is under Region N°2.

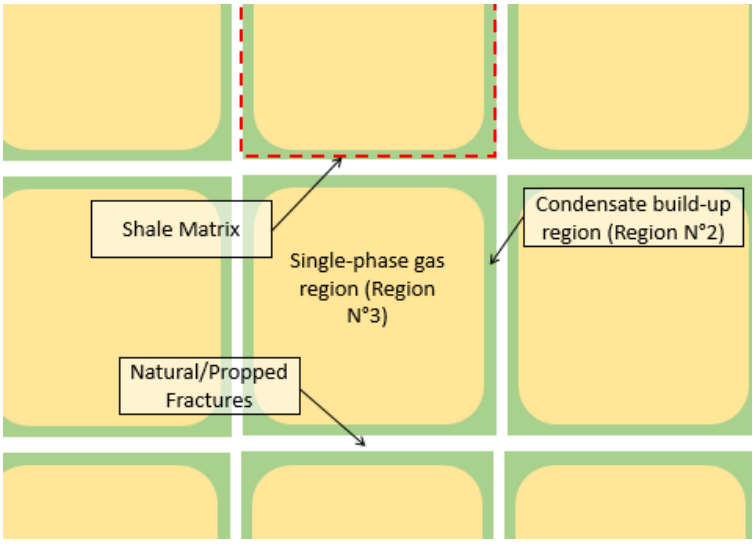

Figure 3.6: The two gas-condensate flow regions in shale matrix. Single-phase gas region in matrix central area with average pressure above the dew-point. Condensate build up region near natural/propped fracture where condensate starts to drop out but the flowing phase is only gas due to high capillary pressure

As in conventional reservoirs, condensate blockage reduces well productivity significantly when well matrix pressure falls below dew point. When condensate build-up in matrix, gas flow from this matrix decreases rapidly as pressure drops. Due to the several magnitude difference of permeability between matrix and hydraulic fracture, the conventional recovery enhancement techniques such as pressure maintenance by gas or water injection and huff-n-puff are not applicable. New techniques are needed to be developed and tested. Meanwhile, an accurate evaluation of condensate banking effect is crucial to predict well production and to allow for optimum well design that minimises the impact of condensate banking.

The condensate accumulation and propagation in the shale matrix are discussed further in Sections 5.5 and 6.4.1.

3.3.3 Gas Condensate Relative Permeability

As mentioned earlier, absolute permeability measurement poses a technical challenge with respect to relative permeability measurement with the known techniques (steady state, pulse decay and crushed samples methods).

In tight sand gas reservoirs, *Permeability Jail* concept is widely used to describe the relative permeability of gas and water in the low permeability sand. *Permeability Jail* consists of the existence of a saturation region where both gas and water become immobile (usually, permeability jail is defined by both K_{rg} and K_{rw} < 2%). This phenomenon is well observed in tight sands with absolute gas permeability less than 50 µD (Cluff and Byrnes 2010). Jail occurs as a result of capillary pressure in small pores filled by liquid blocking gas flow and reducing its relative permeability significantly. Figure 3.7 shows results by Cluff and Byrnes (2010) for gas relative permeabilities measurement for samples with absolute permeability ranging from 0.0001 mD to 1 mD.

Using pore network simulation, Silin (2011) obtained similar results for gas condensate flow in tight sand reservoirs. As condensate accumulates in small pores, capillary pressure inhibits condensate flow to larger pore size and reduces gas flow gradually with increasing condensate saturation.

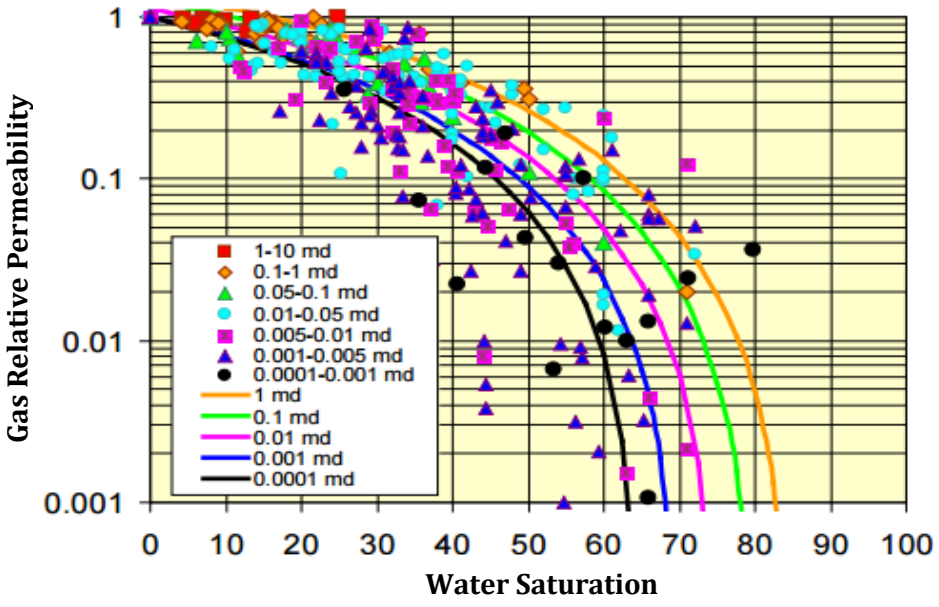

Figure 3.7: Gas relative permeabilities measured at single Sw for absolute permeabilities from 0.0001 mD to 1 mD (Cluff and Byrnes 2010)

3.3.4 Effect of Liquid Saturation on Slip/Knudsen Flow

The effect of liquid saturation on gas slip effect is well documented in the literature. Rose (1948) carried out gas–water core flooding experiments using synthetics materials and natural sandstone with intrinsic permeabilities ranging from 30mD to 800 mD (which are considered as conventional reservoirs). He found that the slippage effect decreased with increasing water saturation. Fulton (1951), Estes and Fulton (1956) and Sampath and Keighin (1982) used similar range of sandstone permeabilities and concluded to the same result. Rushing, Newsham and Fraassen (2003) extended Roses's work to tight gas reservoir using sandstone cores with permeability ranging from 0.01 to 0.1 mD and they validated the same effect of water saturation on slippage effect in tight reservoirs.

The effect of water saturation on gas slippage effect can be explained by the variation of pore size range that is accessible for gas flow as the water saturation increases. Due to capillary forces, when water saturation increase it occupies the smallest free pore size range, hence increasing the average pore size accessible by gas flow which reduces the gas slippage effect.

Recently, Wu et al.(2014) used a synthetic material to build a 1D nanoscale slit-like channels with 100 nm size to describe gas-water flow in shale matrix. However, their results contradicted the conclusions of Rose (1948), Sampath and Keighin (1982) and Rushing et al. (2003); they found that gas slippage effect increases as the water saturation increases. The main reason behind this result is that their 1D nano-channel network lacks the pore interaction and the pore size variation as in shale, tight sandstone and conventional sandstones cores used by the other researchers. Thus, the variation of pore size accessible by gas with increasing water saturation is not represented in their work.

To the best of the author's knowledge, no shale core two-phase flow measurement is reported in the literature. In this case, pore network modelling can be the best alternative to study the two-phase flow of gas and condensate in shale reservoirs.

3.4 Review of Pore Network Flow Modelling

Pore-network modelling is becoming a well-established discipline for petroleum applications for single and multi-phase flows in porous media. The pore network modelling was first introduced by Fatt (1956). Usually, the void in the porous media is represented by a 2D or 3D network of pores connected by pore throats. The network modelling has been used by researchers to study macroscopic properties of porous media such as permeability

and relative permeability linked to pore-level physics such as pore shapes, wettability, and interfacial tension.

For conventional reservoirs, traditionally, the pores are modelled as spheres or cubes and pore throats as curved triangular cross-section tubes. A variety of shapes were used in literature ranging from angular cross-section to grain boundary pores (Blunt 2001, Joekar-Niasar and Hassanizadeh 2012). The main challenge of an accurate network modelling is to capture the complexity of the pore space geometry while using simple pore shapes. For multiphase flow, the shapes of pores and pore throats are very important to describe the capillary pressure as function of wetting phase saturation. When a wetting phase exists in a pore, it occupies the pore corners with high capillary pressure. As saturation increases the capillary pressure decreases until it forms a bridge.

The extension of pore geometry from conventional reservoirs to shale reservoirs should be considered carefully due to the difference of pore space geometry. As discussed in Section 2.3.4, the shale porosity comprises organic porosity in kerogen and inorganic intergranular porosity. The pore space in organic matter (kerogen) tends to have mainly a round shape (Curtis, Ambrose and Sondergeld 2010) which is different from the triangular intergranular shape in conventional sandstone reservoirs. In addition, in inorganic matter, the slit-like pores should be also considered besides circular pores.

In conventional reservoirs, pore network modelling has been used to better understand gas-condensate flow in porous media. The pore network modelling studies focused mainly on condensate critical saturation and relative permeability evaluation and their relationship with capillary forces and wettability (Fang, et al. 1996, Jamiolahmady et al. 2000, Bustos and Toledo 2003, Li and Firoozabadi 2000). Even, at higher permeability (than shale matrix), researchers face difficulties for relative permeability measurement in laboratories.

For shale reservoirs, the situation becomes more complicated where reliable techniques for multiphase permeability are still under development and improvement. Currently, pore-network modelling is the only way to investigate multiphase flow in shale reservoirs. Few pore network studies were reported in the literature. Mehmani et al. (2013) used single phase gas pore network model to study the effect of Knudsen flow. However, they used an intergranular sandstone pore model. They concluded that the gas apparent permeability is sensitive to the fraction of nanopores. Huang et al. (2016) developed a two-phase (gas and water) 3D pore network model including Klinkenberg flow and gas adsorption. They used a mixed wettability network (with organic and no-organic pores) but they used a square cross-section for pores in kerogen which is not in line with experimental observation where nanopores have circular cross section (see Section 2.3.4).

3.5 Capillarity Induced Negative Pressure of Wetting Phase in Nanopores

In nanometre scale, the ratio of channel inner surface to volume increases significantly compared to the macrochannels which induces a large effect of tension forces on condensate pressure to the extent that it can be under negative pressure. In Young-Laplace equation (3.13), the condensate pressure is defined as a function of gas pressure and capillary pressure. When the capillary pressure is high enough (at low pore radius) to exceed the gas pressure, the condensate pressure becomes negative.

$$P_c = P_g - P_{cap} = P_g - \mathrm{C}\,\frac{\sigma_{gc}\,cos\theta}{R} \tag{3.13}$$

where P_g and P_c are pressure in gas phase and condensate phase respectively (psi), P_{cap} is capillary pressure (psi) σ_{gc} is gas-liquid interfacial tension (IFT) (mN/m), θ represents the gas-condensate contact angle. R is the pore radius (m) and C=1.449×10^{-7} is a constant.

An upper pore radius limit R_{neg} for pore with negative condensate pressure (i.e. $P_c(R) < 0$ when $R < R_{neg}$) can be defined as

$$R_{neg} = \mathrm{C}\frac{\sigma_{gc}\,cos\theta}{P_g} \tag{3.14}$$

The negative wetting phase induced by capillary pressure is still under investigation in nanofluidics (Ondarçuhu and Aimé 2013). The Young-Laplace equation extension to nanoscale level (about 100 nm) was proven experimentally by Sobolev et al. (2000). Tas et al. (2003) observed two phase (water and air) flow in hydrophilic silicon nanochannels and used Young-Laplace equation to identify negative water pressure.

3.6 Gas-Condensate Flow Modelling in Shale Matrix

3.6.1 Pore Size Distribution in Shale Matrix

From the literature, a number of experiments were reported on the application of Mercury Injection Capillary Pressure technique (MCIP) to determine the pore size distribution (Lewis, et al. 2013, Kuila 2013, Saidian 2014, Ross and Bustin 2009, Al Hinai et al. 2014, Crousse, et al. 2015). Figure 3.8 represents the incremental pore space fraction vs. pore radius for four samples from Eagle Ford Shale (adapted from Lewis, et al.(2013)). In this Figure, pore radius extends from 3nm up to 300 nm with a logarithmic bell-shape around 10 to 40 nm similar to log normal distributions. Figure 3.9 shows an approximation of Lewis,

et al.(2013) data (Sample 4) to a log normal distribution ln $\mathcal{N}(10\ ,0.6)$ for incremental and cumulative pore space vs. pore radius.

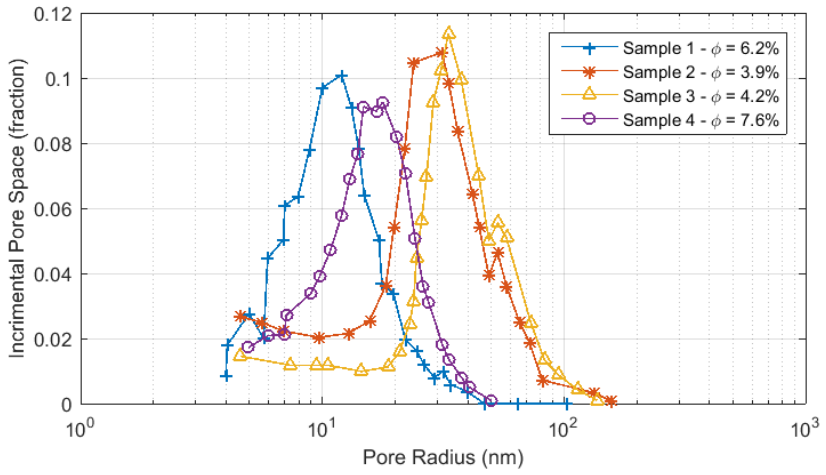

Figure 3.8: Incremental pore space vs. pore radius of four samples of lower Eagle Ford Shale (adapted from Lewis, et al. (2013)).

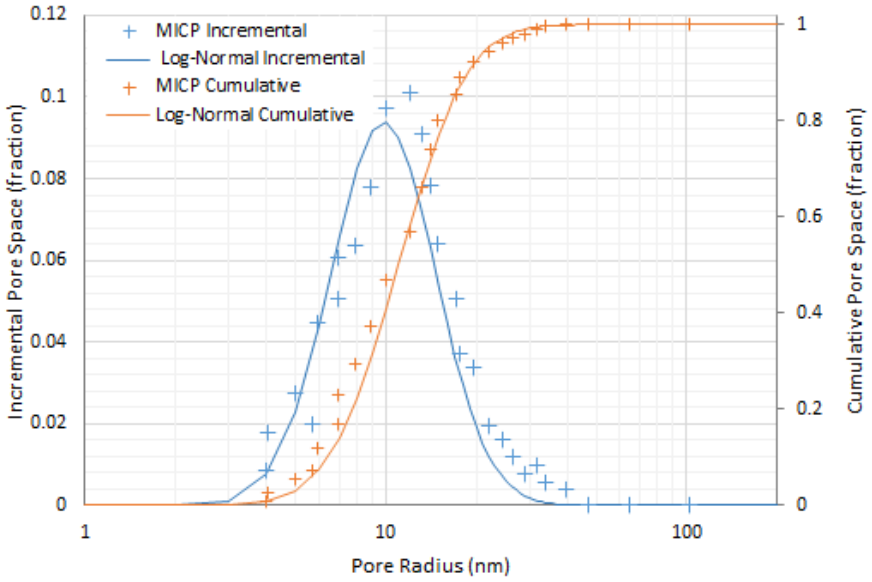

Figure 3.9: Approximation of measured data of Mercury Injection Capillary Pressure (MICP) of Sample 1 to a log normal distribution ln $\mathcal{N}(10\ ,0.6)$ in terms of incremental pore space and cumulative pore space vs. pore radius.

3.6.2 Description of the Pore Space

In this study, porous media in shale matrix kerogen is modelled as three-dimensional cubic network of connected pore segments. Nodes connection segments are valueless and have infinite connectivity. Each pore segment connecting nodes *i* and *j* is modelled as nanotubes

with radial cross section of radius R_{ij} and constant length L (see Figure 3.10). Nanotubes radii are assigned randomly according to a log-normal distribution $\ln \mathcal{N}(v, s)$ of mean v and standard deviation s. The 3D structure has connection factor 6 and N nodes; each node is connected to next nodes in *X, Y* and *Z* directions. Figure 3.11 illustrates a nanotube and an 8×8×8 pore network structure. Figure 3.12 shows the pore radius distribution of $\ln \mathcal{N}(10, 0.6)$ network and the theoretical log normal PDF used to generate it randomly. The dimension in X, Y and Z direction is 1 µm and porosity is 0.08.

The PDF (Probability Density Function) for R can be written as:

$$f(R) = \frac{\sqrt{2}\exp\left[-\frac{1}{2}\left(\frac{\ln R - \ln v}{s}\right)^2\right]}{\sqrt{\pi}\, s\, R\left[\operatorname{erf}\left(\frac{\ln R_{max} - \ln v}{\sqrt{2}s}\right)\operatorname{erf}\left(\frac{\ln R_{min} - \ln v}{\sqrt{2}s}\right)\right]} \tag{3.15}$$

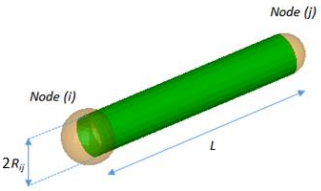

Figure 3.10: Modelling a nanotube (in green) connecting two nodes (in orange)

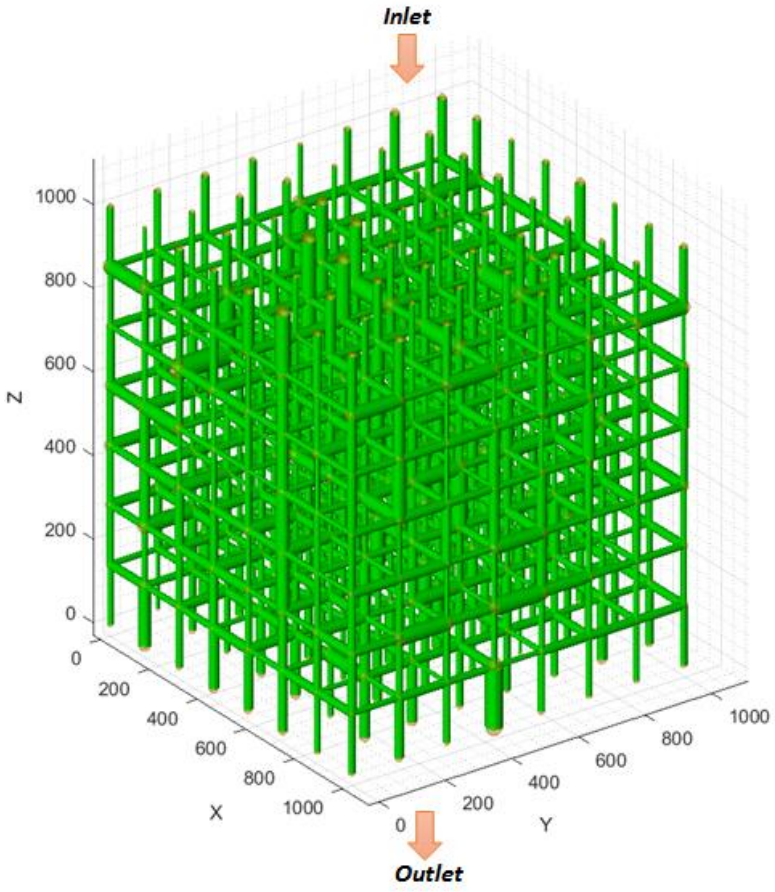

Figure 3.11: Example of a 3D structure pore network with connection factor 6 and 512 nodes with inlet and outlet indicated (dimensions in nm).

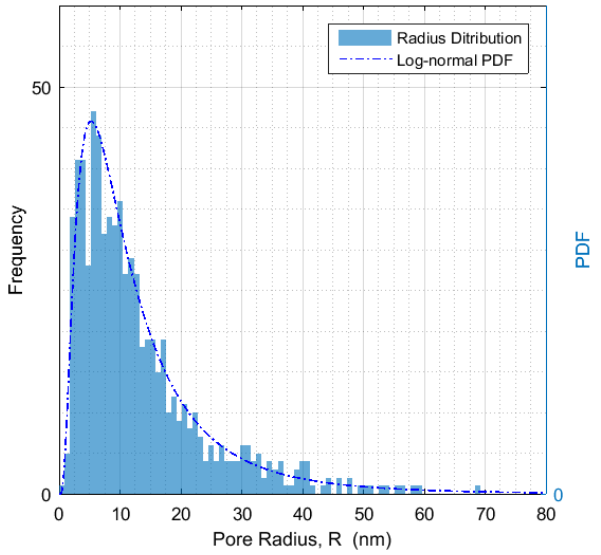

Figure 3.12: Pore radius distribution of the pore network: Histogram of pore radius and PDF of $\ln \mathcal{N}(10, 0.6)$ fitting the pore radius distribution.

A gas condensate sample is defined in Table 3.2. Figure 3.13 displays the Constant Volume Depletion (CVD) liquid drop-out and Interfacial tension (IFT) used in the simulation generated using a PVT-i package for gas condensate fluid. The sample can be defined a medium-rich gas condensate fluid with maximum liquid dropout of 21.8% and dew point of 4250 psi. The CVD experiment mimics the fluid flow in shale reservoir where only gas flows in the two phase region (see Section 3.7.3).

Table 3.2: Gas condensate sample composition used in simulations.

Components	Mol Fraction (%)	Mol Weight
C1	70	16.0
C2	9	30.1
C3	6	44.1
C4	6	58.1
C5	2	72.2
C6	1	84.0
C7+	6	167

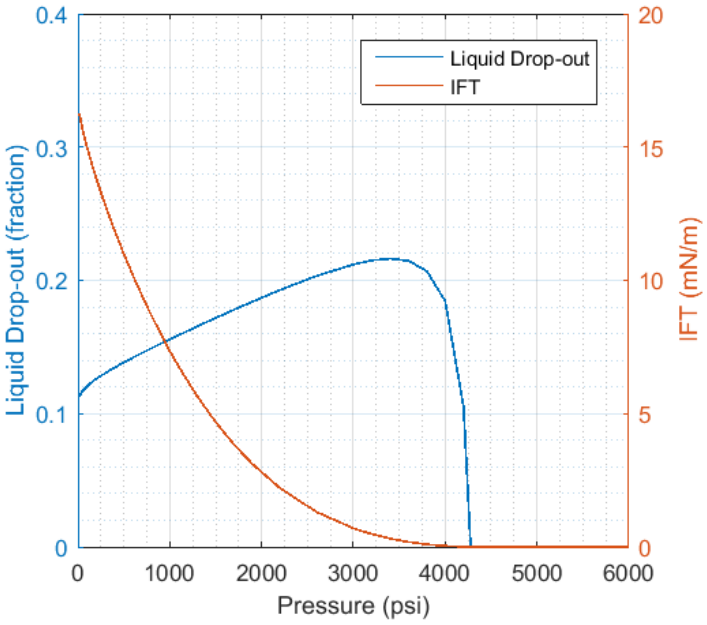

Figure 3.13: Liquid Drop-out and IFT of gas condensate Constant Volume Deletion (CVD) simulation.

3.6.3 Flow Modelling

The gas flow through nanotubes connecting two nodes i and j is described by a modified Hagen-Poiseuille equation established in this work as

$$\Delta P_{ij} = \begin{cases} \frac{1}{\xi_{ij}} \left[\frac{8}{\pi} \frac{\mu_{ij}^{g} L_{ij} q_{ij}^{g}}{R_{ij}^{4}}\right] for\ gas \\ \left[\frac{8}{\pi} \frac{\mu_{ij}^{c} L_{ij} q_{ij}^{c}}{R_{ij}^{4}}\right] for\ condensate \end{cases} \quad i = 1..N, j = 1..N \tag{3.16}$$

where q_{ij} is phase flow rate (m³/s), ΔP_{ij} is differential pressure (Pa), $R_{ij}$is tube radius (m), μ_{ij} is phase viscosity (cp) and L_{ij} is tube length (m); superscripts g and c stand for gas and condensate respectively. The gas permeability correction factor of nanotube ξ_{ij} is defined by Equation (3.17)

$$\xi_{ij} = \left(1 + \alpha_{ij} Kn_{ij}\right)\left(1 + \frac{4Kn_{ij}}{1 - Kn_{ij}}\right) \quad i = 1..N, j = 1..N \tag{3.17}$$

where Kn_{ij} is the nanotube's Knudsen number defined in Equation (3.1).

A nanotube conductivity for gas is defined as

$$G_{ij}^{g} = \frac{q_{ij}^{g}}{\Delta P_{ij}} = \xi_{ij} \frac{\pi R_{ij}^{4}}{8\, \mu_{ij}^{g} L_{ij}} \quad i = 1..N, j = 1..N \tag{3.18}$$

And for condensate, as

$$G_{ij}^{c} = \frac{q_{ij}^{c}}{\Delta P_{ij}} = \frac{\pi R_{ij}^{4}}{8\,\mu_{ij}^{c}\,L_{ij}} \qquad i = 1..N, j = 1..N \tag{3.19}$$

The gas flow through the pore network is governed by mass conversion of gas and condensate in each node (i , j)

$$\sum_{j=1}^{N} q_{ij}^{g} = 0 \text{ and } \sum_{j=1}^{N} q_{ij}^{c} = 0 \qquad i = 1..N \tag{3.20}$$

Equation (3.20) can be written using Equation (3.18) as

$$\sum_{j=1}^{N} G_{ij}^{g}\,\Delta P_{ij} = 0 \text{ and } \sum_{j=1}^{N} G_{ij}^{c}\,\Delta P_{ij} = 0 \quad i = 1..N \tag{3.21}$$

Replacing ΔP_{ij} by $P_i - P_j$ gives

$$P_i \sum_{j=1}^{N} G_{ij}^{g} - \sum_{j=1}^{N} G_{ij}^{g}\,P_j = 0 \quad \text{and} \quad P_i \sum_{j=1}^{N} G_{ij}^{c} - \sum_{j=1}^{N} G_{ij}^{c}\,P_j = 0 \quad i = 1..N \tag{3.22}$$

A code was written in Matlab to generate the 3D pore network, calculate volumetric functions and solve the system of equations (3.22) using iterative Newton-Raphson method for unknown vector P_i. Figure 3.14 represents a flow diagram of the code. This code is provided in an attached CD-ROM.

3.6.4 Condensate Accumulation

As pressure drops, condensate builds up in the pore network and start filling small pores. Due to capillary pressure, all pores lower than the minimum free pore for gas flow, $R_{g,min}$ are considered blocked to gas flow.

$$G_{ij} = \begin{cases} \xi_{ij}\dfrac{\pi R_{ij}^{4}}{8\mu_{ij}L_{ij}}, & R_{ij} \geq R_{g,min} \\ 0, & R_{ij} < R_{g,min} \end{cases} \tag{3.23}$$

A volume function is used to calculate $R_{g,min}$ as function of condensate saturation S_c based on the pore distribution and volumes.

$$R_{g,min} = f(S_c) \tag{3.24}$$

Where $R_{g,min}$ and S_c can be related in discretised version

$$S_c(R_{g,min}) = \frac{\sum_{R_{min}}^{R_{g,min}} {R_{ij}}^2}{\sum_{R_{min}}^{R_{max}} {R_{ij}}^2} \tag{3.25}$$

Figure 3.15a and 3.15b illustrate results of generated $R_{g,min}$ and capillary pressure respectively as function of condensate saturation S_c of a pore network of *8×8×8* nodes and pore size distribution $\ln \mathcal{N}$ (10,0.6). Figure 3.16 represents an example of pore network with blocked pores in red and free pores in green at maximum condensate saturation of 22%.

Results of CVD in terms of μ, compressibility factor Z and average gas molecular mass M as a function of pressure is used to calculate conductivities G_{ij}.

As the condensate accumulates at the smallest range of pore size distribution, which mainly exists in the kerogen, the interface of gas-condensate is located in kerogen pores and controlled by their round cross section. In addition, the kerogen pore space accounts for about 50% of total porosity (refer to Section 2.3.4) enough to hold the condensate saturation. Consequently, the slit-like shape of non-organic pore space which represents the upper range of pore size distribution, has a minor impact on condensate accumulation vs $R_{g,min}$ relationship. As a result, the non-organic pores can be modelled with a circular cross section without having an impact on calculation results.

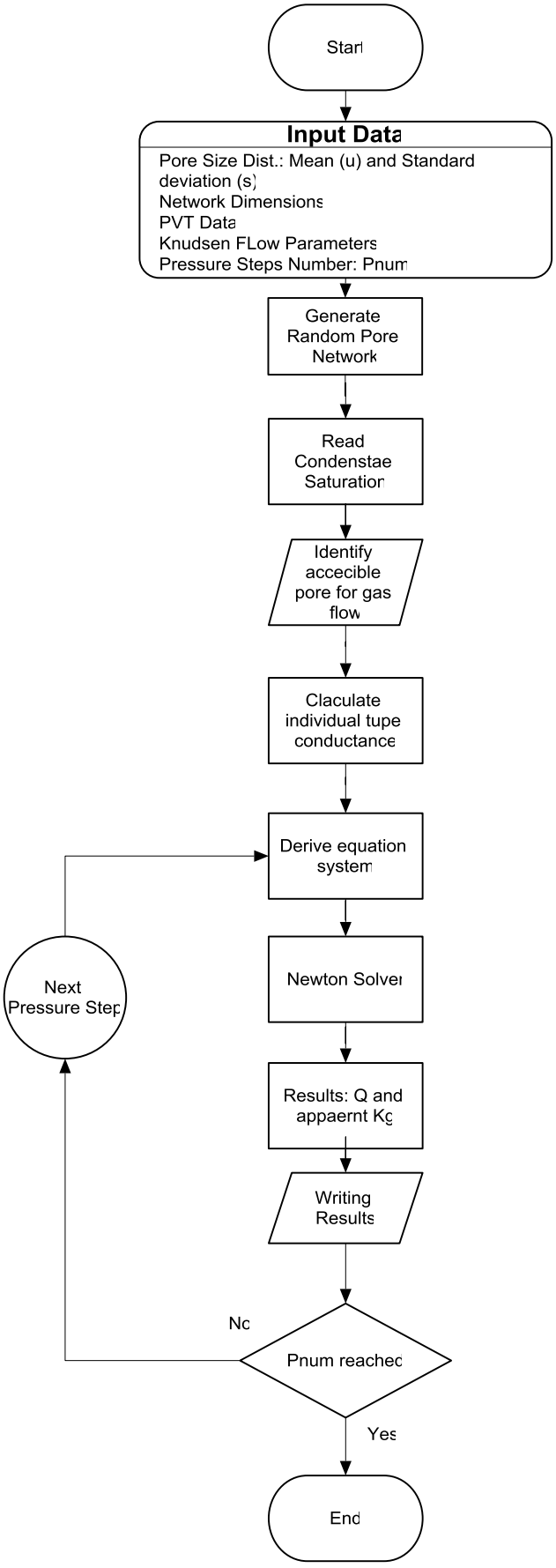

Figure 3.14: Flow diagram of the flow modelling calculation

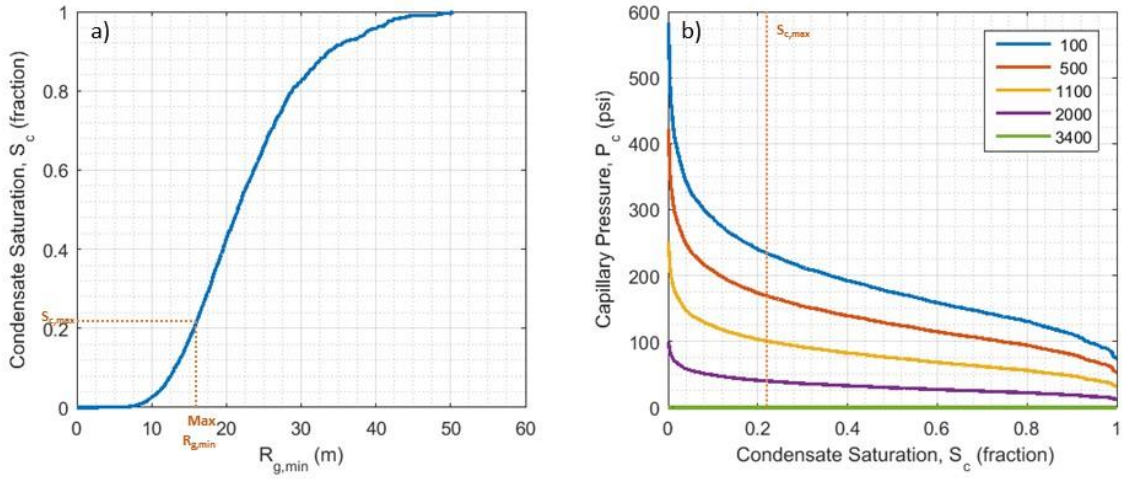

Figure 3.15: Saturation function and capillary pressure of a pore network of 8×8×8 nodes and ln $\mathcal{N}(10, 0.6)$: a) Condensate saturation S_c as function of $R_{g,min}$ showing maximum condensate saturation is related to $R_{g,min}$ of 16nm, b) Capillary pressure as function of saturation and for different pressure values.

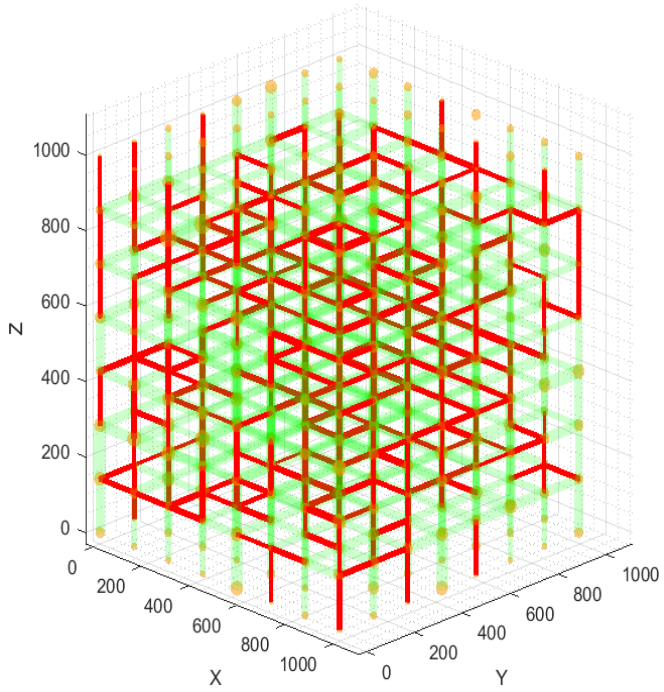

Figure 3.16: An example of pore network with blocked pores in red and free pores in green at maximum condensate saturation of 22% (dimensions in nm).

At each pressure value, the gas R_{min} is determined for the corresponding condensate saturation. The individual G_{ij} conductivities are calculated using equations (3.24) and (3.25).

3.6.5 Network Gas Apparent Permeability and Relative Correction Factor Calculation

The gas Darcy permeability and apparent permeability of the pore network are calculated as

$$k_{app} = \frac{q_{app}\mu_{avg}L}{P_i - P_o} \tag{3.26}$$

And

$$k_D = \frac{q_D\mu_{avg}L}{P_i - P_o} \tag{3.27}$$

where q_{app} and q_D are the apparent and Darcy gas flowrates respectively, μ_{avg} is the pore network average viscosity, L is the pore network dimension in flow direction and P_i and P_o are inlet and outlet pressure respectively.

The enhancement factor is calculated as

$$\xi = \frac{k_{app}}{k_D} \tag{3.28}$$

In order to emphasise the effect of condensate blockage on correction factor, gas condensate correction factorξ_{GC} and dry gas correction factor ξ_{DG} are calculated as

$$\xi_{GC} = \frac{k_{app,GC}}{k_{D,GC}} \quad \text{and} \quad \xi_{DG} = \frac{k_{app,DG}}{k_{D,DG}} \tag{3.29}$$

Where $k_{app,GC}$ and $k_{D,GC}$ are apparent Knudsen permeability and Darcy permeability with condensate blockage respectively, and $k_{app,DG}$ and $k_{D,DG}$ are apparent Knudsen permeability and Darcy permeability of dry gas respectively.

In order to evaluate the effect of condensate saturation on Knudsen flow, a new parameter is defined "Relative Correction factor" ξ_{rel} which is the ratio of ξ_{GC} to ξ_{DG}

$$\xi_{rel} = \frac{\xi_{GC}}{\xi_{DG}} \tag{3.30}$$

ξ_{rel} is a measure of the effect of condensate blockage on Knudsen flow and it can be used to adjust correction factor from dry gas flow to gas condensate flow. ξ_{rel} for Knudsen flow can be perceived as the equivalent of gas relative permeability k_{rg} for Darcy flow.

So the gas apparent permeability in the presence of condensate in shale matrix can be calculated as

$$k_{gapp}(S_c, P) = \xi_{rel}\xi_{DG}\, k_{rg}\, k_{\infty} \tag{3.31}$$

where k_{∞} is the intrinsic permeability

3.7 Results and Discussion

3.7.1 Intrinsic Permeability

Table 3.3 shows the result of intrinsic permeability for shale matrix as a function of varying ν (4 to 100 nm) and s (0.001 to 0.7 nm) with porosity ϕ of 6% and tortuosity τ of 1.5. The range of pore radius distribution of shale matrix identified with permeability between 20 and 1000 nD is indicated with green background. In this work, only (ν , s) values included in shale intrinsic permeability range will be used for matrix modelling.

Table 3.3: Calculated intrinsic permeability as function of varying ν and s with porosity ϕ 6% and tortuosity τ of 20. Shale matrix permeability range between 20 and 1000 nD is indicated in green background.

		s (nm)							
		0.001	0.1	0.2	0.3	0.4	0.5	0.6	0.7
ν (nm)	4	5	5	6	9	13	23	44	96
	6	11	12	14	20	30	51	99	216
	8	20	22	26	35	53	91	176	383
	10	32	34	40	54	83	142	275	599
	12	46	48	58	78	119	204	395	862
	14	62	66	79	106	162	278	538	1173
	16	81	86	103	139	212	363	703	1532
	18	102	109	130	176	268	460	890	1937
	20	126	134	161	217	331	568	1098	2390
	30	285	303	362	489	744	1277	2470	5318
	40	506	538	644	869	1323	2271	4386	9244
	50	792	841	1006	1358	2067	3548	6832	13961
	60	1140	1210	1449	1956	2977	5108	9778	19246
	70	1552	1647	1972	2662	4052	6950	13178	24890
	80	2027	2152	2576	3477	5293	9072	16976	30722
	90	2565	2723	3260	4401	6698	11467	21105	36605
	100	3166	3362	4025	5434	8270	14128	25496	42441

3.7.2 Single Phase Gas Flow

Calculated apparent permeability for 100% methane gas is presented in Figure 3.17. The enhanced gas permeability remains relatively stable near to intrinsic permeability (275 nD) above 1000 psi and starts to increase sharply as pressure decreases to reach around 2000 nD at 14.7 psi.

Figure 3.18 represents a log-log plot of numerical ξ calculated with 3D pore network vs. analytical correction factor ξ_{Michel} proposed by Michel et al (2011) (see equation (3.13)) for

methane flow in porous media with ranges of v (from 8 nm to 50 nm) and s (from 0.1 to 0.7) . It shows a good match of R^2-value=0.98.

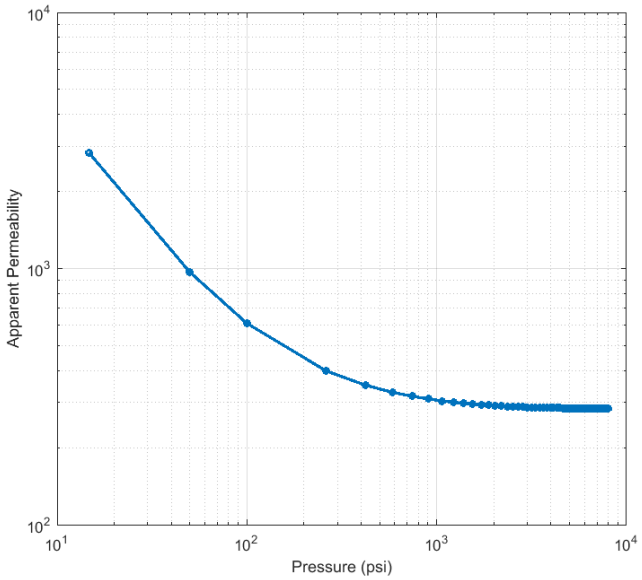

Figure 3.17: Apparent permeability (nD) for ln $\mathcal{N}(10\ ,0.6)$ pore radius distribution and 100% methane gas at reservoir temperature of 393°K

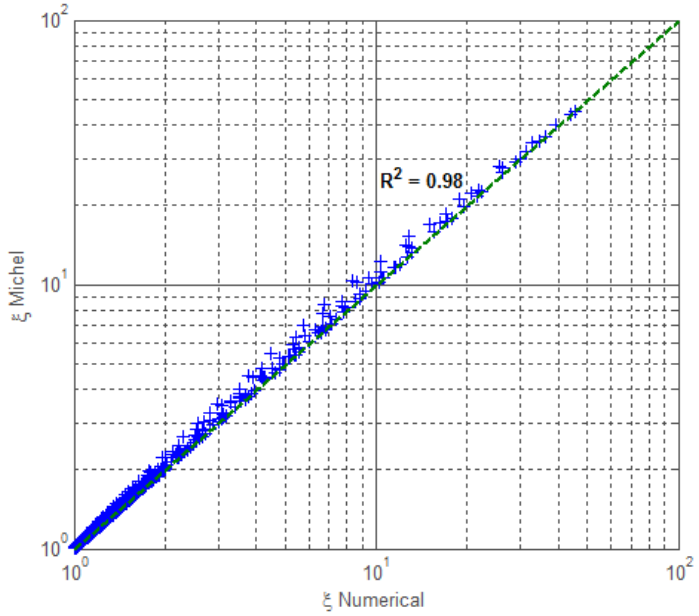

Figure 3.18: Log-log plot of numerical ξ vs. analytical ξ_{Michel} showing a good match of R^2-value=0.98.

3.7.3 Condensate Trapping

In order to investigate the effect of capillary pressure, two nanotube T_1 and T_2 with radii R_1 and R_2 respectively were adopted for analysis (see Figure 3.19) where condensate exists in $Tube_1$. The condensate will flow to $Tube_2$ if

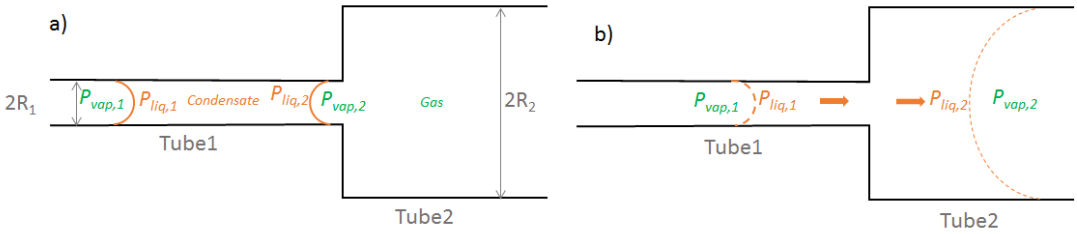

Figure 3.19: Schematic of condensate flow from one nanotube to another: a) immobile condensate in Tube1, trapped by capillary pressure, b) condensate flowing from Tube1 to Tube2.

$$\Delta P = P_{liq,1} - P_{liq,2} > 0 \tag{3.32}$$

Where $P_{vap,1}$ and $P_{vap,2}$ are gas pressure in Tube1 and Tube2 respectively and they can be expressed as

$$P_{liq,i} = P_{vap,i} - P_{cap,i} \quad i = 1,2 \tag{3.33}$$

where P_{cap} is the capillary pressure. Condition (3.32) can be rewritten as

$$P_{vap,1} - P_{vap,2} > P_{cap,1} - P_{cap,2} \tag{3.34}$$

We define $P_{cap,1} - P_{cap,2}$ as the differential pressure threshold ΔP_{thr} for condensate flow from Tube1 to Tube2

$$\Delta P_{thr} = P_{cap,1} - P_{cap,2} = \sigma_{gl} \cos\theta \left(\frac{1}{R_1} - \frac{1}{R_2}\right) \tag{3.35}$$

From equation (3.35), maximum and minimum ΔP_{thr} at pore radius R are defined by capillary pressure difference between a pore radius R and highest pore radius connected tube, and lowest pore radius connected tube. Figure 3.20 illustrates the evaluation of maximum and minimum ΔP_{thr} for pore radius range between 3 and 50nm at 500 and 3600 psi. Minimum and maximum ΔP_{thr} were evaluated at between two tubes of $R_1 = 50$nm and $R_2 = R_1 + 1nm$ respectively. Results are presented at low and high reservoir pressure values of 500 and 3600 psi to emphasise low and high IFT effect and to cover pressure range from reservoir to near well bore area.

In pore radius range less than 20nm where condensate is expected to build up, minimum ΔP_{thr} is more than 8 psi for reservoir pressure 500psi and more than 0.1 psi for reservoir pressure 3600psi.

For the pore network defined in Section 3.6.2 the minimum ΔP_{thr} is calculated numerically for a range of reservoir pressures. For each nanotube with condensate saturation, ΔP_{thr} is evaluated for a potential condensate flow to the connected nanotube with the lowest radius. Figure 3.21 and 3.19 shows minimum ΔP_{thr} of pore network at 60, 500, 3000, 4200 psi. At 4200psi with IFT of 0.18 mN/m minimum ΔP_{thr} average is around 0.1 psi and around 100 psi at 500 psi where IFT is 11.73 mN/m.

In order to compare ΔP_{thr} to pressure values applied on shale matrix in the field. A maximum reservoir pressure of 8000 psi, a minimum bottomhole pressure of 500 psi and a minimum shale matrix dimension of 10×10×10 ft are considered and that results to a maximum differential drainage pressure ΔP of 3e-3 psi applied on the shale matrix block.

Comparing this levels of minimum ΔP_{thr} to the maximum differential drainage pressure in the field of 3e-3 psi (see Figure 3.20 and Figure 3.21), one can conclude that *all* condensate that forms in the matrix remains immobile (trapped). In near wellbore area, where reservoir pressure is around 500 psi, condensate trapping is more pronounced, as illustrated in Figure 3.21 making condensate banking effect severer around wellbore than deep reservoir.

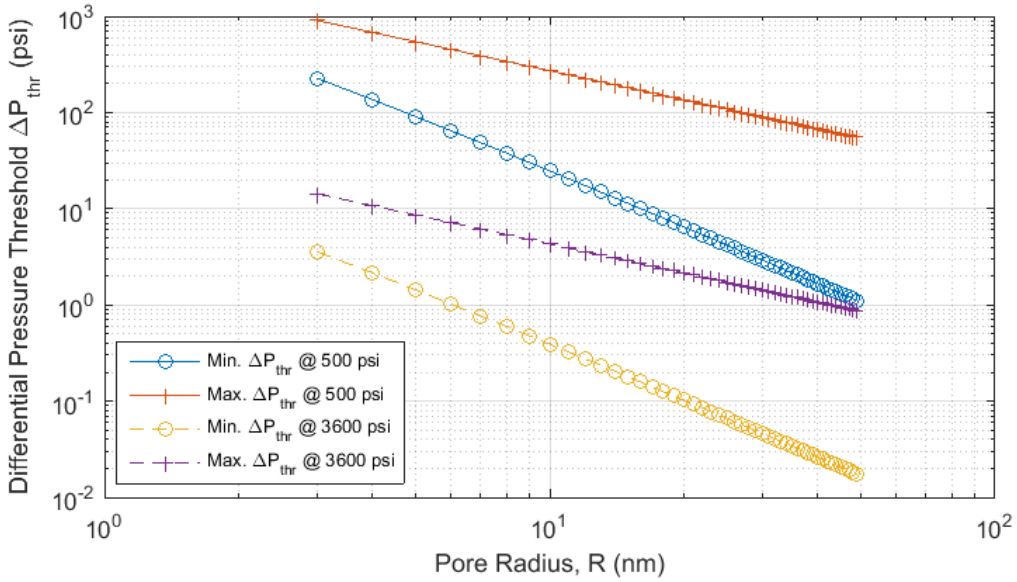

Figure 3.20: Minimum and maximum differential pressure threshold ΔP_{thr} of condensate fluid for pore radius range from 3 to 50nm at 500 psi and 3600 psi. Minimum and maximum ΔP_{thr} were evaluated at between two tube of R at 50nm and R at (R+1nm) respectively.

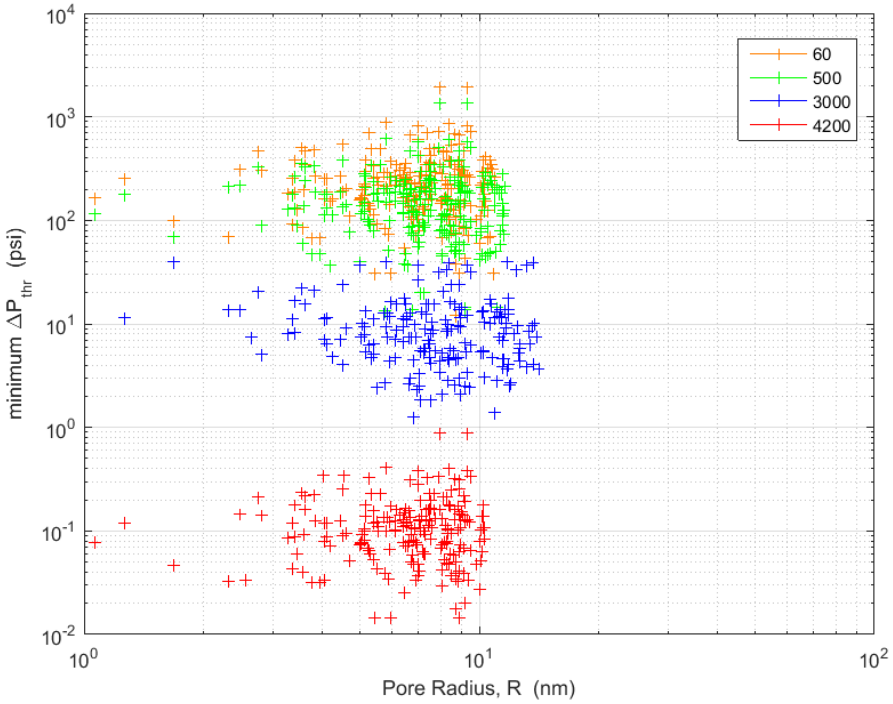

Figure 3.21: Minimum ΔP_{thr} vs. pore radius of pore network at 60, 500, 3000, 4200 psi.

3.7.4 Effect of Condensate Saturation on Gas Apparent Permeability

Using the pore network model, three numerical experiments were carried out on:

a) Darcy flow: where ξ_{ij} = 1,
b) Knudsen flow with condensate blockage effect using $R_{g,min}$ defined by equation (3.24).
c) Knudsen flow for dry gas: where gas permeability is calculated without condensate blockage i.e. $R_{g,min} = R_{min}$. In this exponent, the same PVT data of CVD is used for viscosity, Z-factor and gas molecular weight.

The results of Darcy relative permeabilities of gas and condensate are presented in Figure 3.22. Despite the simplicity of the pore network, the gas relative permeability results are similar to results reported by Cluff and Byrnes (2010) in tight sands. The gas permeability declines rapidly as the condensate saturation increases to reach a very low critical saturation of 28% while the condensate remains immobile to very low relative permeability in this range. This result indicates the severity of condensate banking effect on shale gas well derivability. Nevertheless, it is expected that the relative permeability of condensate in shale matrix is much lower than presented in Figure 3.22 due to the upscaling problem. At macroscale level the condensate phase would have more discontinuity than in microscale level (in micrometre range, as presented in this work) leading to a higher critical saturation and a more concave relative permeability presented by the dashed line in Figure 3.22.

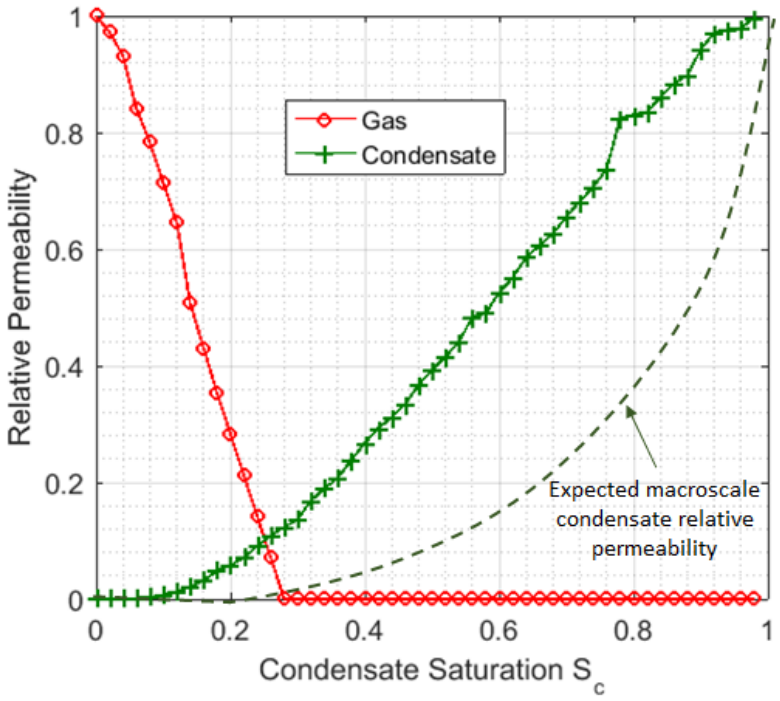

Figure 3.22: Gas Darcy relative permeability and condensate relative permeability results of pore network simulation.

Figure 3.23 represents the permeability results for the three experiments carried out in this work using an 8×8×8 network with ln $\mathcal{N}(10, 0.6)$ pore size distribution. Darcy permeability graph reflects the effect of condensate blockage on gas flow below dew point pressure. The permeability reduction is caused by the loss of permeability of tubes with radius less than $R_{g,min}$. Knudsen permeability graph shows a similar decline below dew point but an enhanced permeability with decreasing pressure where Knudsen flow is more important. In addition, Knudsen dry gas permeability (without condensate blockage is plotted against Knudsen permeability (with condensate blockage).

Figure 3.24 gives the correction factor ξ_{GC} under condensate blockage effect as compared to dry gas correction factor ξ_{DG} . The difference between ξ_{GC} and ξ_{DG} is caused by the loss of the contribution of the pores with radius below $R_{g,min}$ to Knudsen flow under condensate blockage.

Figure 3.25 illustrates ξ_{rel} as function of pressure. As pressure drops below dew point, ξ_{rel} starts to decrease reflecting the reduction of Knudsen flow in pores with condensate blockage. The lower pore radii (blocked with condensate) have an increasing contribution to the total Knudsen flow with decreasing pressure which explains the decline of ξ_{rel}. In this example ξ_{rel} reaches lower value of 0.87 at 14.7 psi. The effect of condensate blockage

should be considered in correction factor calculation so that Knudsen gas permeability in shale matrix is not overestimated.

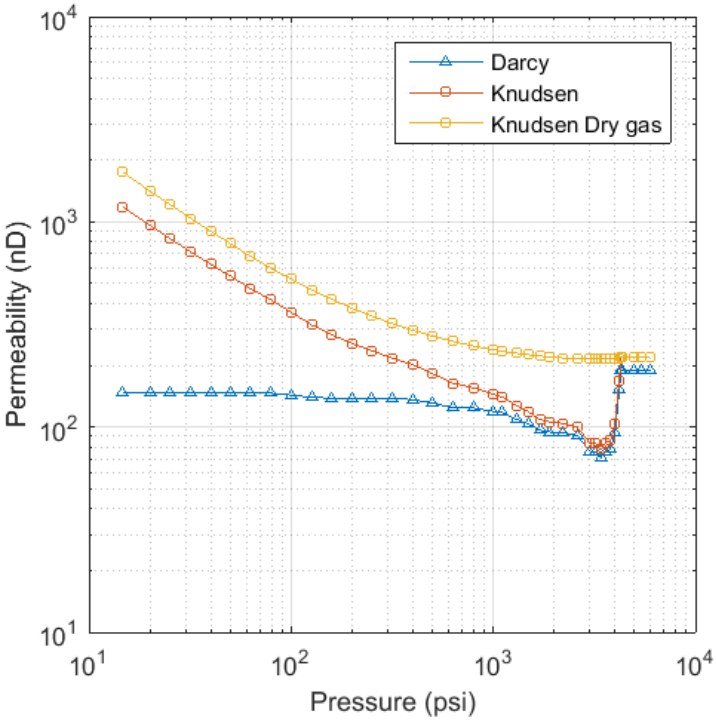

Figure 3.23: Pore network permeabilities Darcy flow and Knudsen flow and Knudsen dry gas flow as function of pressure for ln $\mathcal{N}(10, 0.6)$

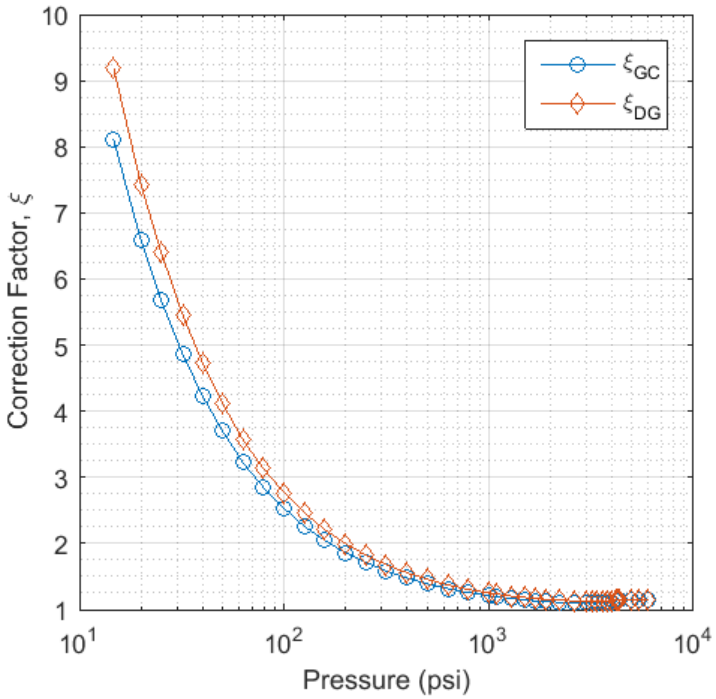

Figure 3.24: Correction factors ξ_{GC} and ξ_{DG}

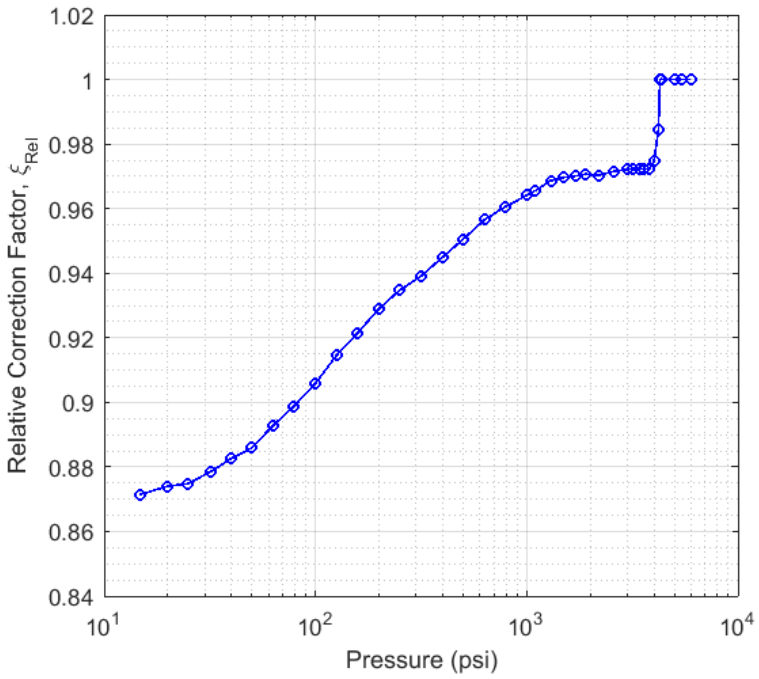

Figure 3.25: Relative Correction Factor ξ_{rel} for pore size distribution of ln $\mathcal{N}(10, 0.6)$

In order to investigate the relationship between condensate saturation, pressure and ξ_{rel}, the simulation was carried out at different pressure values: 14.7, 100, 500, 1000, 2000 psi. At each reservoir pressure value, the condensate saturation extended (beyond the unique value of CVD) to range from 0 to maximum drop out of 22% and results are given in Figure 3.26. This figure shows that at the same pressure ξ_{rel} decreases with increasing condensate saturation which can be explained by the blockage of the lower part of pores range by the condensate hence reducing the effect of Knudsen flow. In addition, this relationship between condensate saturation and ξ_{rel} is affected by pressure. The lower the pressure the higher the effect of condensate saturation on ξ_{rel}.

In order to evaluate the contribution of the different pore size ranges and how it affects ξ_{rel}, two parameters are defined: the Class Contribution (CC) C_m^{δ} and Relative Change of Contribution (RCC) ΔC_m. The pore size distribution is divided into 100 pore size classes and contribution of each class (m) is expressed as a function of pressure; C_m^{δ} in the dry gas flow was calculated for Darcy flow and Knudsen flow using Equation (3.36).

$$C_m^{\delta}(P) = \frac{\sum_{i,j}\left[q_{ij}^{g}\right]}{\frac{\sum_{j=1}^{N}\sum_{j=1}^{N} abs\left[q_{ij}^{g}\right]}{2}}, tube\ (i,j) \in\ C_m, m = 1..N_{class} \tag{3.36}$$

where δ= D or Kn, refers to the flow type Darcy or Knudsen flow respectively and N_{class} is the classes number. The relative change of Class Contribution $\Delta C_m$was calculated using Equation (3.37).

$$\Delta C_m(P) = \frac{C_m^{Kn}(P) - C_m^{D}(P)}{C_m^{D}(P)} \, , m = 1..N_{class} \tag{3.37}$$

ΔC_m is a measure of the contribution variation of each pore size class with pressure.

Figure 3.27a shows the contribution of pore radius ranges to total gas flow rate for Darcy dry gas simulation whilst Figure 3.27b shows the relative change of this contribution for different pressure values (14.7 100, 500, 1000 and 2200 psi). These figures depict the increase of the contribution of the lower range of pore size.

The contribution pattern shifts with pressure i.e. at low pressure (250, 60 and 14.7 psi) lower pore sizes (under 12nm) contribute more than at high pressure (1000 and 2000 psi). When these pores are blocked, the correction factor ξ_{GC} decreases as a function of decreasing pressure, reflecting the loss of Knudsen flow contribution of these pores.

As a result, the Knudsen flow under condensate banking effect should be expressed as a function of both condensate saturation and reservoir pressure using the relative correction factor as

$$\xi_{rel} = f(S_c, P) \tag{3.38}$$

Equation (3.38) reflects the effect of pore size distribution on Knudsen flow under condensate banking effect. The saturation controls the range of pore sizes accessible by gas flow and pressure affects the contribution of these pore sizes to the total Knudsen flow. Using the results presented in Figure 3.26, the following formulation of ξ_{rel} was derived

$$\xi_{rel} = 1 - \frac{a}{P^b} \, (S_c)^n \tag{3.39}$$

where n, a and b are parameters of the pore distribution. For data used in this work estimated parameters value are shown in Table 3.4. Figure 3.28 shows ξ_{rel} values from correlation in Equation (3.39) plotted against values obtained from simulations with R^2 =92%.

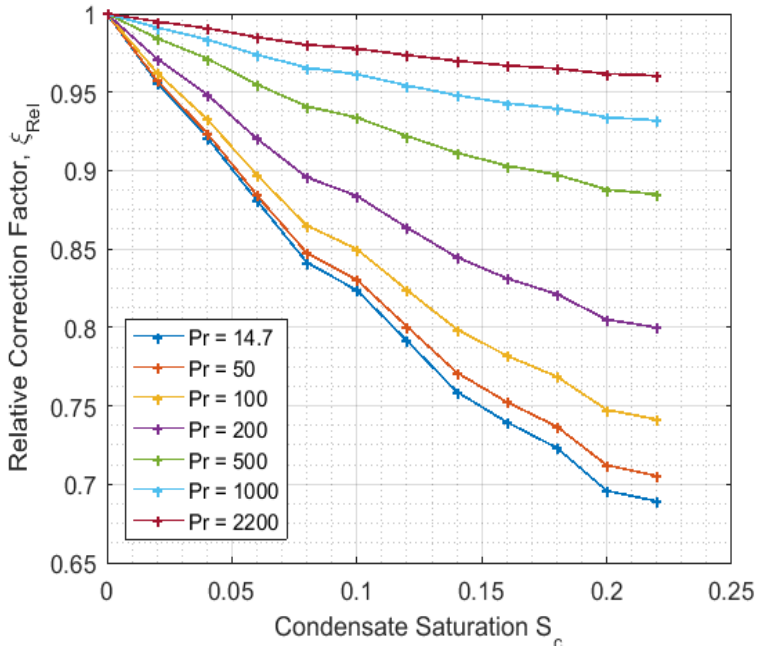

Figure 3.26: ξ_{rel} vs. condensate saturation for different reservoir pressures.

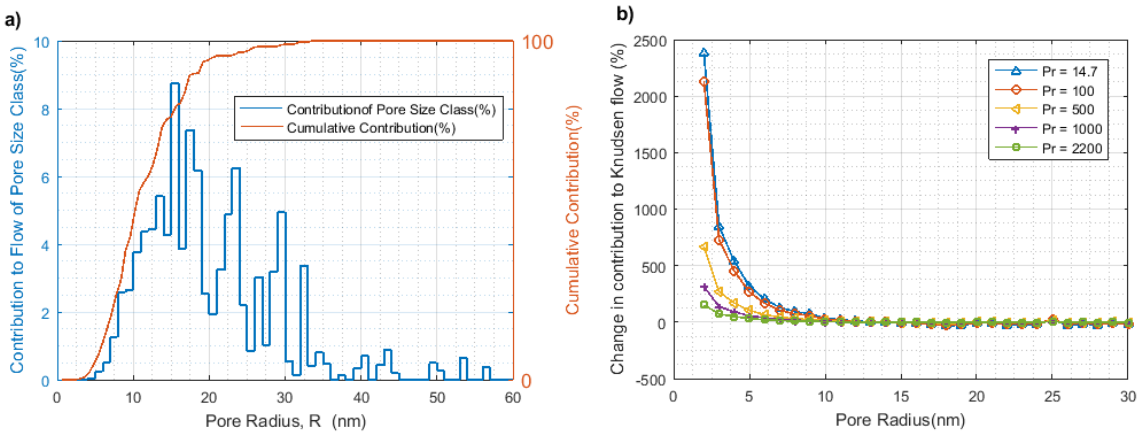

Figure 3.27: Contribution of pore radius ranges to total gas flow rate for Knudsen dry gas: a) the pore size class contribution to Darcy dry gas flow, C_m^D and b) the relative change, ΔC_m of each class of pore size under Knudsen flow for different pressure values.

Table 3.4: Estimated values of ξ_{rel} parameters for data used in this work

Parameter	Value
n	0.927
a	2.371
b	0.193

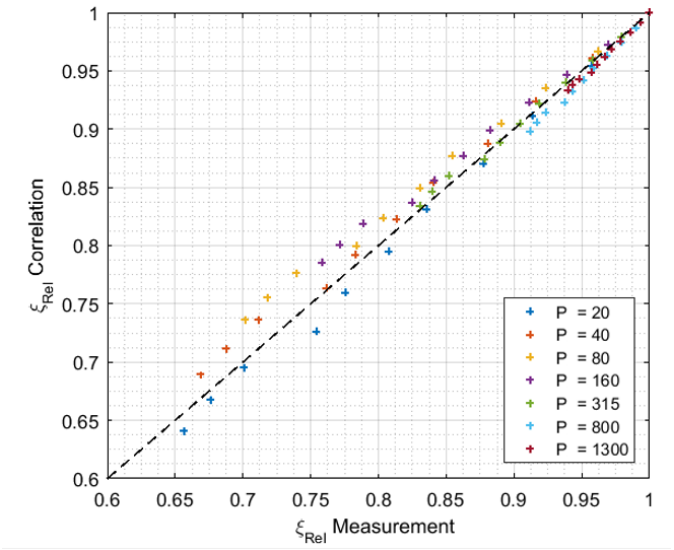

Figure 3.28: Plot of ξ_{rel} values from simulation vs. correlation.

3.7.5 Effect of Pore size Distribution on Relative Correction Factor ξ_{rel}

In order to evaluate the effect of pore size distribution, the previous experiments were performed for varying pore radius median and standard deviation. 8 pore networks with mean pore radius varying from 5 to 30 nm and constant standard deviation 0.6 were generated randomly to evaluate the effect of the median value. Figure 3.29 shows the results of ξ_{rel}. In this figure, the effect of condensate blockage decreases with increasing mean pore radius. At higher median, lower blocked pore sizes have very low contribution to total Knudsen flow. As the median decreases, the pore size distribution shifts to upper levels which reduces the effect of Knudsen flow in the lower part of radii of the distribution.

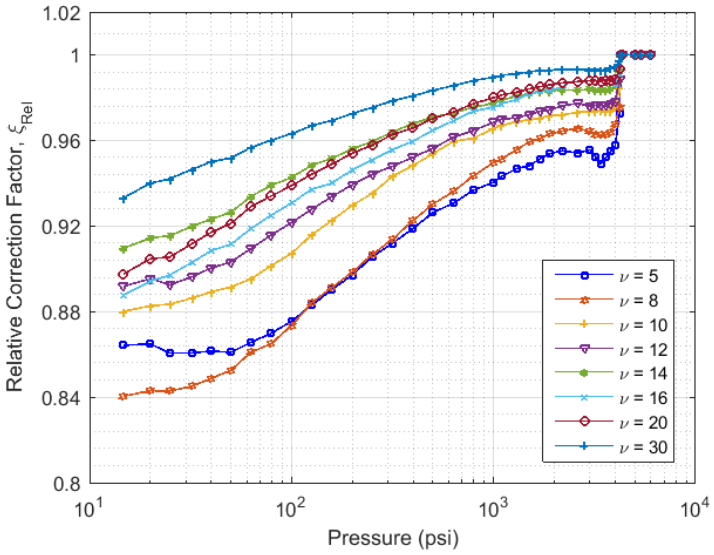

Figure 3.29: Sensitivity of Relative Correction Factor ξ_{rel} to median of pore size distribution.

Other pore networks with standard deviation varying from 0.1 to 0.8 and constant median pore radius of 10nm were generated randomly to evaluate the effect of the standard deviation. Figure 3.30 shows the ξ_{rel} results.

The standard deviation reflects the degree of the dispersion of pore radii. At small standard deviation, pore radii are concentrated around the median value which leads to an insignificant variation of pore radius range filled by condensate and thus a lower effect on ξ_{rel}. Inversely, at high standard deviation values, the pore size distribution is more dispersed leading to condensate saturation change having an effect on the pore radius range available to free gas flow. Thus, it generates a reduction in ξ_{rel}.

These results illustrate the importance of describing the shale matrix as pore size distribution rather than single pore radius to be able to estimate the impact of condensate accumulation on apparent gas permeability.

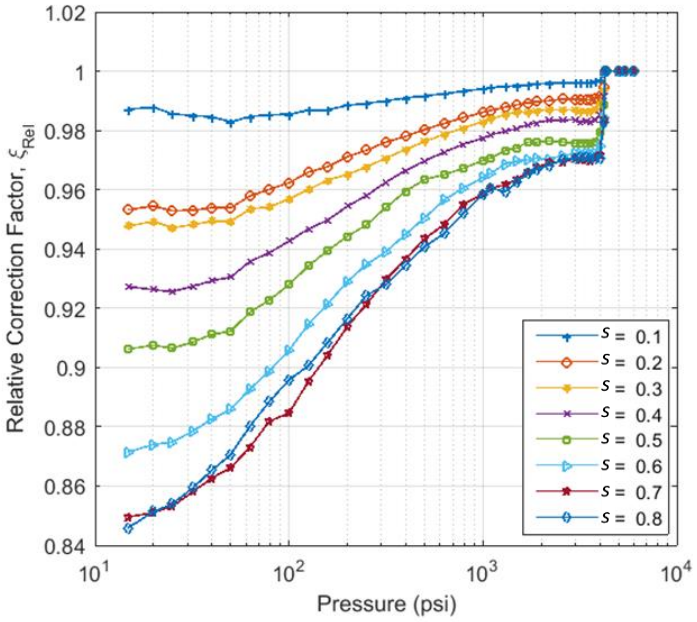

Figure 3.30: Sensitivity of Relative Correction Factor ξ_{rel} to standard deviation of pore size distribution.

3.8 Summary

At nanoscale pores in shale matrix, gas flow deviates from continuum flow to slip flow and transition flow where Darcy law is replaced by Knudsen enhanced permeability model of Beskok, Karniadakis (1999). This deviation from Darcy flow is highly dependent on pore size and pore pressure.

A more accurate modelling is needed for gas condensate two-phase flow in shale matrix at pore level which takes into consideration pore distribution in pore network and the effect of condensate accumulation on Knudsen flow. Single pore size cannot be used to describe Knudsen flow in shale matrix when condensate forms due to the change of the pore size range available for gas flow as function of condensate saturation.

The multi-scale flow model proposed by Beskok and Karniadakis (1999) is used to evaluate Knudsen flow in shale pore level. 3D pore network modelling was used to evaluate gas flow in shale matrix under condensate banking effect using a log-normal pore size distribution.

For dry gas systems, the simplification of the pore network to a single pore size using the effective pore radius proposed by Michel et al. (2011) $R_{eff} = v \exp(3s^2)$. However, for gas condensate systems, the evaluation of Knudsen flow using pore network models is essential in order to implement:

a) the changing flow contribution of pore sizes as a function of pressure: at reservoir pressure under 1000 psi lower pore sizes contribute to total gas flow more than at pressure above 1000 psi.
b) the condensate banking effect by eliminating the contribution of lower pore sizes blocked by condensate and its effect on the gas flow in connected higher pore sizes.

All the condensate generated in shale matrix remained trapped due to high capillary pressure. Consequently, only gas can flow in shale matrix below the dew point pressure.

A new parameters was introduced in this study, "Relative Correction Factor" ξ_{rel} defined as the ratio of ξ_{GC} to ξ_{DG}. It is a measure of the effect of condensate blockage on Knudsen flow and it can be used to adjust correction factor from dry gas flow to gas condensate flow.

Results show that condensate blockage affects the enhancement permeability factor by blocking small pores under capillary pressure effect. A significant reduction of Knudsen flow effect is observed at high condensate saturation and low reservoir pressure.

The effect of condensate blockage is highly dependent on the pore size distribution. High values of standard deviation have relatively high condensate blockage effect on Knudsen flow due to the dispersion of pore size distribution.

Assuming a constant mean effective pore size with pressure in gas apparent permeability calculation in shale matrix with condensate banking results in an overestimation of Knudsen flow contribution in well productivity.

Introducing pore network modelling and dynamic minimum gas pore radius $R_{g,min}$ as function of pressure is crucial in order to estimate accurately the gas apparent permeability under condensate blockage in shale matrix.

CHAPTER 4: GAS-CONDENSATE PHASE BEHAVIOUR DEVIATION IN SHALE MATRIX

4.1 Introduction

Understanding phase behaviour of gas-condensate systems is crucial considering that condensate saturation controls the gas relative permeability hence the well productivity and the fraction of heavy components recovery at surface. As discussed in Chapter 3, gas relative permeability is highly sensitive to condensate saturation under permeability jail effect. Hence, even small variation of condensate saturation has an important impact on well dynamic calculations.

Under high capillary pressure in shale matrix nanopores, the pressure difference between gas and condensate cannot be negligible in VLE (Vapour Liquid Equilibrium) calculation. Furthermore, as the capillary forces are highly dependent on pore size, describing shale porous medium with a pore size distribution is essential to evaluate accurately the phase behaviour deviation. Individual pores with different radii exhibit different phase behaviour and contribute to the macro phase behaviour according to their volumes. However, VLE calculation for shale reservoirs have been studied using the average pore size by many researchers (Brusilovsky 1992, Espósito, Tavares and Castier 2005, Firincioglu, Ozkan and Ozgen 2012, Pang, et al. 2013, Nojabaei, Johns and Chu 2013, Jin and Firoozabadi 2015).

The research question that this Chapter addresses is the effect of pore size distribution on the phase behaviour deviation of gas-condensate fluids in shale matrix. The VLE (Vapour-Liquid Equilibrium) calculation is modelled using PREOS combined with a log normal pores size distribution in order to build a model capable of generating phase behaviour of gas-condensate in shale matrix. The deviation of condensate saturation from bulk phase behaviour to capillary phase behaviour is investigated for lean and rich condensate fluids. The effect of capillary pressure coupled with pore size distribution on condensate saturation vs pressure is also presented.

4.2 Capillary Pressure Effect on Phase Behaviour

In conventional reservoirs, the effect of capillary pressure on the phase behaviour is negligible due to the low vapour-liquid pressure difference. The liquid pressure in one

capillary tube is defined by Young–Laplace equation in Equation (3.13). In shale reservoirs, the capillary pressure, P_c is significant due to the very small pore radii, R which cannot be neglected in VLE calculations.

Sigmund et al. (1973) investigated the effect of porous media on phase behaviour and concluded that only at high surface curvature the effect was significant. Recently, Chen et al. (2012) illustrated in a simple experimental study the capillary condensation in shale plugs compared to sandstone plugs showing the effect of capillary pressure on gas phase behaviour.

Brusilovsky (1992) proposed a modified cubic Equation of State (EOS) that is able to calculate the VLE for multicomponent fluids at given defined surface curvature. They concluded that dew point at high capillary pressure increases compared with the conventional PVT cell dew point. Firincioglu, Ozkan and Ozgen (2012) in their modified Peng-Robinson EOS added surface forces to capillary forces and conducted flash calculation. They showed that surface forces are only significant compared to capillary forces for pore diameter less than 1 nm.

To the best of the author's knowledge, all work done to date only studied the effect of capillary pressure for one equivalent pore radius without taking into consideration the pore size distribution effect on the phase behaviour deviation. Pores sizes with different diameters exhibit different phase behaviour and contribute to the macro-scale phase behaviour proportional to their volumes. In addition, the interaction between the pores should be considered as the liquid formed in bigger pore sizes is adsorbed to smaller pore sizes under capillary pressure effect. The use of one pore size (mean pore size for instance) could lead to an underestimation of the capillary effect in shale matrix.

4.3 Methodology of VLE Calculation

4.3.1 Criteria for Equilibrium

The chemical equilibrium of multicomponent systems is expressed by the equality of fugacity of each component in vapour and liquid phases. For gas condensate system under capillary effect, this condition is expressed as

$$f_{ic} = f_{ig} \quad \mathrm{i} = 1..n_c \tag{4.1}$$

Where f_{ic} and f_{ig} are fugacities of component i in condensate and gas respectively. By replacing the fugacity by its definition, equation (4.1) is rewritten as

$$x_i \phi_{ic} P_c = y_i \phi_{ig} P_g \quad \text{i} = 1..n_c \tag{4.2}$$

Where ϕ_{ic} and ϕ_{iv} are fugacity coefficients for condensate and gas respectively calculated by EOS (Equation of State).

The equilibrium ratio is extended from conventional equation to include P_g and P_c

$$K_i = \frac{y_i}{x_i} = \frac{\phi_{ic} P_c}{\phi_{ig} P_g} \quad \text{i} = 1..n_c \tag{4.3}$$

In contrast, $K_i = \frac{\phi_{ic}}{\phi_{ig}}$ usually used in conventional calculation.

4.3.2 Equation of State

Equation of state (EOS) is a thermodynamic equation which describes fluid phases (gas, liquid and solid) properties: pressure, temperature, volumes and internal interaction. The equation of state was pioneered by Van der Waals in 1873 by predicting the coexistence of vapour-liquid (see Table 4.1).

Redlich and Kwong (1949) developed a modified Van der Waals' EOS to improve its accuracy by proposing a temperature dependency for the attractive parameter a. Later, Soave (1972) and Peng-Robinson (1976) modified Redlich-Kwong EOS and proposed a more general formulation for the attractive parameter in order to improve EOS prediction of vapour pressure and equilibrium ratio. Since then numerous modifications of EOS have been proposed on empirical and theoretical basis (e.g. Martin (1979), Schmidt and Wenzel (1980) and Patel and Teja (1982)). Peng-Robinson is considered the most successful equation of states and it is routinely used in hydrocarbon PVT calculations (Danesh 1998). Table 4.1 provides examples of various versions of equations of state.

Table 4.1: Cubic Equations of State (*P* is pressure, *T* is temperature, *R* is ideal gas constant, *V* is molar volume, *a* is a measure of the attractive forces between the molecules and *b* is related to the size of the molecules).

Reference	EoS
Van der Waals	$P = \frac{RT}{V-b} - \frac{a}{V^2}$
Redlich-Kwong	$P = \frac{RT}{V-b} - \frac{a}{V(V+b)T^{0.5}}$
Soave-Redlich-Kwong	$P = \frac{RT}{V-b} - \frac{a(T)}{V(V+b)}$
Peng-Robinson	$P = \frac{RT}{V-b} - \frac{a(T)}{V(V+b)(V-b)}$

Originally, EOS was developed for pure component systems (i.e. fluids of single molecular) but then extended to multi-components by using mixing rules to determine the interaction forces in the mixture. Simple random mixture rules are well accepted for hydrocarbon fluids modelling where components are assumed randomly dispersed in the mixture (Danesh 1998).

In this work Peng-Robinson equation of state with random mixing rules was used to relate pressure, temperature, volume and composition for both gas and condensate phases, necessary for fugacity coefficient calculation.

4.3.3 IFT Correlation

The interfacial tension (IFT) for a gas-condensate fluid with n_c components is calculated using Parachor method developed by Reno and Katz (1943) as follows:

$$IFT = \left[\sum_{i=1}^{n_c} P_i(x_i\rho_c - y_i\rho_g)\right]^{\mathrm{n}} \tag{4.4}$$

where P_i is the Parachor of component i, x_i and $y_i$are the mole fractions of component i in the liquid and gas phase and n is the correlation exponent. ρ_c and ρ_g are condensate and gas molar densities, respectively, calculated from equation (4.5).

$$\rho_{c,g} = \frac{P_{c,g}}{Z_{c,g}R_g\,T} \tag{4.5}$$

where $P_{c,g}$ is condensate or gas phase pressure (MPa), $Z_{c,g}$ is condensate or gas phase Z-factor,

R_g is the gas constant and T is the reservoir temperature (K). Equation (4.4) is called the Parachor method and it is commonly used in hydrocarbon PVT calculation. Reno and Katz (1943) proposed a value 4 for the exponent *n*. The Parachor is a constant of pure components and it's a measure of the molecular volume and chemical composition (Schechter and Guo 1998). Reno and Katz's (1943) correlation Hough and Stegemeier (1961) and Chien (1984) proposed exponent values of 3.67 and 3.91, respectively instead of 4. Firoozabadi and Katz (1988) compared calculated IFT using different exponents with experimental data and concluded that a quadratic exponent provides the best IFT estimation. The effect of the exponent variation according to different correlations has a marginal effect on final results.

4.4 Phase Behaviour Modelling in Single Pore

Constant Volume Depletion (CVD) is a routine PVT experiment carried out in laboratory and its results are used to analyse production from gas-condensate reservoirs under natural depletion. Initially, a streamline gas sample is collected in a cell at pressure above dew point. The cell volume is expanded until reaching the dew point and the reference volume is recorded. The volume is then increased regularly to reach pressure values with constant incremental change of 50 to 150 psi. At each pressure step, the excess of gas above the reference volume is removed and condensate and gas saturation are recorded. Figure 4.1 illustrates the schematic of CVD experiment for gas-condensate fluid with 3000 psi dew point and 150 psi pressure step.

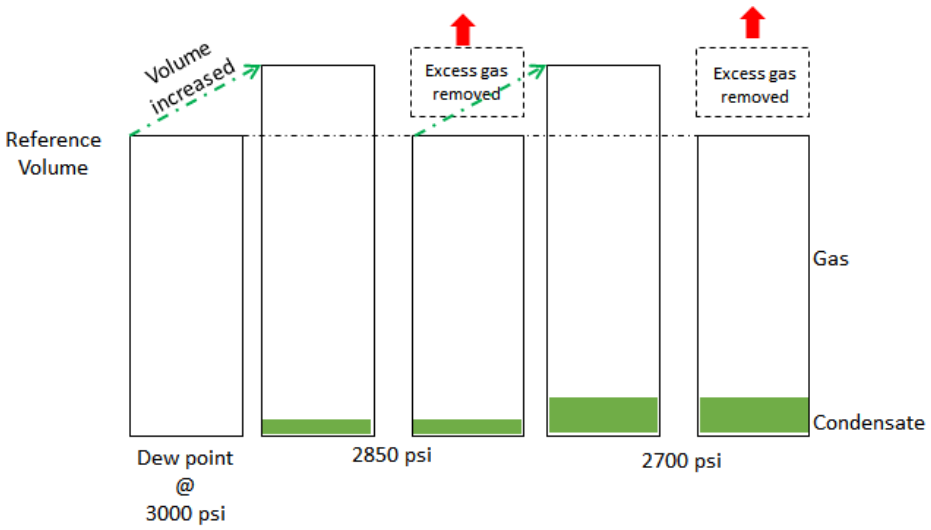

Figure 4.1: Schematic of CVD experiment with dew point at 3000 psi and pressure step of 150 psi

Obviously, CVD experiments are carried in laboratory (bulk condition) at null capillary pressure which cannot be representative of phase behaviour in shale matrix under capillary pressure effect. As mentioned in Chapter 3, CVD experiment reflects the gas-condensate flow in shale matrix better than CCE (Constant Composition Depletion) where condensate remains almost immobile and only free gas flows.

4.4.1 Dew Point Estimation

In order to be able to combine IFT with equation of state, an algorithm was developed in Matlab which includes two convergence criteria for both fugacity and IFT The Matlab code of this algorithm is provided in an attached CD-ROM. Initially, the bulk dew point P_d^{bulk} is

estimated using bulk calculation without capillary pressure ($P_l = P_g$). For dew point calculation under capillary pressure effect, the algorithm starts with the bulk dew point P_d^{bulk} as an initial guess then the IFT at this pressure is calculated using the bulk gas and condensate compositions as initial values. The use of the bulk dew point P_d^{bulk} as an initial guess is justified in order accelerate the algorithm rather than selecting a random initial guess. An EOS calculation is carried out resulting to fugacity values for both gas and condensate and their equilibrium is verified against a tolerance value ε_f using Condition (4.6)

$$\sum_{i=1}^{nc}\left(1-\frac{f_{ig}}{f_{ic}}\right)^2 \leq \varepsilon_f \tag{4.6}$$

This process is repeated until the equilibrium condition (4.6) is satisfied. If it is not the case, a new dew point is calculated as

$$P_{d,new} = P_{d,old}\sum_{i=1}^{nc}\frac{yi}{Ki} \tag{4.7}$$

where yi is gas molar fraction and Ki the equilibrium ratio of component *i.*

When condition (4.6) is satisfied a new σ_{new} is calculated using equations (4.4) and (4.5). The new σ_{new} is checked against the previous σ_{old} (which was to calculate the input capillary pressure) to evaluate the IFT convergence by a tolerance factor ε_σ

$$|\sigma_{new} - \sigma_{old}| \leq \varepsilon_\sigma \tag{4.8}$$

Figure 4.2 illustrates the flow diagram for the described dew point pressure calculation.

Table 4.2 lists the fluid composition, temperature and wettability used in the dew point calculation. Figure 4.3 gives the dew point calculation results for five pore radii of 3, 5, 10, 50 and 100 nm. In Figure 4.3a, the dew point lines for each pore radius is plotted with the bulk dew point line and it shows that the dew point in nanopores is higher than bulk dew point. Figure 4.3b gives the deviation of dew point from the bulk conditions. The deviation is inversely proportional to pore radius; e.g. 3nm pore has a positive deviation up to 300 psi while 100nm pore has a deviation less than 20 psi. Moreover, the dew point deviation at the same pore radius decreases significantly towards the critical point where vapour and liquid share similar properties resulting in a null IFT (see Figure 4.3c).

Table 4.2: Fluid and tube properties used in calculation.

Retrograde Condensate	
Component	*Molar Composition (%)*
C1	78
C4	12
C7	7.2
C10	1.4
C14	1.4
Reservoir Temperature, T_{res} (K)	430
Wettability, $cos\theta$	0.80

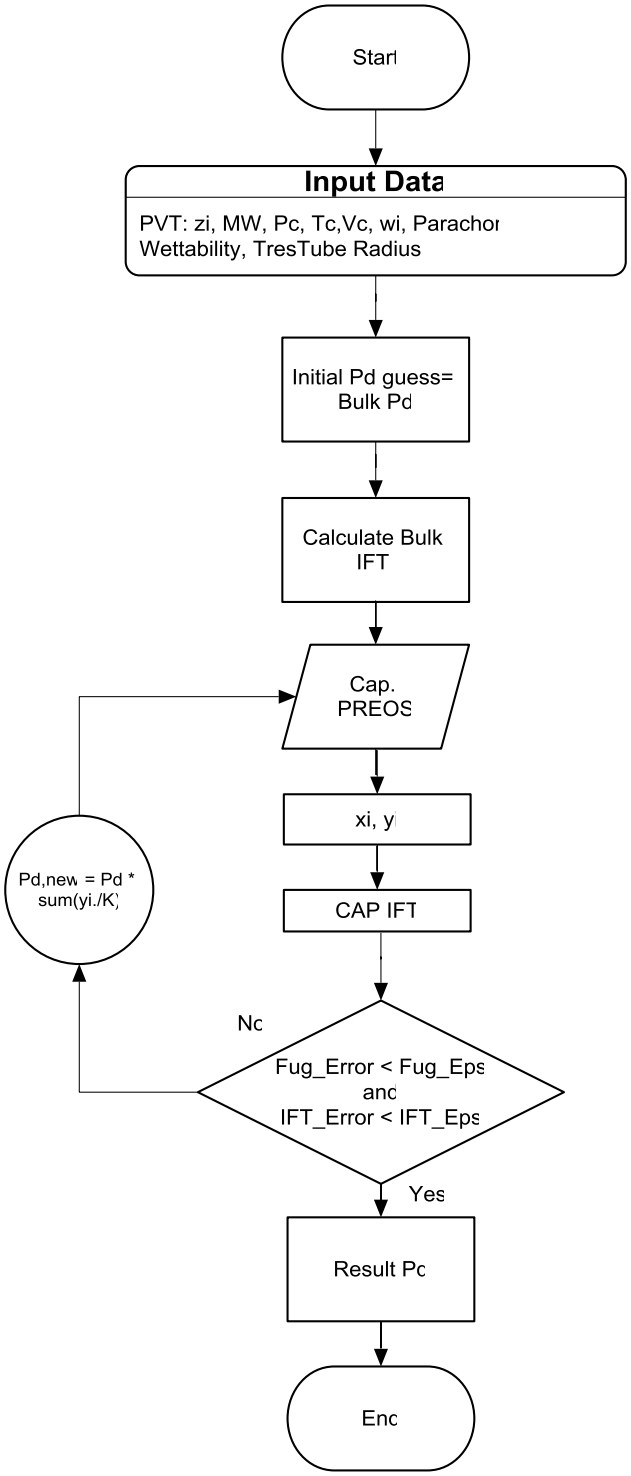

Figure 4.2: Flow diagram for single tube CVD simulation

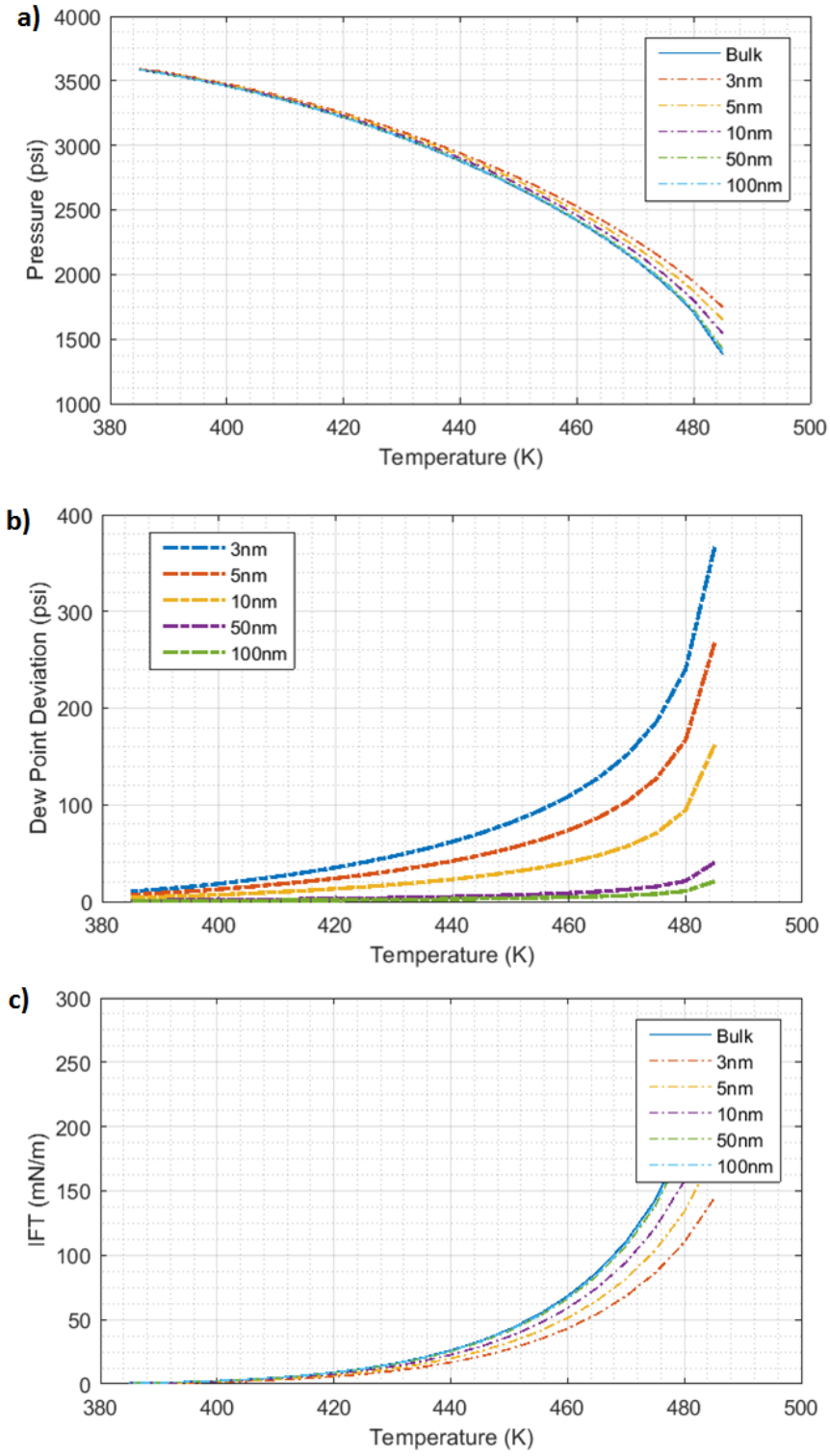

Figure 4.3: Dew point deviation in single tubes of 3, 5 and 10 nm: a) capillary dew point vs. bulk dew point, b) dew point deviation as function of temperature and c) IFT as function of temperature.

4.4.2 CVD Condensate Saturation

After capillary dew point calculation, a second algorithm is needed to calculate the gas-condensate equilibrium in the two-phase regions under the dew point and then to estimate the condensate saturation and other properties such as Z-factor, density and IFT. At each pressure step, the total system molar composition is known as z_i but the molar composition of gas and condensate phases are unknown which are controlled by fugacity equation and capillary pressure.

Very similar to the dew point algorithm, condensate saturation is calculated using two layers, one for fugacity and another for IFT. The only difference resides at the end of fugacity loop where a new equilibrium ratio $K_{i,new}$ for each component is calculated as

$$K_{i,new} = K_{i,old} \frac{f_{ic}}{f_{ig}} \tag{4.9}$$

The dew point is used as a volume reference, i.e. the algorithm simulates decrease of pressure from dew point to next lower pressure step by cell volume expansion and the excessive gas volume above the initial volume at the dew point pressure is evacuated. Therefore, the total molar composition is updated by removing the evacuated gas moles from the cell. The CVD experiment describes more accurately (than CCE) the multiphase flow in shale matrix where only gas can flow while condensate remains almost immobile. Figure 4.4 illustrates the flow diagram for the CVD calculations.

Figure 4.5 represents the result of condensate relative volume of capillary CVD numerical simulation for 3, 5, 10, 20 and 50 nm radii plotted against bulk CVD. It shows that the lower the tube radius the higher the phase behaviour deviation with maximum condensate relative volume deviation of 17% for 3nm radius tube.

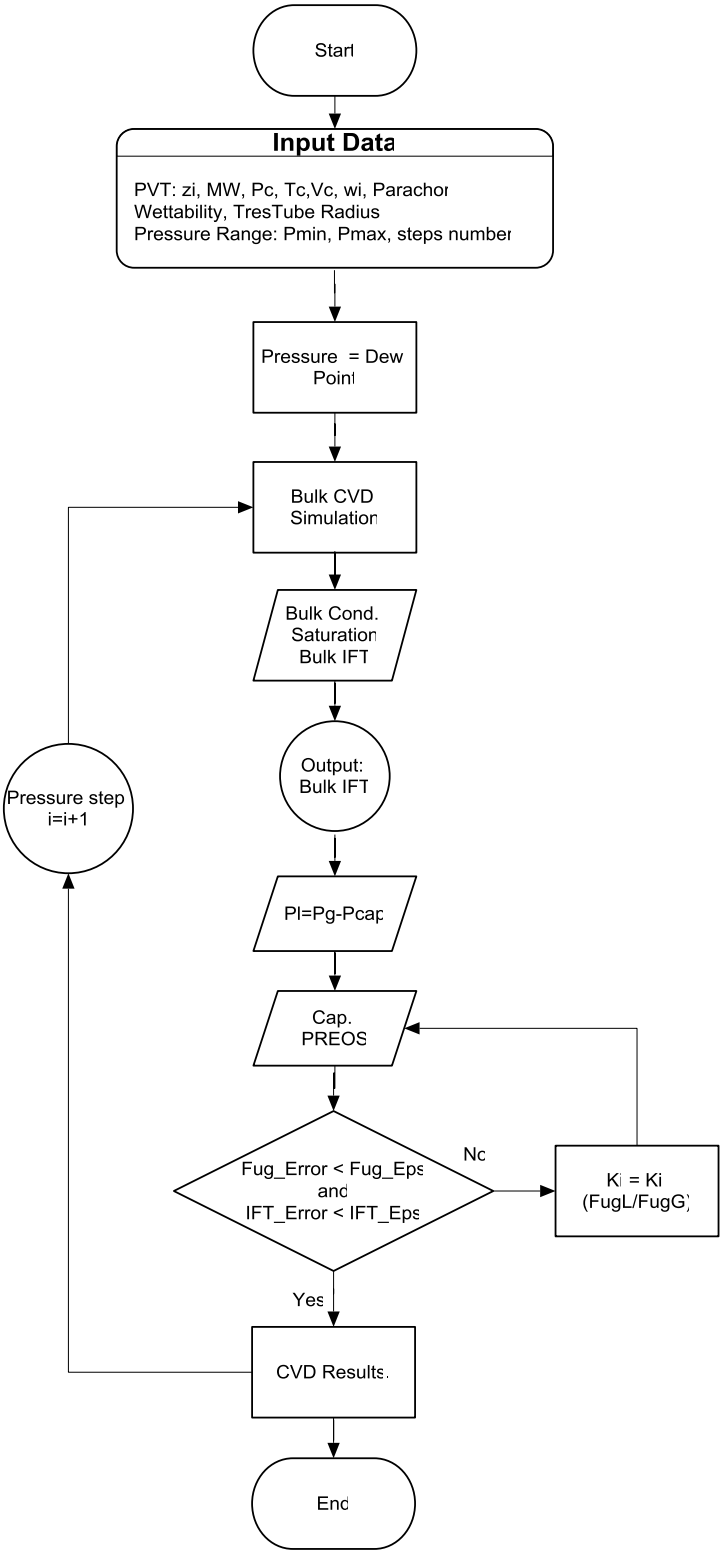

Figure 4.4: Flow diagram for single tube CVD simulation

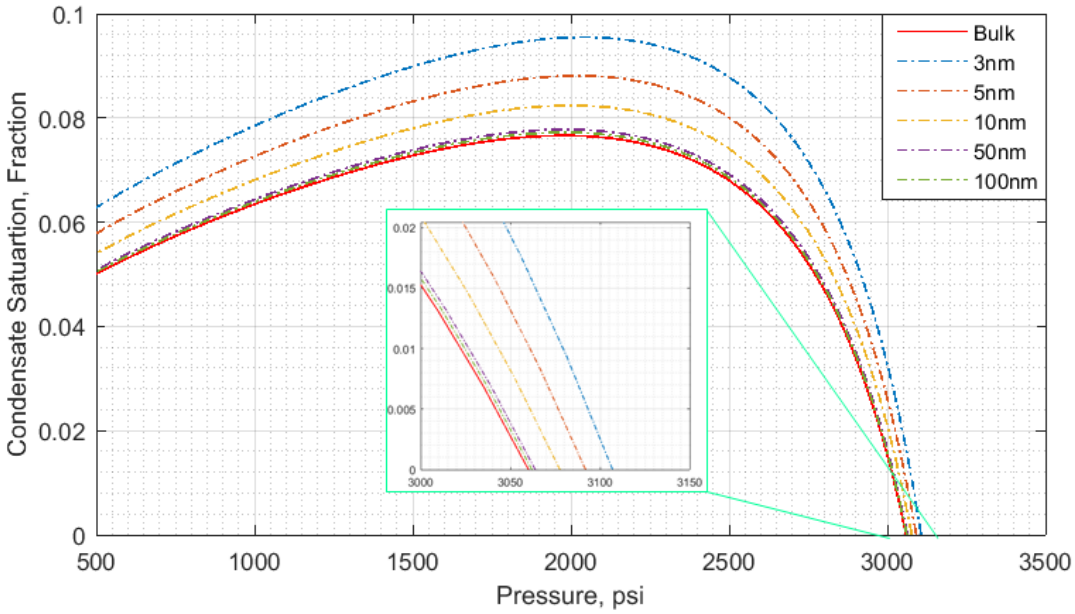

Figure 4.5: CVD condensate relative volume for single tube with different radii: 3, 5, 10, 20, 30 nm plotted against bulk CVD.

4.5 Phase Behaviour Modelling in Pore Network

4.5.1 CVD Numerical Simulation

In shale matrix which is described usually by pore size distribution, assuming one pore size to carry out phase behaviour calculation will be misleading because of the difference of phase behaviour of each pore size and the volumetric contribution of each pore size range. Figure 4.6 illustrates an example of incremental pore space by pore radius range for a pore size distribution of log-normal (10nm, 0.6) with R_{min} =3nm and R_{max} =200nm plotted with the PDF. Although the pore deviation increases by decreasing pore radius, the contribution of small pore radius range is insignificant compared to higher pore range where the phase behaviour deviation is less significant. Consequently, the phase behaviour calculation under capillary pressure effect must be carried out for the pore distribution range rather than pore radius average or median.

In this work, two models are presented to evaluate the deviation of phase behaviour from bulk to under capillary pressure effect for gas condensate fluids in shale matrix: Discretised Pore Space Model (DPSM) and Continuous Pore Space Model (CPSM).

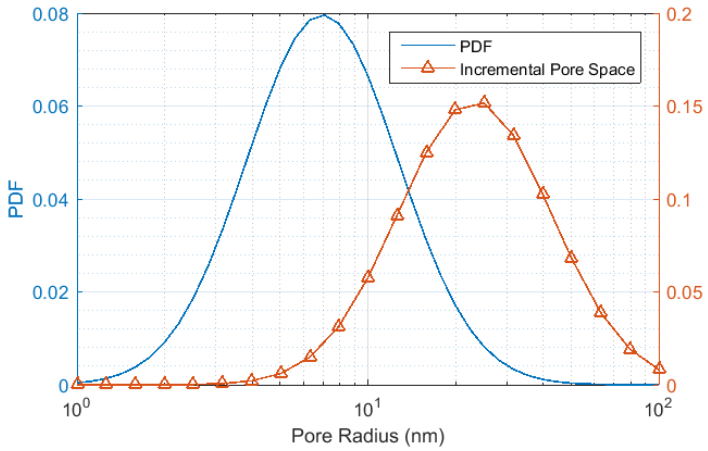

Figure 4.6: PDF vs. incremental pore space of log-normal(10, 0.6)

4.5.2 Discretised Pore Space Model (DPSM)

The pore space is discretised from continuous log-normal distribution to N tubes and the condensate is assumed to start to build up simultaneously in each tube separately without interconnection. In order to upscale the condensate relative volume (and other fluid properties) from pore scale to macro scale, the individual tube pore volume is used as weight for condensate relative volume averaging as shown in Equation (4.10)

$$V_{rel} = \sum_{i=1}^{N} V_{rel}^{i} \, V_{pore}^{i} \tag{4.10}$$

where V_{rel} is macro-scale (pore media) condensate relative volume, V_{rel}^{i} is the tube i condensate relative volume and V_{pore}^{i} is the tube i pore space.

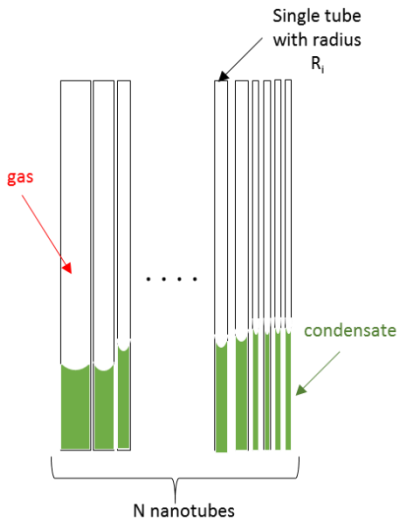

Figure 4.7: Schematic diagram of Discretised Pore Space Model representing porous media s bundle of N tubes.

4.5.3 Connected Pore Space Model (CPSM)

In the continuous pore space model, the interaction between tubes is considered. The condensate starts to generate in the smallest pore size under the effect of high capillary pressure (see Figure 4.7). As the condensate saturation increases with decreasing pressure below dew point, the condensate fills next pore size range.

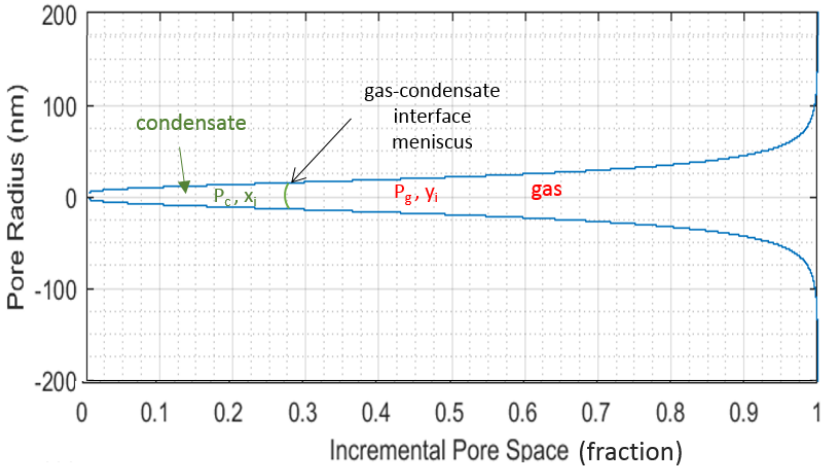

Figure 4.8: Schematic diagram of Connected Pore Space Model representing porous media as connected nanotubes. Y-axis represents pore radius and X-axis represents the incremental pore space fraction of pore radius.

Figure 4.9 and Figure 4.10 show the flow diagram of DPSM and CPSM methods respectively.

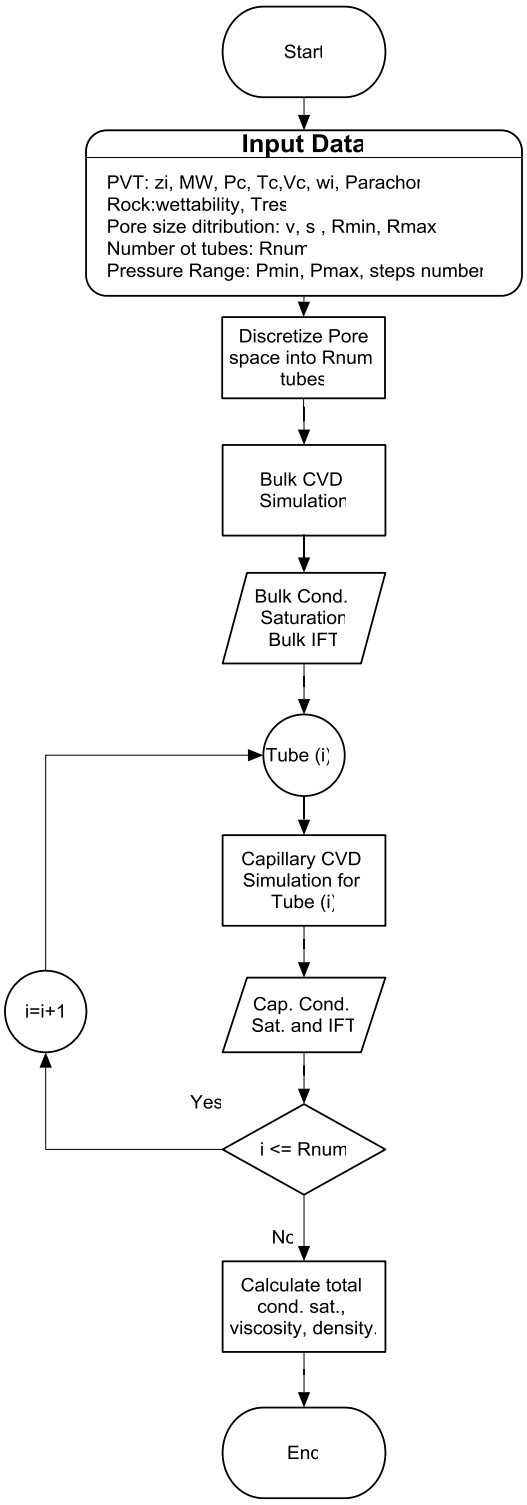

Figure 4.9: Flow diagram of CVD experiment simulation using DPSM.

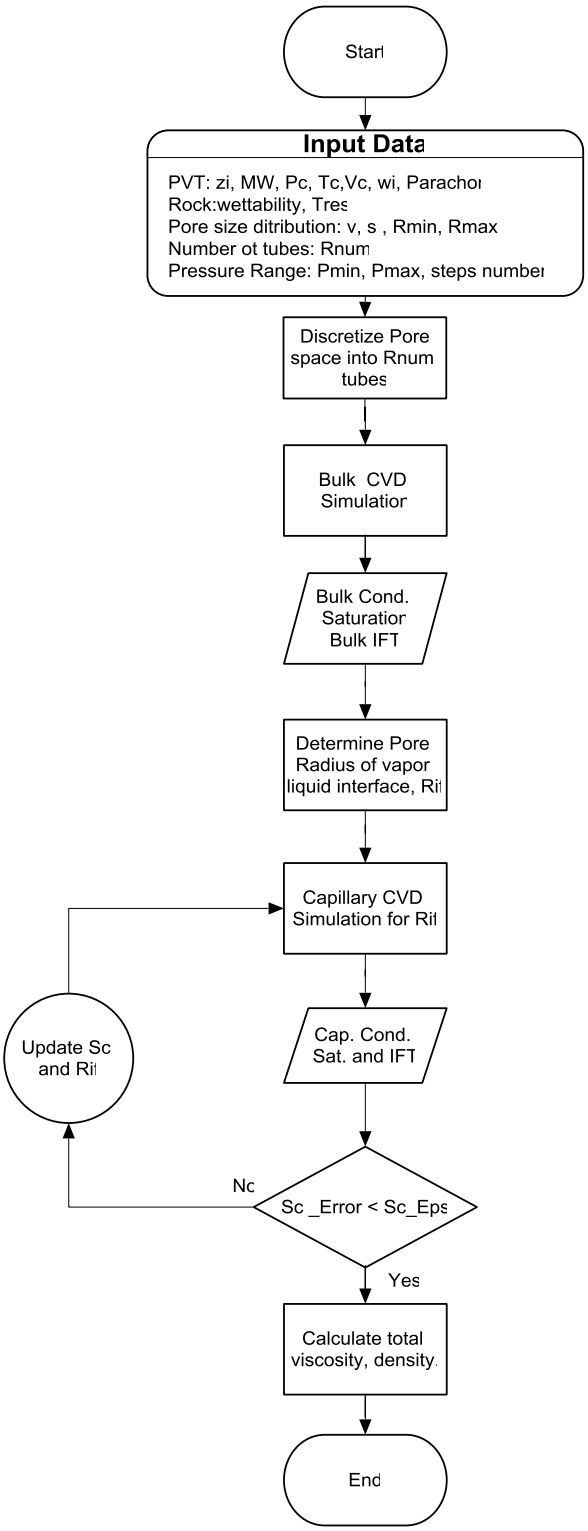

Figure 4.10: Flow diagram of CVD experiment simulation using CPSM.

4.5.4 CVD Numerical Simulation in Pore Network

A number of CVD numerical simulation was carried out for lean and rich gas condensate fluids and a pore distribution of $\ln \mathcal{N}(10, 0.6)$ with minimum pore radius of 1nm and maximum pore radius of 300nm. Table 4.3 summarises the input data for the numerical simulation. All the codes necessary to perform the PVT calculations were written in Matlab. These codes are provided in attached CD-ROM.

Table 4.3: Fluids and pore size distribution properties used in CVD numerical simulation

Lean Retrograde Condensate		**Pore Size Distribution**	
Component	*Molar Composition (%)*	Median, ν (nm)	10
C1	80	Standard Deviation, s	0.6
C4	12	Minimum Pore Radius, R_{min} (nm)	3
C7	7.2	Maximum Pore Radius, R_{max} (nm)	200
C10	0.4	Reservoir Temperature, T_{res} (K)	392
C14	0.4	Wettability, $cos\theta$	0.8

Rich Retrograde Condensate	
Component	*Molar Composition (%)*
C1	70
C2	9
C3	6
C4	6
C5	2
C10	1
C16	6

4.5.5 Bulk vs. Capillary Phase Behaviour

Figure 4.11 represents condensate saturation of CVD simulation carried out for a lean condensate fluid shale matrix with a pore distribution described in Table 4.3. The CVD simulation were completed for bulk condition (no capillary effect), Discretised Pore Space Model (DPSM) and Continuous Pore Space Model (CPSM). Figure 4.11(a) shows the higher condensate saturations resulted from capillary models (DPSM and CPSM) compared to bulk conditions. Higher condensate saturation in the matrix leads to higher condensate banking effect on well performance.

The main disadvantage of this approach is that EOS cannot be applied as pore diameter and pressure combination resulting in negative liquid pressure (see Figure 4.11a). Comparing the two capillary models, CPSM gives higher condensate saturations and higher dew point pressure. Figure 4.11b depicts a condensate saturation deviation up to 60% of CPSM around near to the dew point pressure while for DPSM the deviation is about 25%. Between 2000 psi and 500 psi, CPSM deviation is around 10% and twice the DPSM deviation.

The CPSM reflects the effect of the condensate build up gradually in the small pores where the capillary pressure effect is more pronounced resulting in higher dew point and condensate saturation than DPSM where condensate is assumed to start forming in all pores sizes simultaneously.

In DPSM, although phase behaviour is more important in small pores (less than 20 nm) their contribution to the overall phase behaviour deviation is not significant due to the small volume contribution. In small pores the fluid condenses at higher pressure than bulk dew point and the liquid dropout in the two phase regions is higher. The deviation is more pronounced at the dew point as the fluid condenses at higher pressure and in the two phase region. For this example, the dropout volume deviation can reach up to 10% for 20nm.

Figure 4.12 shows the effect of capillary pressure on the heavy components fraction (C4, C7, C10 and C14) of produced gas. The produced gas is referred to as the gas removed at each CVD numerical simulation step. The capillary model, CPSM, results in lower fraction of heavy component compared to the bulk model. Under capillary pressure with higher condensate saturation, the generated condensate has higher heavy component fraction than in bulk model. Not considering the capillary trapping of the heavy components fraction in the reservoir would lead to an overestimation of the predicted commercial value (*i.e.* calorific value) of the surface produced gas.

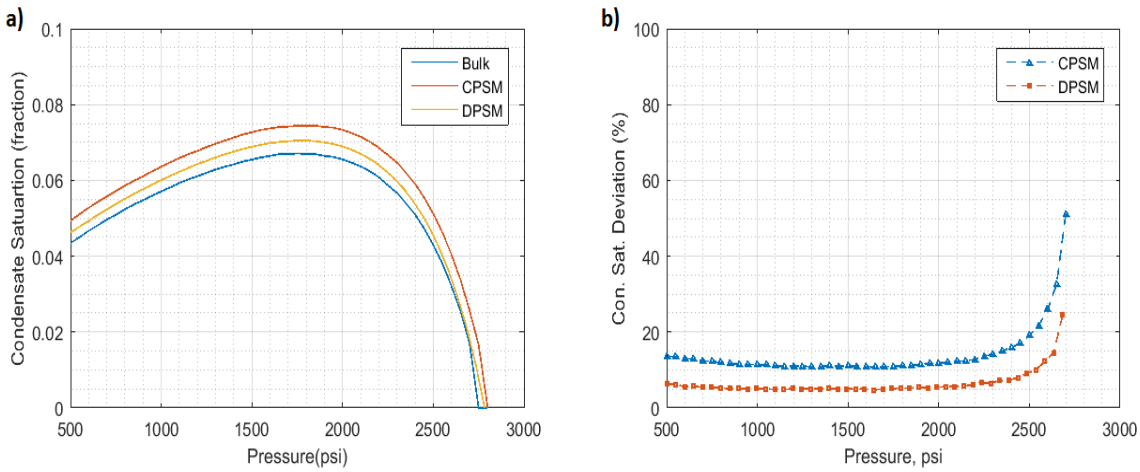

Figure 4.11: Condensate saturation of pore size distribution vs. bulk condensate saturation of CVD experiment simulation

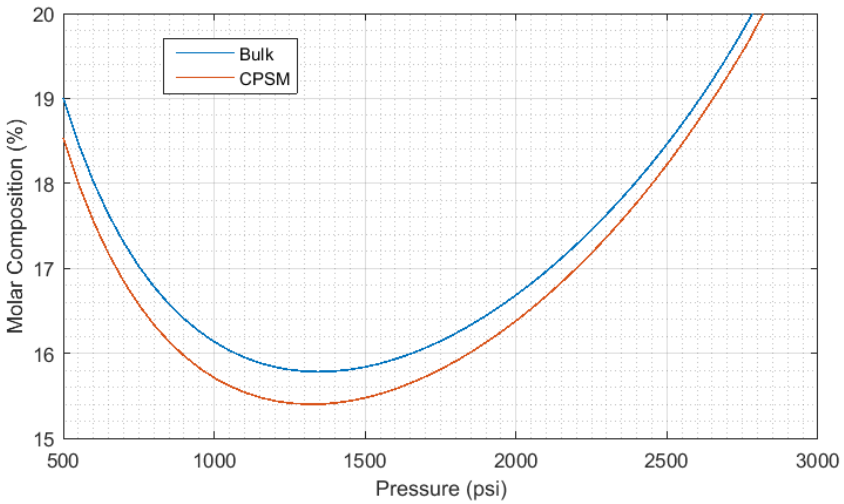

Figure 4.12 Effect of capillary pressure on heavy components fraction of produced gas: CPSM models show a lower fraction of heavy component than bulk model leading to a lower surface commercial value.

4.5.6 Rich vs. Lean Condensate

Figure 4.13 compares the condensate saturation of CVD simulation of lean and rich condensate fluids in the same pore size distribution given in Table 4.3 using CPSM method. The rich condensate fluid exhibits a lower degree of deviation in terms of condensate saturation compared to lean condensate fluid. This deviation difference can be explained by the different pore sizes where the gas-condensate meniscus occurs. Figure 4.14 shows the pore radius of gas-condensate interface meniscus for lean and rich condensates. This Figure indicates that pore radius meniscus is higher in rich condensate than lean condensate.

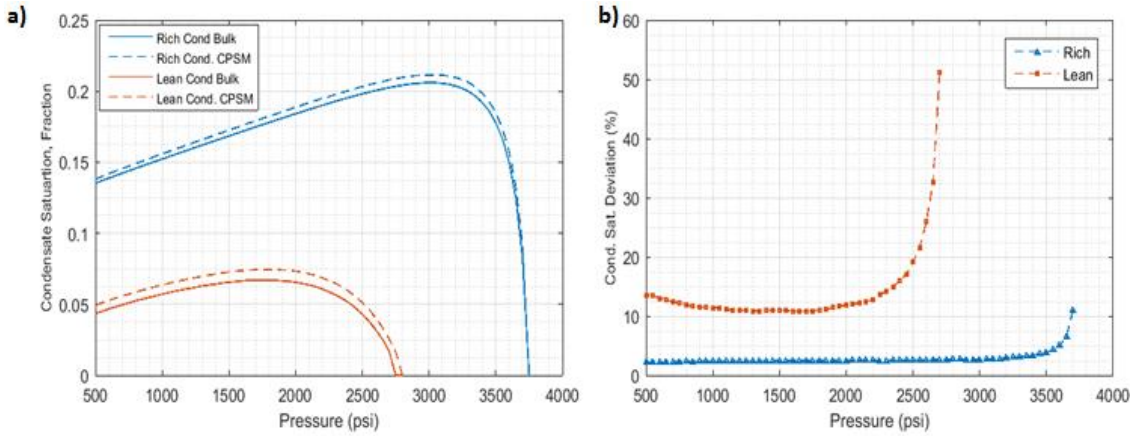

Figure 4.13: Comparison of condensate saturation deviation between lean and rich condensate.

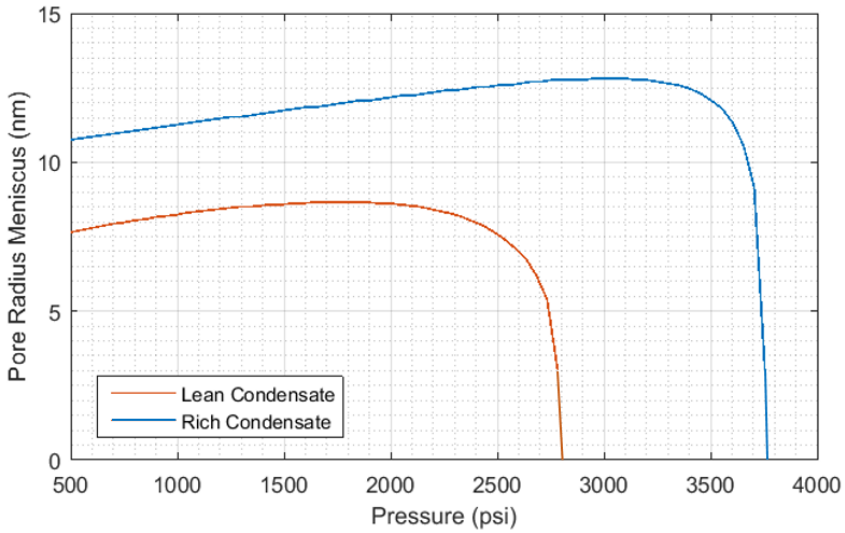

Figure 4.14: Pore radius of gas condensate interface meniscus at equilibrium for lean and rich condensate.

4.5.7 CPSM vs. R_{avg} Method

Many authors (Brusilovsky 1992, Espósito, Tavares and Castier 2005, Firincioglu, Ozkan and Ozgen 2012, Pang, et al. 2013, Nojabaei, Johns and Chu 2013, Jin and Firoozabadi 2015) used single nanotube with an average pore size to study the phase behaviour in shale matrix. However, using average pore size can lead to an underestimation of the phase behaviour deviation. For example, Figure 4.15 shows the CVD condensate saturation results for lean condensate (see Table 4.3) using CPSM method vs. single tube method with

$$R_{avg} = v\, e^{s^2/2} = 11.97\ nm \tag{4.11}$$

The average pore radius method gives a lower condensate saturation compared to CPSM method due to the pore radius of 11.97 nm used in calculation which is greater than the actual pore radius of gas-condensate interface predicted by CPSM.

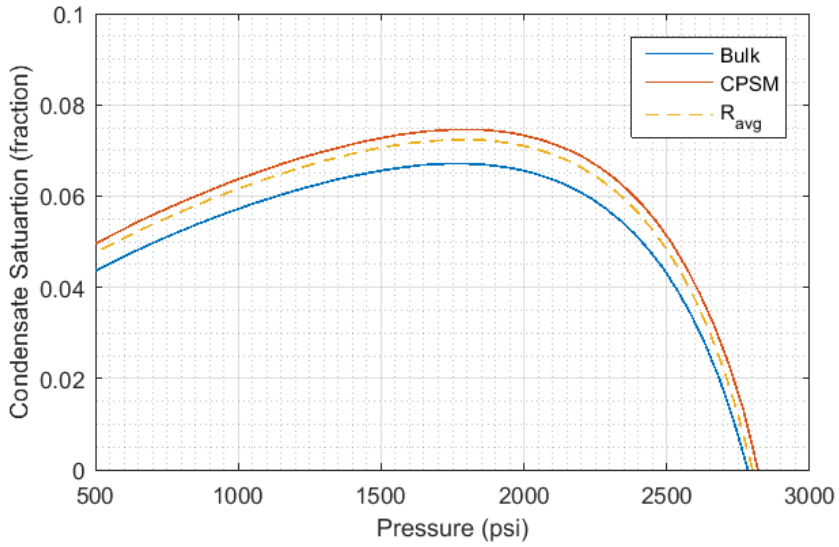

Figure 4.15: Condensate saturation using CPSM vs. single tube with R_{avg}.

4.5.8 Pore Distribution Effect

Furthermore, the pore size distribution effect is investigated by varying the standard deviation s = 0.1, 0.5 and 0.9 for the same pore size distribution and lean condensate data in Table 4.3. Results are presented in Figure 4.16. At low s values, the pore size distribution is concentrated around the mean value v=10nm resulting to high capillary pressure and high phase behaviour deviation. At high s values, the pore size is more scattered towards bigger pore sizes with low capillary pressure and less deviation.

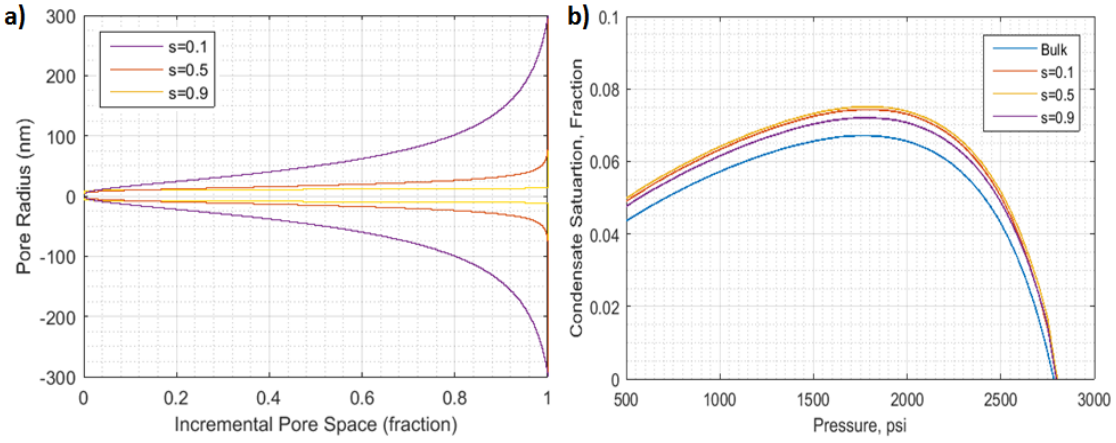

Figure 4.16: Effect of varying standard deviation, s=0.1,0.5 and 0.9 on condensate saturation deviation: a) Incremental pore space fraction vs. pore radius of different distributions and b) condense saturation of different distribution deviation compared to bulk.

4.5.9 Wettability Effect

Rock wettability to condensate can change significantly from one shale play to another and even in the same reservoir. It has a direct effect on capillary pressure as mentioned by Young-Laplace Equation (3.13). Figure 4.17 represents the sensibility of CVD condensate saturation to rock wettability of condensate for 0.4 to 1 values. As expected, condensate saturation under capillary pressure has a high dependency on rock wettability. Hence, wettability measurement and averaging wettability heterogeneity is important for an accurate phase behaviour modelling of gas-condensate fluids in shale matrices.

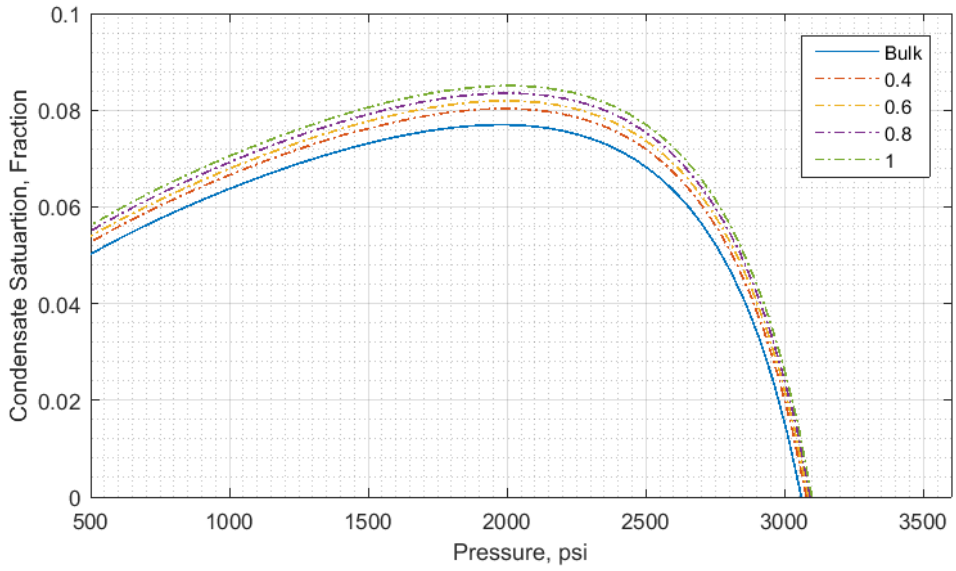

Figure 4.17: CVD condensate saturation sensitivity to wettability

4.6 Summary

Shale reservoir matrix is characterised by very small pore sizes in the range of nanometre resulting in very high capillary pressure. Unlike conventional reservoir, capillary pressure effect on phase behaviour cannot be negligible; i.e. it must be considered in VLE calculation of gas-condensate systems.

The dew point and condensate saturation were investigated in single tubes using Peng-Robinson EOS and compositional IFT model. An iterative algorithm is used to solve the system for dew point calculation and condensate saturation in CVD simulation. Results show the phase behaviour deviation in terms of dew point and CVD condensate saturation is more important in small pore radii. The dew point deviation for all pore radii decreases as temperature and pressure move towards critical point where IFT is null.

As different pore radii exhibit different phase behaviours, the pore size distribution should be used in the VLE calculation of shale reservoir matrix. Two models were proposed in this work to model the upscaling of CVD simulation from single nanotube to shale matrix. The first model, Discretised Pore Space Model (DPSM) represents the matrix porous media as bundle of capillary tubes where the condensate forms simultaneously in all tubes. Second model, Connected Pore Space Model (CPSM) depicts the interaction between tubes under capillary pressure where the condensate starts to build up in small pores and continues to fill the larger pore gradually. Both models use an iterative algorithm to converge towards system solution. Results show that CPSM predicts more accurately dew point and CVD condensate saturation than DPSM thanks to the connected pores method.

Beside the higher condensate saturation that affects the well performance, the capillary pressure effect contributes to the trapping of the heavy components in the matrix resulting in a leaner produced gas at the surface than in conventional reservoirs.

The phase behaviour deviation is more pronounced in lean condensates than rich condensate due to the smaller pore size at which the gas-condensate interface forms resulting in a higher capillary pressure.

Using pore size distribution in phase behaviour calculation under capillary pressure effect for shale gas-condensate reservoirs is crucial in order to evaluate accurately reservoir saturations and compositional change as a function of pressure.

Rock wettability is a key parameter in phase behaviour calculation under capillary pressure effect as it affects the condensate saturation deviation.

CHAPTER 5: PERFORMANCE OF GAS CONDENSATE SHALE RESERVOIRS

5.1 Introduction

As mentioned in Chapters 3 and 4, the very small pore size in shale matrix impacts the gas-condensate multiphase flow where Darcy flow deviates to Knudsen flow and phase behaviour is affected by high capillary pressure. Even though the hydraulic fracturing enhances the conductivity of the reservoir, fluid needs to flow from the matrix to the fracture. Consequently, evaluation of matrix flow performance is crucial for well production calculations.

Furthermore, in shale reservoirs, condensate banking effect occurs mainly in the matrix rather in the fracture network. In hydraulic fractures, gas and condensate phases can flow simultaneously with very low effect on productivity. However, due to the high capillary forces in the matrix, condensate banking causes reduction of the gas relative permeability hence a decrease of productivity.

Consequently, investigating condensate banking effect in shale matrix and how it is influenced by Knudsen flow and phase behaviour deviation can be considered representative of their effect on the well productivity.

In this chapter, the research objective regarding the evaluation of the effects of condensate banking, flow behaviour deviation (Knudsen flow) and phase behaviour deviation under capillary pressure on gas-condensate flow from matrix to fracture is addressed. A one block matrix flow model is derived in Laplace domain which covers both transient and pseudo-steady state flows. Results of Knudsen flow and phase behaviour deviation modelling from Chapters 3 and 4 were used as input data to the model and their effect on production is examined.

5.2 Previous work

The shale matrix reservoirs are described as hydraulically/naturally fractured reservoirs with dual-porosity system: matrix with low permeability and high storativity and fracture network which represents induced hydraulic fracture with or without natural factures. The fluid flows from matrix to fracture network and then to the wellbore.

Dual porosity well models were first introduced by Barenblatt, Zheltov and Kochina (1960) and later extended to well test analysis of slightly compressible fluids by Warren and Root (1963). Kazemi (1969) introduced a new model for matrix-fracture transient flow using slab matrix model and bounded radial reservoir. El-Banbi and Wattenbarger (1998) presented for the first time linear flow in fractured reservoirs using dual porosity for constant pressure and constant rate. Many other models (Brown and Ozkan 2009, Bello and Wattenbarger 2010, Stalgorova and Mattar 2013) were developed by extending El-Banbi and Wattenbarger's model by considering an additional outer unstimulated region (with natural fractures only) in communication with the SRV.

While dual porosity models for single phase high compressible fluids (gas reservoirs) were derived from slightly compressible models using the pseudopressure and pseudotime functions, gas-condensate reservoirs cannot be described by analytical dual porosity models. The main reason is the pseudopressure function difference between fracture and matrix because they have different relative permeability functions. Where liquid and gas relative permeabilities in matrix have a concave shape, in fracture relative permeability is more straight line like due to the difference of interfacial tension in matrix and fracture. This pseudopressure function discontinuity represents the major difficulty in extending dual porosity models from single phase to gas condensate reservoirs.

Numerical simulation is widely used to evaluate well performance of fractured gas-condensate reservoirs both conventional and unconventional. However, flow behaviour and phase behaviour deviation of gas-condensate fluids are not yet introduced into commercial simulators as it is still under research domain. For this research, no open source dual porosity compositional numerical simulator was available to incorporate the necessary models to describe the phenomena. As a result, in this work the effect of flow behaviour and phase behaviour deviation is investigated by using only a single matrix block with constant fracture pressure.

5.3 Mathematical Model

Conventionally, matrix in naturally fractured reservoirs is modelled as cubes, cylinders, slabs, or matchsticks. In shale reservoirs, the hydraulic fractures are usually intuited in vertical direction creating vertical matrix geometries that can be idealised as match sticks (see Figure 5.1). As discussed in Chapter 3, the condensate flow in shale matrix is assumed to be negligible.

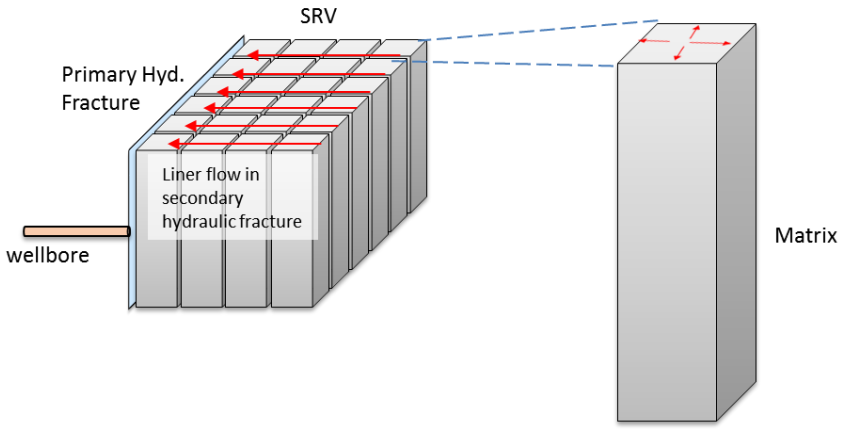

Figure 5.1: Modelling matrix as matchstick

Diffusivity equation for radial flow in matrix writes in field units

$$\frac{0.006328}{r}\frac{\partial}{\partial r}\left(\frac{\xi k_{rg} k_{\infty}}{\mu}(\rho\, r)\frac{\partial p}{\partial r}\right) = \rho\phi c_f \frac{\partial p}{\partial t} + \phi \frac{\partial \rho}{\partial t} \tag{5.1}$$

where r is radial coordinate, ξ is the Knudsen enhancement factor, k_{rg} is gas relative permeability, k_{∞} is intrinsic rock permeability, μ is gas viscosity, ρ is gas density, p is pressure, ϕ is rock porosity, c_f is formation compressibility and t is time.

Replacing $\rho = \frac{pM}{ZRT}$ and $c_g = \frac{1}{p} - \frac{1}{Z}\frac{\partial Z}{\partial p}$ in Equation (5.1) gives

$$\frac{0.006328}{r}\frac{\partial}{\partial r}\left(k_{\infty}\frac{\xi p}{\mu Z}\frac{\partial p}{\partial r}\right) = \phi c_t \frac{p}{Z}\frac{\partial p}{\partial t} \tag{5.2}$$

Pseudo-pressure P is defined in equation (5.3)

$$P(p) = \int_0^p 2\frac{\xi k_{rg} p}{\mu Z}\, dp \tag{5.3}$$

and replaced in equation (5.2) gives

$$\frac{\partial^2 P}{\partial r^2} + \frac{1}{r}\frac{\partial P}{\partial r} = \frac{1}{\eta}\frac{\partial P}{\partial t} \tag{5.4}$$

where η is the diffusivity constant

$$\eta = \frac{0.006328\,\xi k_{\infty}}{\phi\mu c_t} \tag{5.5}$$

5.3.1 Matrix Dimensionless Variables

Matrix dimensionless pressure is defined as

$$P_D = \frac{P_i - P}{P_i - P_f} \tag{5.6}$$

Where P_i is initial reservoir pseudo-pressure, P_f is fracture pseudo-pressure

Matrix dimensionless time is

$$t_D = \frac{\eta}{{r_e}^2}\, t \tag{5.7}$$

Matrix dimensionless coordinate, r-direction

$$r_D = \frac{r}{r_e} \tag{5.8}$$

where r is radial coordinate and r_e is matrix radius of equivalent matrix cross section defined as

$$r_e = \sqrt{\frac{x_e\, y_e}{\pi}} \tag{5.9}$$

5.3.2 Equations

Boundary conditions of matrix block are:

$P(r, 0) = P_i$, at t=0, all reservoir at initial pressure

$\left.\frac{\partial P}{\partial r}\right|_{r=0} = 0$, symmetry of pressure in matrix block

$P(r = r_e) = P_f$, pressure continuity from matrix to fracture

In dimensionless variables equation (5.4) becomes

$$\frac{\partial^2 P_D}{\partial {r_D}^2} + + \frac{1}{r_D}\frac{\partial P_D}{\partial r_D} = \frac{\partial P_D}{\partial t_D} \tag{5.10}$$

And with boundary conditions

$P_D(r_D, 0) = 0$

$\left.\frac{\partial \mathrm{P}_D}{\partial r_D}\right|_{r_D=0} = 0$

$P_D(r_D = 1) = 1$

Equation (5.10) is converted into Laplace domain

$$\frac{\partial^2 \overline{P_D}}{\partial {r_D}^2} + \frac{1}{r_D}\frac{\partial \overline{P_D}}{\partial r_D} = s\overline{P_D} + \overline{P_D}(r_D, 0) \tag{5.11}$$

And with boundary condition in Laplace domain

$\overline{P_D}(r_D, 0) = 0$

$\left.\frac{\partial \overline{P_D}}{\partial r_D}\right|_{r_D=0} = 0$

$\overline{P_D}(r_D = 1) = \frac{1}{s}$

The general solution of (5.11) is

$$\overline{P_{mD}} = A\,\mathrm{I}_0\left(\sqrt{s}r_D\right) + B\,\mathrm{I}_1\left(\sqrt{s}r_D\right) \tag{5.12}$$

where I_0 and I_1 are modified Bessel functions; A and B are determined by applying boundary conditions

$B = 0$

$A = \frac{1}{\mathrm{s}\,\mathrm{I}_0\left(\sqrt{s}\right)}$

Thus, matrix pseudo-pressure in Laplace domain is defined as

$$\overline{P_D} = \frac{\mathrm{I}_0\left(\sqrt{s}r_D\right)}{\mathrm{s}\,\mathrm{I}_0\left(\sqrt{s}\right)} \tag{5.13}$$

The pseudo-pressure derivative in Laplace domain is

$$\left.\overline{\frac{dP}{dr}}\right|_{r=r_e} = -\frac{\left(P_i - P_f\right)}{r_e}\frac{\mathrm{I}_1\left(\sqrt{s}\right)}{\sqrt{s}\,\mathrm{I}_0\left(\sqrt{s}\right)} \tag{5.14}$$

The gas flowrate from matrix to fracture is given by

$$q = \frac{k_m\,A_e}{1422\,T\,r_e}\left(P_i - P_f\right)\mathcal{L}^{-1}\left[\left.\overline{\frac{dP}{dr}}\right|_{r=r_e}\right] \tag{5.15}$$

Where $A_e = 2\pi\,r_e\,h$ and h is the matrix block thickness.

The Laplace inverse $\mathcal{L}^{-1}\left[\frac{\mathrm{I}_1(\sqrt{s})}{\sqrt{s}\,\mathrm{I}_0(\sqrt{s})}\right]$ is calculated in time domain using Stehfest (1970) algorithm.

5.4 Input Data

Table 5.1 presents the matrix, pore size distribution and reservoir properties used for matrix flow evaluation. The relative enhancement factor for gas under condensate banking effect is calculated using the results of the network model as described in Chapter 3. Table 5.2 provides the gas-condensate fluid composition which was used to generate the PVT

properties (such as gas viscosity μ and is compressibility factor, Z and condensate saturation). Figure 5.2 depicts the CVD condensate saturation as function of pressure. As the condensate flow in matrix is negligible, CVD reflects the phase behaviour of gas-condensate fluid in matrix.

Table 5.1: Matrix, Reservoir and Knudsen flow Input Data

Property	Value
Porosity, $\boldsymbol{\phi}$	0.10
Intrinsic permeability, $\boldsymbol{k_\infty}$ (nD)	150
Formation compressibility, $\boldsymbol{c_f}$ (psi-1)	1×10-6
Pore size median, $\boldsymbol{\nu}$ (nm)	10
Pore size standard deviation , $\boldsymbol{s}$ (nm)	0.6
Matrix block thickness, h (ft)	100
Initial Reservoir Pressure, $\boldsymbol{p_i}$ (psi)	4500

Table 5.2: Composition of gas-condensate fluid

Component	Molar Composition (%)
C1	80
C4	12
C7	7.2
C10	0.4
C14	0.4

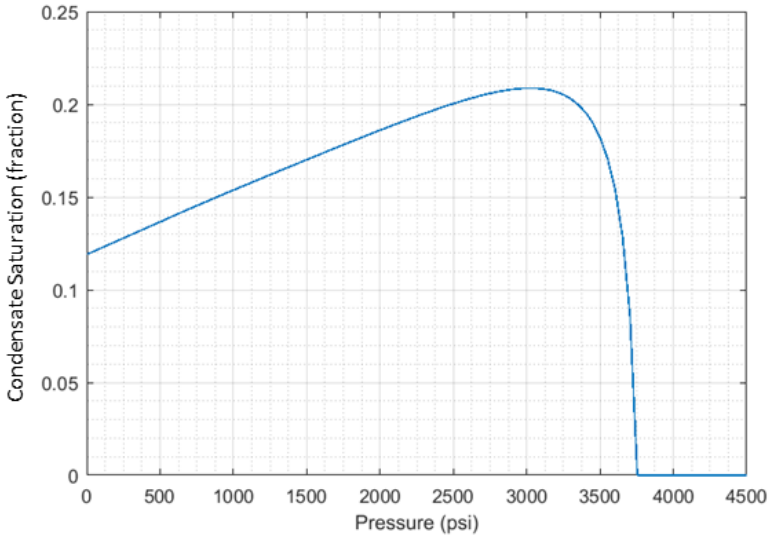

Figure 5.2: CVD Condensate saturation as function of pressure

5.5 Condensate Banking Effect

In this case, only condensate banking effect on production is investigated i.e. without introducing the Knudsen flow and phase behaviour deviation.

Figure 5.3 gives the log-log plot of gas production rate and Figure 5.4 shows the pressure profile in the matrix for different time steps. The R direction is oriented from the matrix centre at (r=0 ft) to the matrix edge (r= 177 ft) which is in direct contact with the fracture (the flow direction is from matrix centre to matrix edge). As showed in Figure 5.4, the pressure decline moves from the edge towards the centre and two pressure regimes can be distinguished: transient regime for t<166 days and pseudo-steady regime for t>166 days when the pressure decline reaches the matrix centre (see Figure 5.3).

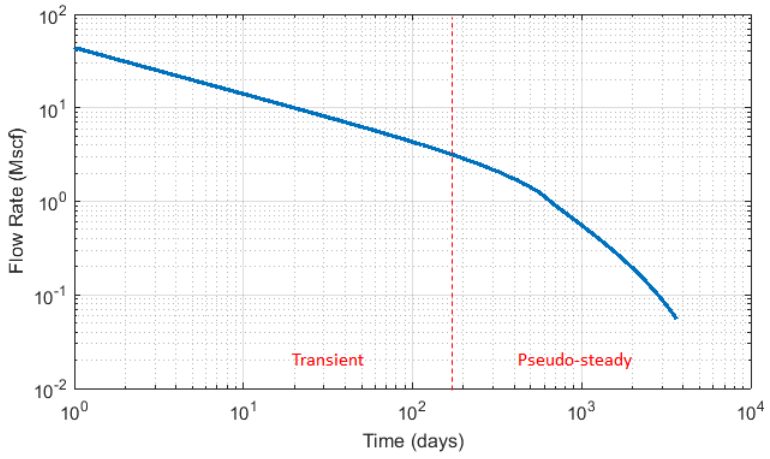

Figure 5.3: Log-Log plot of Gas flowrate showing transient regime and pseudo-steady state.

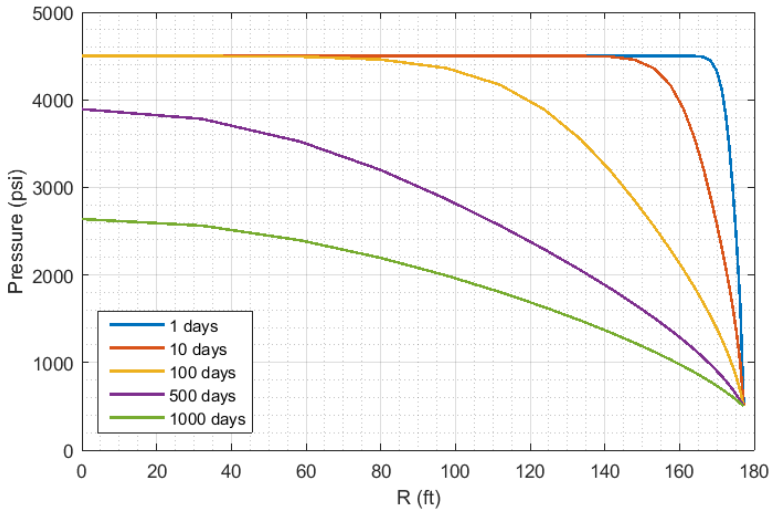

Figure 5.4: Matrix pressure profile for different time steps

As a result, when matrix pressure drops below dew point condensate starts to form first at the outer zone which is directly in contact with fracture and propagate towards the block centre. Figure 5.5a gives the condensate saturation profiles generated as function of pressure using CVD results. For instance, at t=0.8 days the free gas in the inner zone of the matrix in encircled by condensate ring of approximately 5 ft thickness. This condensate banking, enveloping the matrix, locks the gas inside the matrix under the effect of gas relative permeability reduction by condensate accumulation. Figure 5.5b illustrates the gas relative permeability profile in the matrix for different time steps and it shows the reduction of relative permeability as the condensate spreads from the edge to the block centre. For example, at t=10 days, although the most important part of the matrix is at free gas phase, it is encircled by a thin layer of highly reduced gas relative permeability.

This mechanism of condensate banking enveloping matrix blocks is a distinctive feature of shale gas-condensate reservoirs compared to conventional reservoirs where the condensate banking manifests mainly around the wellbore or the fracture face. A more detailed discussion of condensate propagation and accumulation in the reservoir is provided in Section 6.4.1.

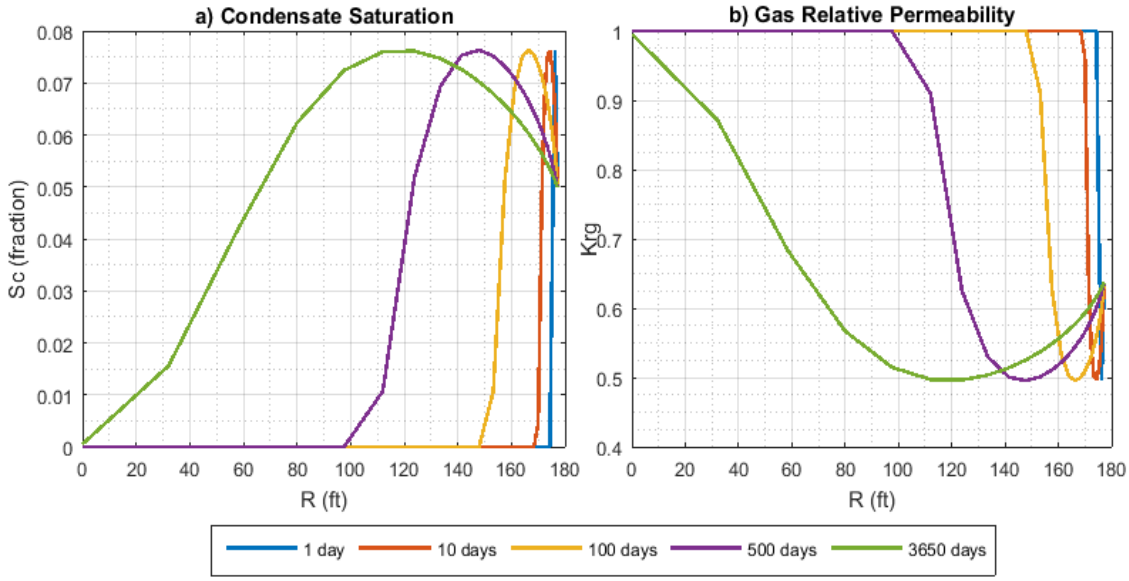

Figure 5.5: Matrix profiles for different time steps: a) condensate saturation and b) gas relative permeability

The gas cumulative production vs. time is shown in Figure 5.6 with and without condensate banking. The no condensate banking case was generated by using relative permeability equal to unity i.e. condensate saturation has no effect on gas permeability. In this example, the effect of condensate banking translates to about 30% loss of production.

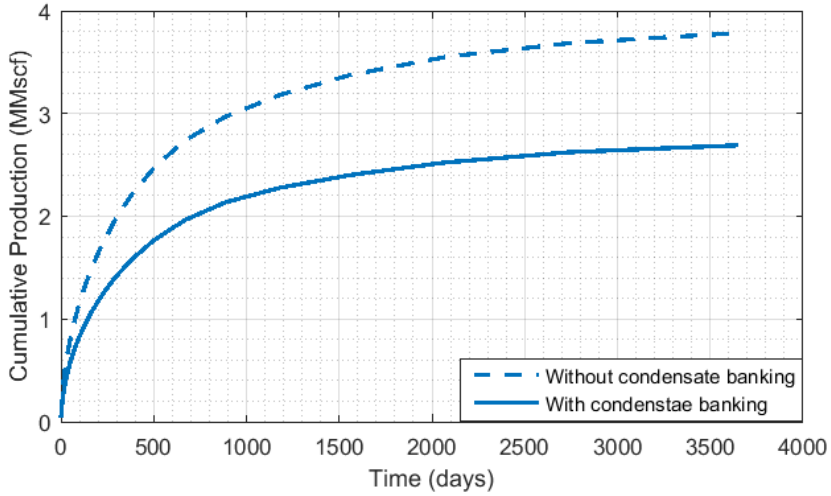

Figure 5.6: Condensate banking effect on matrix cumulative gas production

As mentioned in Section 2.5.3, the absence of effective enhanced recovery techniques to reduce the effect of condensate banking makes the production loss almost inevitable when producing from this type of reservoirs. This production loss makes the development of shale gas-condensate reservoirs more commercially challenging than dry shale gas reservoirs which should be carefully considered during field development studies.

Developing new techniques to minimise the production loss due to condensate banking will represent the main challenge that researchers and engineers have to tackle in order to improve the recovery of shale gas-condensate reservoirs.

5.6 Knudsen Flow Effect

The Knudsen flow enhances the gas permeability in shale matrix at pore pressure (see Figure 5.7). The Knudsen flow partially reduces the effect of condensate banking on gas permeability under dew point but its effect is significant only under 1000 psi while condensate banking forms under 3758 psi.

Figure 5.8 represents the gas flow rate of Darcy flow vs. Knudsen flow where gas flow rate is higher under Knudsen flow than Darcy flow resulting to a higher cumulative production by 25%. Figure 5.9 shows the ratio of Knudsen to Darcy flow $q_{Knudsen}/q_{Darcy}$ vs. average reservoir pressure and it indicates that $q_{Knudsen}/q_{Darcy}$ ratio increases as the reservoir pressure decreases.

The average matrix pseudo-pressure is derived from equation (5.6) in Laplace domain and calculated using equation (5.16)

$$\bar{P} = \frac{P_i}{s} - \left(P_i - P_f\right)\frac{\mathrm{I}_0\left(\sqrt{s}\,\frac{r}{r_e}\right)}{\mathrm{s}\,\mathrm{I}_0\left(\sqrt{s}\right)} \tag{5.16}$$

As expected, the Knudsen flow starts to have a significant effect when the reservoir pressure drops below 2000 psi.

As the condensate banking effect and Knudsen flow manifest at the same reservoir pressure range, Knudsen flow helps to alleviate partially the productivity decline of gas-condensate reservoirs.

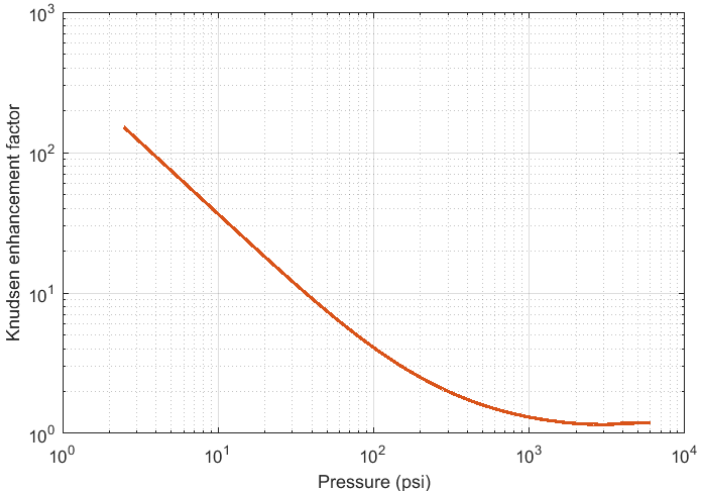

Figure 5.7: Gas permeability enhancement factor

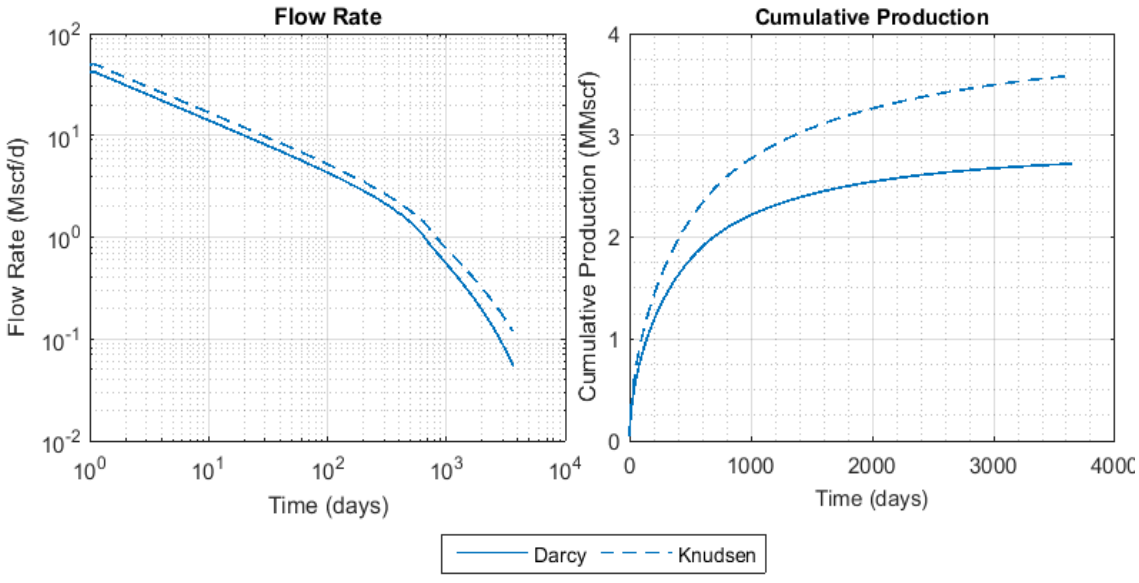

Figure 5.8: Gas flow rate and cumulative production of Darcy vs. Knudsen flow.

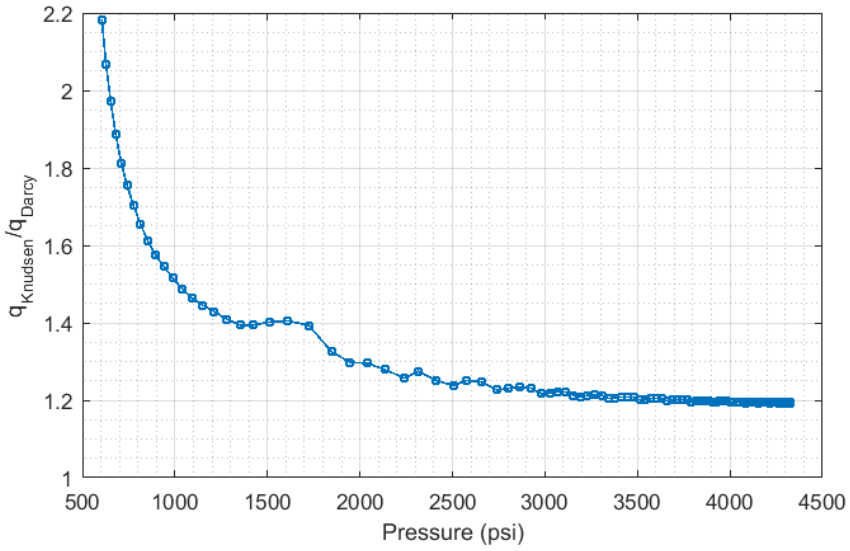

Figure 5.9: $q_{Knudsen}/q_{Darcy}$ vs. average reservoir pressure

In Figure 5.8, the effect of condensate banking on Knudsen flow was not considered. Here, the effect of the Relative Correction Factor ξ_{rel} is incorporated in order to reflect this effect on production. The pseudo-pressure P is modified by introducing ξ_{rel} in equation (5.3) to become

$$P(p) = \int_0^p 2\frac{(\xi_{rel}\,\xi\,)\,k_{rg}p}{\mu Z}\,dp \tag{5.17}$$

ξ_{rel} is described as function of condensate saturation and pressure as in Equation (3.38).

Figure 5.10 compares the cumulative production for Darcy flow, dry gas Knudsen flow (without correction to condensate saturation) and Knudsen flow under condensate banking (without correction to condensate saturation). This Figure shows that the condensate banking effect on Knudsen flow causes a reduction of 25% of the production gained by Knudsen flow (compared to Darcy flow). Consequently, not correcting the Knudsen flow to the condensate saturation effect leads to an overestimation of the production gain by Knudsen flow by 33% equivalent to an overestimation of the total production by 19%.

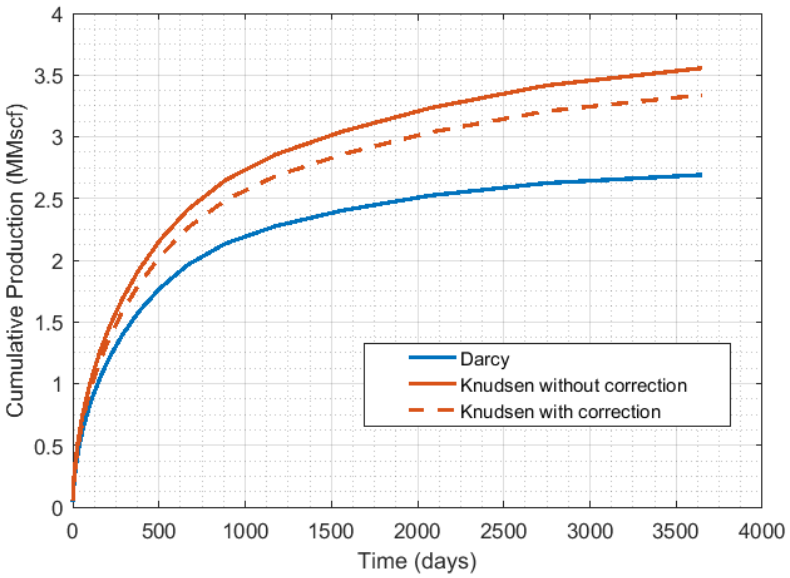

Figure 5.10: Gas flow rate and cumulative production of Darcy vs. Knudsen flow.

5.7 Phase Behaviour Effect

The phase behaviour deviation of gas-condensate fluids under capillary pressure induces a higher dew point and higher condensate saturation compared to bulk phase behaviour (Chapter 5). Figure 5.11 gives an example of CVD condensate saturation vs. pressure of lean condensate (see Table 5.2) showing higher condensate saturation. A higher condensate saturation results in a lower gas relative permeability. Figure 5.12 gives gas relative permeability vs. pressure under capillary pressure effect compared to bulk phase behaviour.

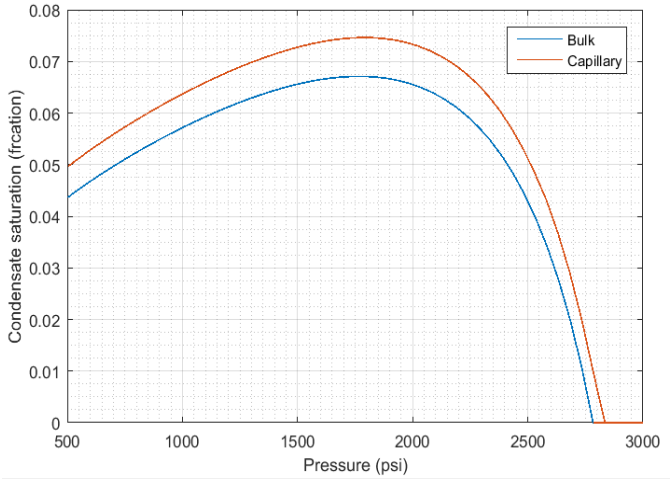

Figure 5.11: CVD condensate saturation of bulk vs. capillary phase behaviour

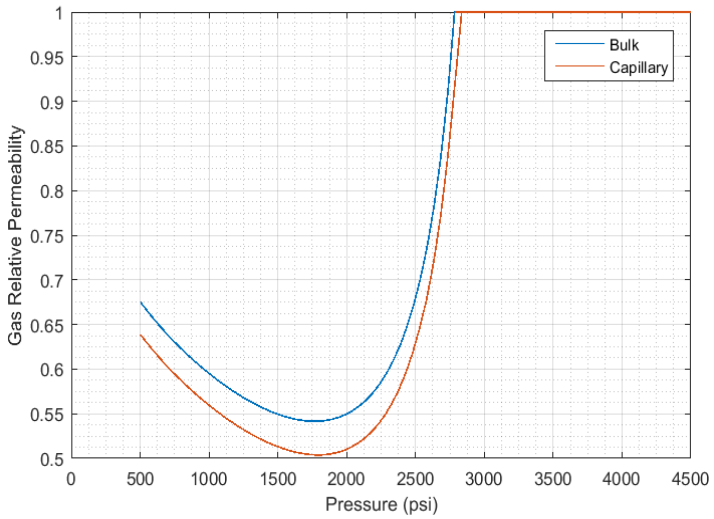

Figure 5.12: Gas relative permeability of bulk vs. capillary phase behaviour for lean condensate

The cumulative production under capillary pressure vs. bulk phase behaviour are presented in Figure 5.13. The production reduction is limited (about 5%). Similarly, Figure 5.14 gives the cumulative production of a rich condensate fluid with and without capillary pressure effect. This Figure shows a 2.5% production loss which is lower than in Lean condensate fluid.

Consequently, although the high capillary forces have an impact on the phase behaviour leading to a deviation in terms of dew point pressure and condensate saturation, its effect on the ultimate production is insignificant.

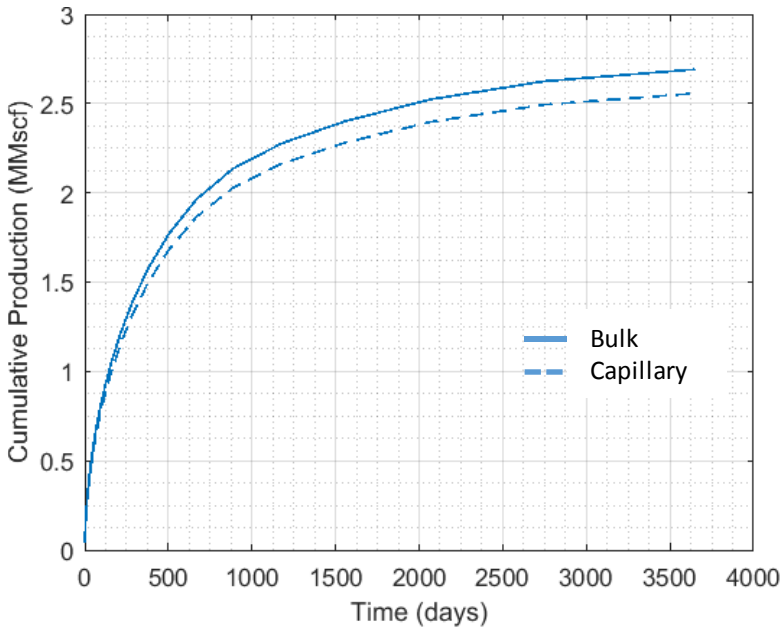

Figure 5.13: Gas cumulative production of bulk vs. capillary phase behaviour for lean condensate

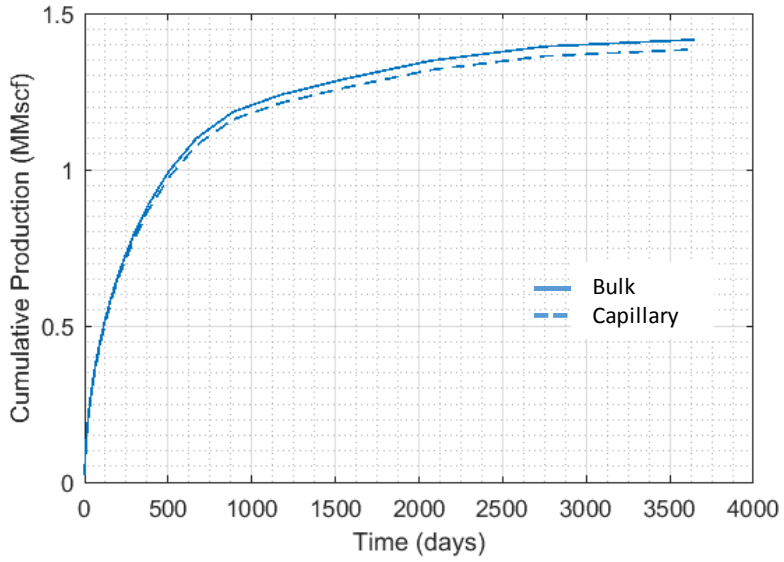

Figure 5.14: Gas cumulative production of bulk vs. capillary phase behaviour for rich condensate

5.8 Summary

The performance of shale gas-condensate reservoirs was investigated using a single matrix block with constant fracture pressure. The unavailability of rigorous analytical models and open source numerical simulation software makes this tool the only available way to investigate the flow behaviour and phase behaviour deviations.

Due to high capillary pressure in the matrix, the condensate banking in shale matrix induces a high productivity loss up to 30%. Thus, the development of this type of shale resources is considered challenging compared to oil and dry gas shale reservoirs.

In addition, results showed that condensate banking effect on Knudsen flow reduces the production gain by this type of flow by up to 25%. The use Knudsen flow with correction to the candidate saturation can lead to an overestimation of cumulative production by about 20%. The use of the Relative Correction Factor introduced in this thesis is crucial for an accurate evaluation of well performance of shale gas-condensate wells.

As addressed in Chapter 4, lean and rich condensate fluids exhibit different levels of phase behaviour deviation under capillary pressure in shale matrix. The effect of this phase behaviour on gas production has different degree of importance. The higher condensate

build-up in shale matrix of lean condensate fluids compared to bulk causes a production loss of 5% while rich condensate fluids have a limited impact (less than 2.5%).

CHAPTER 6: SHALE GAS-CONDENSATE RESERVOIR NUMERICAL SIMULATION AND PRODUCTION OPTIMISATION

6.1 Introduction

In Chapters 3 and 4, the deviation from conventional reservoirs of the flow behaviour and the phase behaviour in shale matrix were investigated at the micro-level. In Chapter 5, the effect of this deviation is evaluated using a semi-analytical model of shale matrix.

However, gas-condensate wells are a highly complex system that contains three different media; shale matrix, hydraulic fracture network and wellbore. These sub-systems have distinctive multiphase flow behaviour and phase behaviour where the condensate banking effect manifests differently. In shale matrix, with the high capillary forces in nano-scale pores, the impact of condensate accumulation is more severe than in fractures and wellbore. Thus, the effect of condensate banking in shale matrix has an impact on its interaction with the fracture network and the wellbore. This interaction controls the propagation of the condensate bank in the reservoir and as a result the well productivity.

This Chapter aims to provide a comprehensive study of how the condensate accumulation affects the whole well productivity and how it propagates in the reservoir.

3D compositional numerical simulation is used to model the shale gas-condensate reservoirs and to evaluate the condensate banking effect on production. Even though the commercial software used in this study (Eclipse) does not include the necessary functionalities to model flow behaviour deviation due to Knudsen flow and phase behaviour deviation due to capillary pressure, it can be used to build a basic understanding of the shale gas condensate wells performance and how condensate forms in the reservoir and affects the ultimate recovery.

Moreover, the well design optimisation in terms of hydraulic fracture spacing is investigated using numerical simulation and economic evaluation to identify the spacing that allows a maximum NPV (Net Present Value).

6.2 Limitations of Current Shale Gas-Condensate Reservoir Engineering Tools

The use of performance analysis for shale reservoirs is essential for field development design and planning to increase the shale plays profitability. In this Section, three conventional tools are reviewed in terms of the ability to be adapted to shale gas-condensate reservoirs: Decline Curve Analysis, Semi-analytical Models and 3D Reservoir Simulation.

6.2.1 Decline Curve Analysis

Presently, Decline Curve Analysis (DCA) technique is widely used for shale gas reservoir performance for economic studies and field development planning. The conventional DCA equation established by Arps (1945) is

$$q(t) = q_i(1 + bD_i t)^{-1/b} \tag{6.1}$$

Where q is flow rate (Mscf/d), q_i is initial flow rate (Mscf/d), D_i is nominal decline rate at $t = 0$, t is time (years) and b is Arps exponent.

Despite the simplicity and practicality of DCA, the complexity of reservoir performance and different production regimes cannot be described accurately with DCA models. Relatively short production history of shale wells makes using DCA analysis to establish long term production forecast very difficult. Instead, 3D reservoir models are used to generate long term production profiles and extract b value by fitting these profiles to equation (6.1). Nevertheless, different values of rate exponent b are needed for different production intervals to obtain an acceptable long term accuracy (Kanfar and Wattenbarger 2012, Kurtoglu, Cox and Kazemi 2011, Nelson, et al. 2014). These intervals consist of: a) different degree of flow contribution of sub-systems (hydraulic fractures, natural fractures and matrix), b) transient regime and boundary-dominated flow (BDF). In practice the determination of the number and limits of interval with different b values is difficult to achieve.

6.2.2 Semi-Analytical Models

Some semi-analytical models were developed by researchers (Brown and Ozkan 2009, Bello and Wattenbarger 2010, Stalgorova and Mattar 2013) to describe the gas flow from multi-stage fractured tight and shale gas reservoirs for pressure transient analysis and rate transient analysis.

The well is drilled in a Stimulated Reservoir Volume (SRV) with rectangular shape reservoir and by symmetry only ¼ of the model is described ($x_F \times y_e \times h$) where x_F is hydraulic fracture half length (ft), y_e is the fracture half spacing (ft) and h is the reservoir thickness (ft) (see Figure 6.1). The reservoir is modelled as fracture and matrix (dual porosity) with interaction function between matrix and fracture. The fluid flows from matrix through propped fracture to hydraulic fracture to the wellbore and the gas flow within propped fractures and within hydraulic fracture is described as linear flow. A convergence skin is introduced to take into consideration the flow convergence near wellbore in the hydraulic fracture. An outer region can be added to model the flow from unstimulated area. The system solution for constant bottomhole pressure (BHP) or constant rate is written in Laplace domain and converted to time domain using Stehfest's (1970) algorithm.

The main disadvantage of these models is the interference between stages: 1) in the SRV, where symmetry of drainage area is assumed, 2) in the wellbore, where the BHP is assumed to be the same along perforation clusters which is interpreted by calculation of well flow rate q_{well} as

$$q_{well} = N_{stages}\, q_{stage} \tag{6.2}$$

Where N_{stages} is number of stages and q_{stage} is stage flow rate calculated by the model.

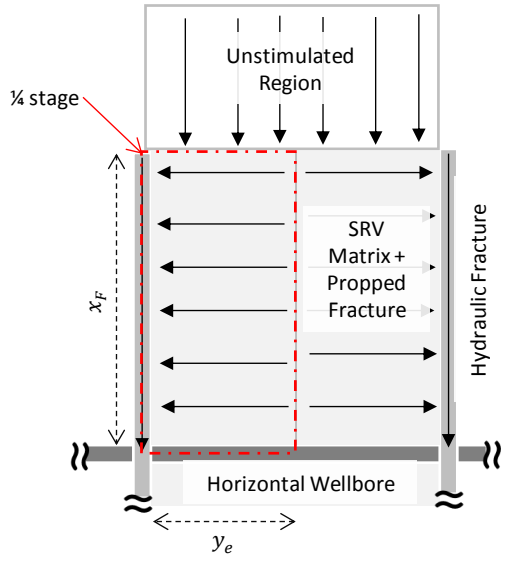

Figure 6.1: Schematic of gas flow in ¼ hydraulic fracture in shale gas wells model with (matrix+ fracture) SRV, hydraulic fracture and wellbore. Arrows indicate the linear flow assumption in unstimulated region, SRV and hydraulic fracture.

Although the gas-condensate phase behaviour and flow behaviour in shale matrix can be easily integrated into the gas pseudopressure function, it is difficult to assign two separate relative permeability models for matrix and fracture due to the limitation in Laplace domain.

6.2.3 3D Numerical Reservoir Simulation

3D numerical reservoir simulation models are the most powerful tools that can describe more accurately (than other tools presented above) the shale gas-condensate well performance. The reservoir is represented as dual permeability model i.e. both matrix-matrix and matrix-fracture flow is allowed. Local Grid Refinement (LGR) are used to logarithmically discretise the grid into smaller sub-cells around hydraulic fracture in order to capture the high pressure drawdown between hydraulic fracture and matrix.

Cipolla et al. (2010) introduced a new LGR method combined with dual permeability referred to as "*DK-LS-LGR*" (*dual permeability, logarithmically spaced local grid refinement*) method where the grid refinement is applied for the whole hydraulic fracture network through the SRV and not only around the primary hydraulic fracture (see Figure 6.2a). The reason behind using additional LS-LGR is to model the long transient regime that occurs in very low permeability matrix. Conventionally, analytical solutions by Warren and Root (1963) and Kazemi (1969) are used in reservoir simulation package to model fracture-matrix interaction. However, they cannot capture the transient regime in the matrix. On the other hand, despite the accuracy of *DK-LS-LGR* method it cannot be deployed for full field reservoir models because it can generate high number of cells with high volume heterogeneity which makes the simulation very expensive.

Another alternative to *DK-LS-LGR* method is MINC (Multiple Interacting Continua) method which consists of dividing matrix block to logarithmically spaced nested volumes in cylindrical or cubic shapes (see Figure 6.2b). The challenge of using MINC with LGR around hydraulic fracture in shale simulation is the very small cells that can be generated at the overlap of LGR and MINC methods in matrix cells around hydraulic fractures.

The gas-condensate phase behaviour is modelled with EOS (Equation of State) matched to the lab experiments results (such as CCE, CVD, flash calculation). A major difficulty of using compositional reservoir simulation tools in this work is the lack of flexibility to implement modified gas condensate flow models and phase behaviour models in the software source code.

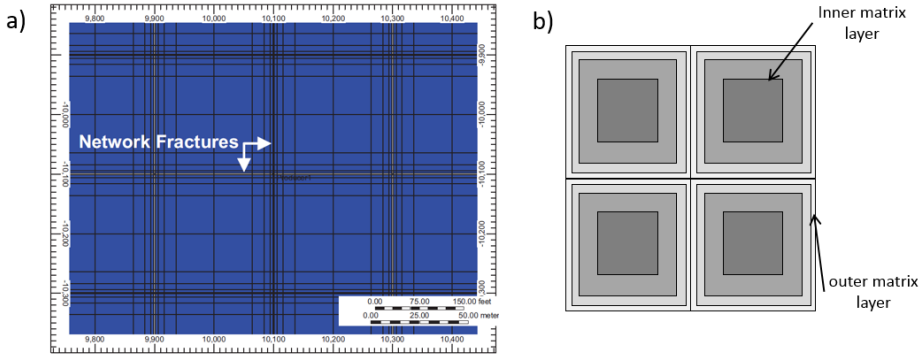

Figure 6.2: Reservoir modelling techniques for shale: a) *DK-LS-LGR* method , b) MINC method.

6.3 Reservoir Model Description

6.3.1 Fracture Network

Multistage fracturing of horizontal well has become the standard well completion for shale wells where this type of completion is required to reach an economic production volume. Fisher et al. (2002) , Maxwell et al. (2002) and Fisher et al. (2004) used micro-seismic (M-S) data to observe the propagation of hydraulic fracture in Barnett Shale and they identified that induced fractures are extremely complex (pattern C in Figure 6.3) than the simple plan fracture (A pattern Figure 6.3).

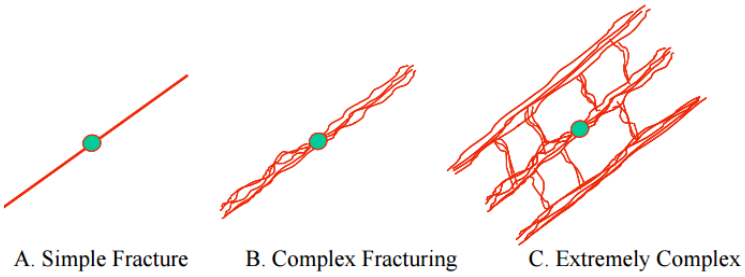

Figure 6.3: Increasing complexity levels of fractures (Fisher, et al. 2002).

Figure 6.4 represents an Example of M-S mapping of extremely complex fracture network in core area of Barnett Shale reported by Fisher et al. (2004). This fracture network length is 4000 ft (2000 ft half length) and width is about 1200 ft. The grey dots are the recorded M-S events and the straight lines show the interpreted fracture structures. The red dots represent the killed wells by the treatment.

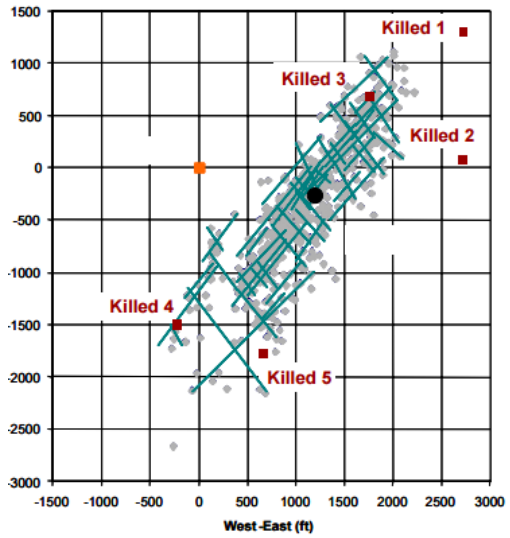

Figure 6.4: Example of M-S mapping of extremely complex fracture network in core area of Barnett Shale (Fisher et al. 2004)

Fisher et al. (2002) suggested that the observed complexity of fracture network is a result of re-opening of existing natural fractures. In this example the average spacing between fractures is 100 ft.

In this work, data of Fisher et al. (2004) is used to idealise the fracture network with a constant fracture network spacing $D_x = D_y$ in x –direction and y-direction respectively to build a general model. Figure 6.5 shows the fracture network modelling within ¼ SRV with constant fracture network spacing D_x of 100 ft, a hydraulic fracture half-length of 1000 ft and a hydraulic fracture spacing (stage width) of 600 ft.

The fracture network spacing D_x and the hydraulic fracture half-length vary according to reservoir properties and the treatment program design. Generally, a hydraulic fracturing simulator is used to optimise hydraulic fracture geometry (width, half-length and height) and then select the treatment fluid and proppant (Economides and Wang 2010, Fonseca and Farinas 2013). The impact of natural fracture spacing is investigated in Section 6.4.4.

The hydraulic fracture spacing of 600 ft was extracted from data of Fisher et al. (2004) presented in Figure 6.4. The hydraulic fracture spacing optimisation is discussed later in Section 6.5.

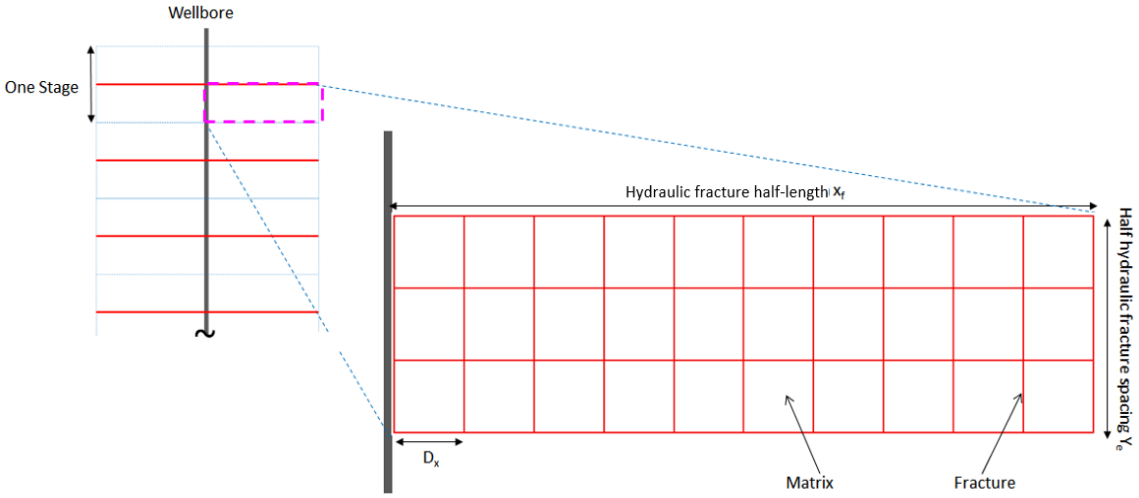

Figure 6.5: Schematic of fracture network modelling in ¼ SRV with constant fracture network spacing $D_x = D_y = 100\ ft$

6.3.2 Stress Dependent Fracture Conductivity

Reservoir geomecahnics play an important role in well performance as well as in well fracturing. The in-situ stress is a combination of overburden stress, tectonic stress and pore pressure. As the reservoir pore pressure declines with production, the in-situ stress increases resulting in fracture conductivity reduction due to proppant embedment and crushing in fractures. Numerous correlations were proposed to model fracture conductivity as a function of stress (Raghavan and Chin 2002, Rutqvist et al. 2002, Nur and Yilmaz 1985, Wasaki and Akkutlu 2015, Kwon et al. 2001). The fracture conductivity can be described by Equation (6.3)

$$C_f = C_{f_0} \exp\left[-A\,\sigma_{eff}\right] \tag{6.3}$$

Where C_f is the conductivity in md.ft at the current effective stress σ_{eff} in psi, C_{f_0} the initial conductivity in md.ft, σ_{eff} is the effective stress, and A is an empirical coefficient which estimated by lab experiments or by well production analysis.

The effective stress σ_{eff} is defined as the difference between normal stress σ_n and fracture fluid pressure P (Economides et al. 2000) as

$$\sigma_{eff} = \sigma_n - \alpha P \tag{6.4}$$

where α is Biot's coefficient, it describes to which extent the pore pressure counteracts elastic deformation of porous media (Biot 1941). Havens and Batzle (2011) and Jun and Kegang (2014), using experimental measurements of Bakken shale formation, reported Biot's coefficient ranges from 0.57 to 0.75.

Cipolla et al. (2010) used experimental data to estimate the stress-dependent conductivity of fracture network for Barnett shales. FAN et al. (2010) derived the fracture permeability reduction by analysing Haynesville shale gas production (see Figure 6.6).

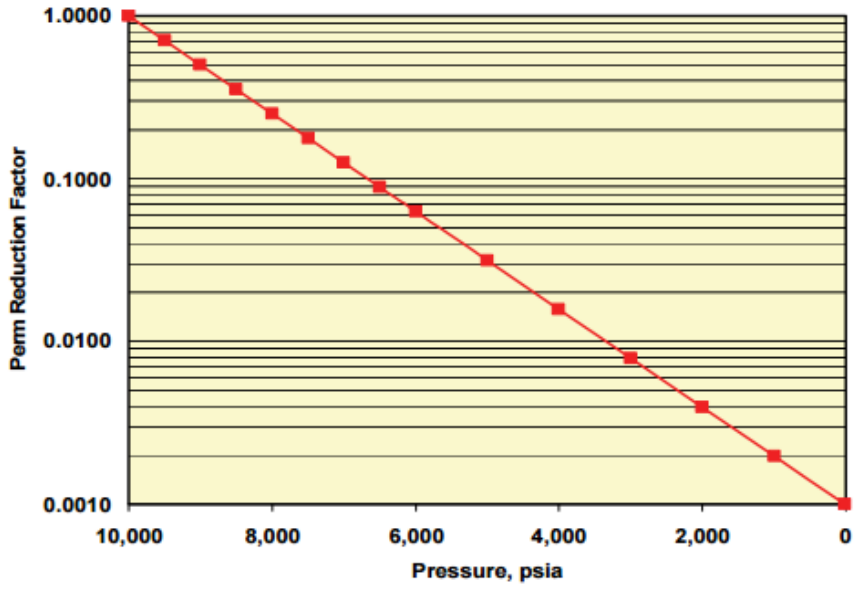

Figure 6.6: Haynesville hydraulic fracture permeability reduction factor vs. fracture fluid pressure (Fan, Thompson and Robinson 2010).

6.3.3 Non-Darcy Flow

The high gas velocity with high Reynold number in the hydraulic fracture shifts gas flow from Darcy laminar flow to non-Darcy turbulent flow causing a reduction of apparent conductivity. The Forchheimer correction to Darcy law is given in Equation (6.5)

$$\frac{dP}{dx} = \left(\frac{\mu}{k\,A}\right) q + \beta\,\rho \left(\frac{q}{A}\right)^2 \tag{6.5}$$

Where q is the volumetric flow rate, k is the rock permeability, A is the section area, μ is the fluid viscosity, ρ is the fluid density and β is the Forchheimer parameter.

Several β correlations were developed based on core experiments, proppant tests and analytical studies (Li and Engler 2001, Lopez-Hernandez, Valko and Pham 2004). Two types of correlation can be distinguished:

a) Correlations with permeability: the turbulent factor β is expressed only as function of fracture permeability as

$$\beta = \frac{a}{{k_f}^b} \tag{6.6}$$

where β in ft^{-1}, k_f is fracture permeability in mD and a and b are correlation constants. The first fracture only correlation was developed by Cooke (1973) using brine, oil and nitrogen and different proppant sizes. Cooke's correlation constants are listed in Table 6.1.

Table 6.1: Constants a and b in Cooke equation

Sand Size (mesh)	a	b
8/12	5.38e+11	1.24
10/20	8.51e+11	1.34
20/40	3.41e+11	1.54
40/60	2.14e+11	1.60

In a similar approach Pursell and Blakely (1988) carried out nitrogen injection through different proppant sizes and they gave a and b constants (shown in Table 6.2) for two sand meshes 10/20 and 20/40.

Table 6.2: Constants a and b in Pursell and Blakely (1988) equation

Sand Size (mesh)	a	b
10/20	5.30e+10	1.14
40/60	2.35e+10	1.12

Martins et al. (1990) used nitrogen injection at ambient temperature and high flow rates and different sand mesh sizes. They found that a and b constants are not affected by the sand mesh size and they proposed the following equation

$$\beta = \frac{8.23E+09}{{k_f}^{1.04}} \tag{6.7}$$

Jones (1987) used 335 sandstone and 29 limestone cores with permeability from 0.01 to 2,500 mD and from 0.01 to 400 mD respectively. Only helium was used in his experiments. Jones presented the following correlation

$$\beta = \frac{6.15E+10}{{k_f}^{1.55}} \tag{6.8}$$

b) Correlations with permeability and porosity: equations are similar to previous type with addition of porosity to the correlation

$$\beta = \frac{a}{{k_f}^b \phi^c} \tag{6.9}$$

where ϕ is porosity and c is a constant. Janicek and Katz (1955) performed experiments on sandstone, dolomite and limestone and developed the following correlation

$$\beta = \frac{1.82E+8}{{k_f}^{1.25} \phi^{0.75}} \tag{6.10}$$

Tek et al. (1962) derived partial differential equations and used Janicek and Katz (1955) data to formulate their correlation

$$\beta = \frac{5.5E+9}{{k_f}^{1.25} \phi^{0.75}} \tag{6.11}$$

Belhaj et al. (2003) developed numerical model for Non-Darcy flow in porous media and they validated their model with water injection through cores experiments. They subsequently proposed equation (6.12)

$$\beta = \frac{1.15E+7}{k_f \phi} \tag{6.12}$$

Lopez-Hernandez et al. (2004) recommended the use of Martins et al. (1990) correlation or Pursell and Blakely (1988) correlation as general equation for non-Darcy analysis in fractures in absence of experimental data.

6.3.4 Dual Porosity/Permeability Models

In order to model the two different media, matrix and fracture (natural or induced hydraulically) and dual porosity/permeability models are used to simulate the interaction between matrix and fracture. In commercial simulators, the matrix fracture interaction is only modelled using analytical dual porosity models as Warren and Root (1963) and Kazemi (1969). The analytical solutions were developed for pseudo-steady-state flow regime in the matrix. However, in shale reservoirs, due to very low permeability, transient flow regime in matrix controls an important period of well life.

6.3.5 Grid

Gridding in this numerical reservoir simulation is a very important element due to existence of three different media: reservoir matrix, natural fracture and hydraulic fracture network. Hydraulic fracture network needs to be modelled separately in order to be able to characterise it with different reservoir properties: porosity, permeability, non-Darcy flow and stress-dependent conductivity.

In addition, due to the high pressure draw down between fracture and matrix, logarithmic grid refinement is necessary to model the pressure distribution in the matrix during the transient flow regime. Using coarse cells instead of grid refinement makes the matrix to enter in a pseudo-steady state directly after production starts, which leads to an overestimated production.

Cipolla et al. (2009) and Rubin (2010) studied reservoir modelling for shale dry gas using local grid refinement and dual permeability techniques. This technique is usually referred to as "DK-LS-LGR" (i.e. for dual permeability, logarithmically spaced, local grid refinement). They concluded that a simplified grid with 9×9 logarithmic grid refinement for matrix blocks and 2 ft wide grid for each fracture can simulate accurately the shale gas reservoirs. Cipolla et al. (2009) used a high resolution grid of 43×43 grid refinement and 0.001 ft wide grid as reference solution for the simplified grid. Rubin (2010) used a similar approach with finely-gridded reference model (approximately 6-14 million cells).

MINC (Multiple Interacting Continua) is another technique used widely to model the transient flow in matrix in dual porosity models and it is also called discretised matrix or multi-porosity model. In this technique, the matrix is sub-divided to nested volumes (usually from 3 to 7 volumes) while the fractures are modelled by one cell. Rubin (2010) used a dual porosity model with 4 nested MINC matrix cells and one MINC cell for fracture. He compared the MINC solution to the reference fine grid model and concluded that MINC technique provided inaccurate results due to the lack of direct connection between matrix and fracture through matrix-cell because of the dual porosity models where connection is limited to matrix-fracture.

In this study, hydraulic fractures are represented with 1 ft wide cells and matrix blocks are modelled with 100 ft wide cells which is the hydraulic fracture network spacing. The intrinsic width of hydraulic fracture is 0.001 ft. Figure 6.7 shows the *DK-LS-LGR* method used in this work with 9×9 logarithmic grid refinement (as proposed by in matrix blocks and 1 ft wide cells for fractures). Intrinsic properties of fractures (porosity, permeability and non-Darcy coefficient) are upscaled from 0.001 ft thickness to effective 1ft cell thickness. For example, the intrinsic permeability of 4000 mD in 0.001 ft is upscaled to 4 mD permeability for the effective thickness of 1 ft.

Only ¼ of SRV is modelled due to symmetrical flow across the wellbore and primary hydraulic fracture. The half hydraulic fracture length, x_f is 1000 ft and spacing of 300 ft which is equivalent to 16.5 acres. Table 6.3 lists the SRV properties.

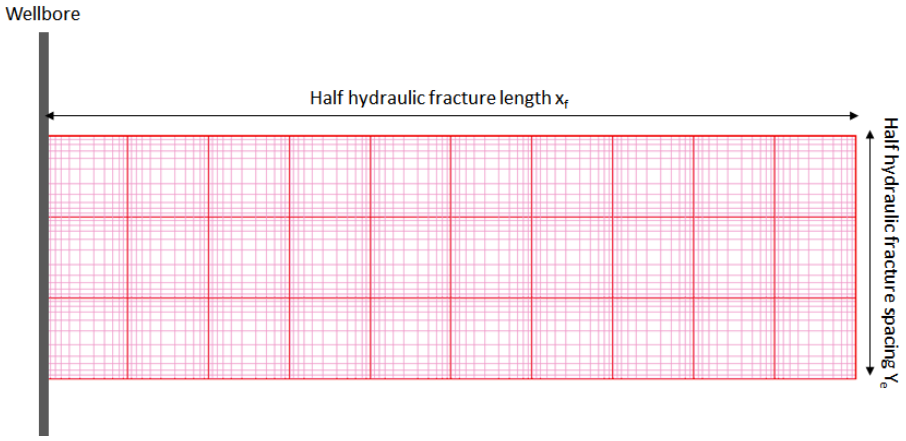

Figure 6.7: Logarithmic grid refinement of 9×9 in matrix blocks and 1 ft wide grid for fractures.

Table 6.3: Properties of Stimulated Reservoir Volume

Property	Value
Porosity, ϕ	0.10
Permeability, k_∞ , nD	150
Compressibility, psi^{-1}	1×10^{-6}
Pore size median, nm	10
Pore size standard deviation, nm	0.6
Matrix block thickness, *h*, ft	100
Initial Reservoir Pressure, psi	4500
Connate water saturation	20%

6.3.6 Gas-Condensate Fluid

The gas condensate fluid used in the simulation is a gas-condensate with an API gravity of 50˚ and CGR (Condensate Gas Ratio) of 110 stb/MMscf. The reservoir temperature is 310 ˚F. The fluid composition was derived from literature (Orangi, et al. 2011) which was estimated from an Eagle Ford gas-condensate well. Figure 6.8 shows the phase envelope of the gas condensate fluid. At reservoir conditions, the dew point is 3730 psi. Figure 6.9 gives the CVD (Constant Volume Depletion) experiment simulation of the gas-condensate fluid with a maximum condensate saturation of 28%. Table 6.4 represents the EOS (Equation of State) parameters of the gas-condensate fluid used in the simulation.

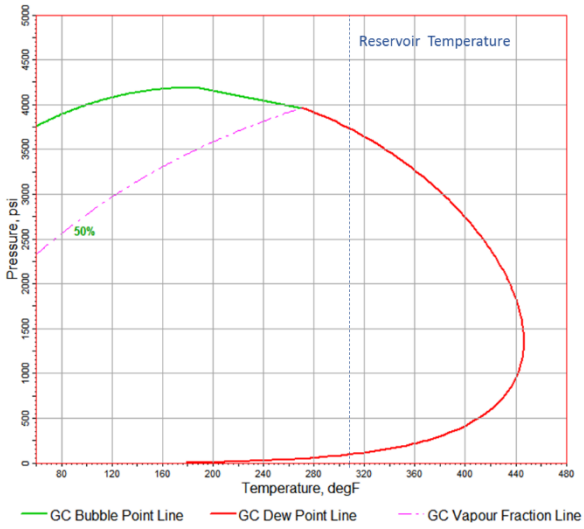

Figure 6.8: Gas-condensate phase envelope

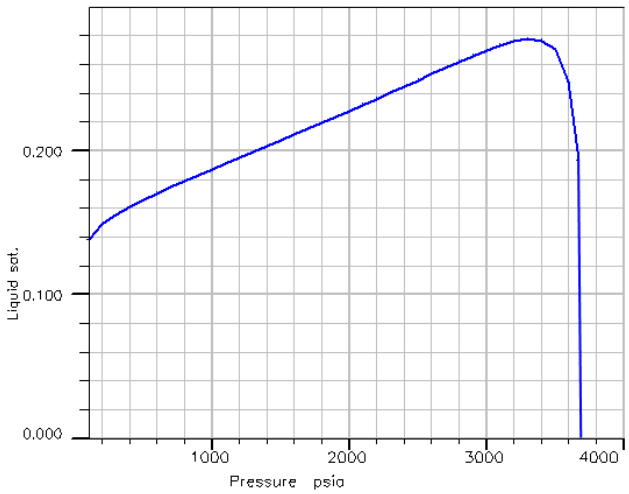

Figure 6.9: CVD (Constant Volume Depletion) simulation of the gas-condensate fluid at reservoir condition.

Table 6.4: EOS parameters for gas-condensate fluid used in simulation

Components	Mol Weight	Mol Fraction (%)	Crit Pres (psia)	Crit Temp (K)	Omega A	Omega B	Acentric Factor	V Crit (ft3 /lb-mole)	Z Crit
C1	16.043	68.72	667.78	190.6	0.45724	0.077796	0.013	1.5698	0.28473
C2	30.07	8.34	708.34	305.43	0.45724	0.077796	0.0986	2.3707	0.28463
C3	44.097	4.67	615.76	369.8	0.45724	0.077796	0.1524	3.2037	0.27616
C4	58.124	1.05	529.05	408.1	0.45724	0.077796	0.1848	4.2129	0.28274
NC4	58.124	1.83	550.66	425.2	0.45724	0.077796	0.201	4.0847	0.27386
NC5	72.151	0.79	488.79	469.6	0.45724	0.077796	0.251	4.9817	0.26844
C5	80.447	2.02	483.39	488.8	0.45724	0.077796	0.25315	5.3347	0.27312
C6+	138.41	12.59	368.37	619.69	0.45724	0.077796	0.44641	8.754	0.2694

6.3.7 Relative Permeability Model

While relative permeability in hydraulic fractures is well documented, researchers tend to use the conventional two phase/multiphase relative permeability models for shale matrix. However, the high capillary pressure in shale matrix compared to conventional reservoir makes the two phase/multiphase flow in shale matrix different. For gas condensate shale reservoir. It was concluded in Chapter 3 that condensate is almost immobile in shale matrix. Consequently, using a conventional gas condensate relative permeability would overestimate the condensate flow from matrix to fracture leading to an overestimation of well production. Figure 6.10 gives the relative permeability used in this simulation. For gas-condensate relative permeability in fractures straight line model is used.

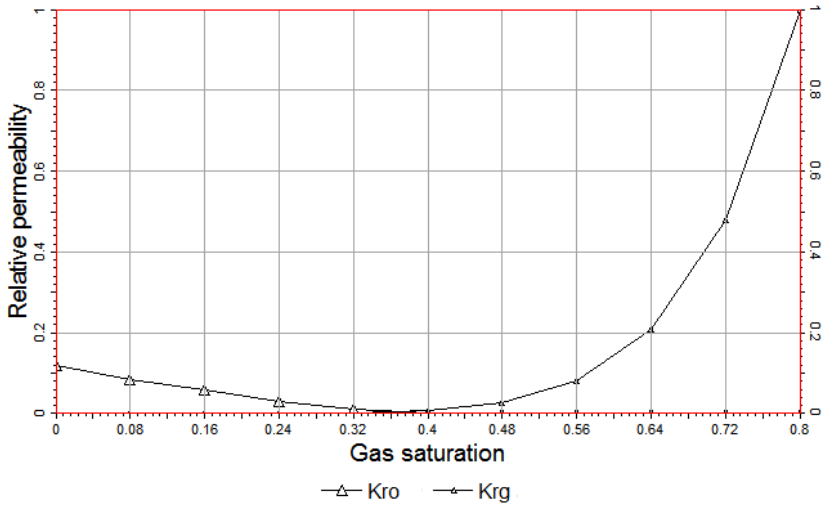

Figure 6.10: Relative permeability model for shale matrix with almost immobile condensate due to high capillary pressure

The main DATA input file of Eclipse 300 is given in Appendix B.

6.4 Shale Gas-Condensate Well Performance

6.4.1 Effect of Condensate Banking

Condensate banking (accumulation) in the reservoir represents the first concern when evaluating well deliverability and CGR output. Additionally, given that the multiphase flow and the completion design (SRV) in shale reservoirs are different from conventional reservoirs, understanding how condensate forms and how it affects the well productivity is of vital importance in gas-condensate reservoir engineering.

Figure 6.11 shows reservoir pressure and condensate saturation at 3 months, 1 year and 3 years of production for Reference run and Figure 6.12 shows the gas relative permeability at the same time steps.

As the flowing bottomhole pressure is lower than dew point, condensate starts to build up in fractures near to the wellbore from the first weeks of production (see Figure 6.11a). Few weeks/months later, the condensate spreads into the matrix around the wellbore as the adjacent fracture pressure goes below dew point. The propagation of condensate banking in the matrix blocks happens from the outer layer towards the centre as the pressure decline travels from the edge to the centre. At this stage, the condensate banking is limited to the matrix blocks at the well bore vicinity (see Figure 6.11b).

After 15 months of production, as the pressure declines below the dew point through the SRV, the condensate banking is propagated into the whole SRV enveloping the matrix blocks into a layer of condensate liquid while the free gas is locked in the centre zone (see Figure 6.11a and b). The effect of condensate banking is two-folds; it reduces the gas relative permeability to flow from matrix to fracture, and it makes the heavy components to get stuck in the matrix reducing the CGR (Condensate Gas Ratio) at the surface. Figure 6.13 represents the CGR of produced fluid and the average SRV pressure, it is indicating a sharp decline of heavy components production at surface after 1 year of production even when the average pressure is still around 4500 psi.

After three years of production, the pressure decline reaches all matrix blocks centres but still above the dew point with only free gas in the matrix blocks centre through all SRV (see Figure 6.11a and b).

Figure 6.14 indicates the average poressure of fractures and matrx blocks and it shows the differnce of pressure decline with time. After one year productuion, the fractre pressure starts to decline further than the previous period (first year of production) due to the lack of pressure support from the matrix blocks which are envelopped by condensate. The condenate banking plays a role of a dynamic skin in the matrix, reducing the connectivity to fracture network.

While the ultimate recovery factor for gas is about 35%, only 10% of condensate is recoverable due to the reduction of CGR through the production period.

In order to evaluate the effect of condensate banking on production, a “Dry Gas” run was built with dry gas fluid and the same reservoir and completion properties. Although dry gas and gas-condensate fluids have different fluid properties (density, viscosity, CGR and

relative permeability), the comparison of gas production of dry gas and gas-condensate cases can give an indicative evaluation of condensate banking effect.

Figure 6.15 represents the gas cumulative production of Gas-condensate case (Reference case) compared to the “Dry Gas” case where the results show a production reduction due condensate banking is about 40%.

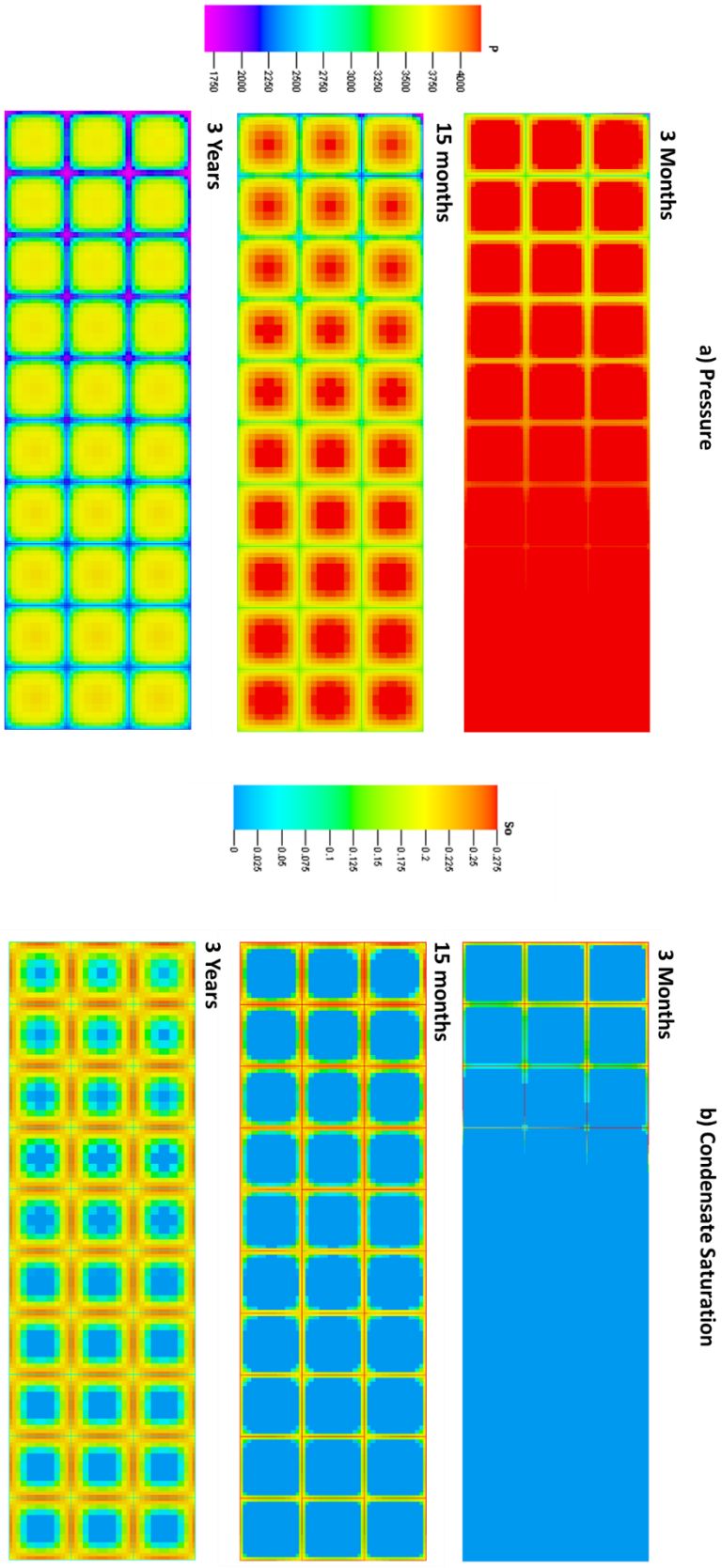

Figure 6.11: a) Reservoir pressure and b) condensate saturation at 3 months, 15 months and three years of production.

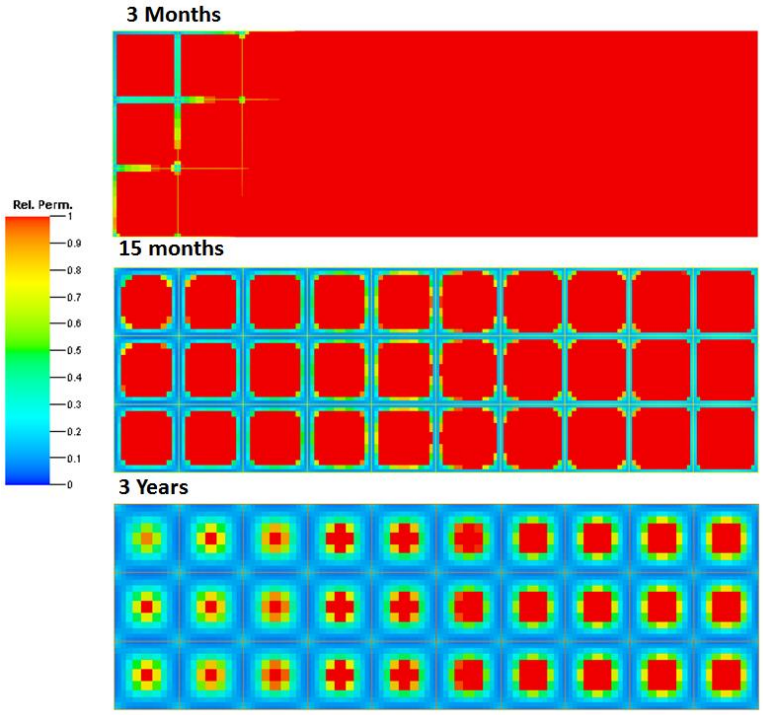

Figure 6.12: SRV gas relative permeability at 3 months, 1 year and three years of production.

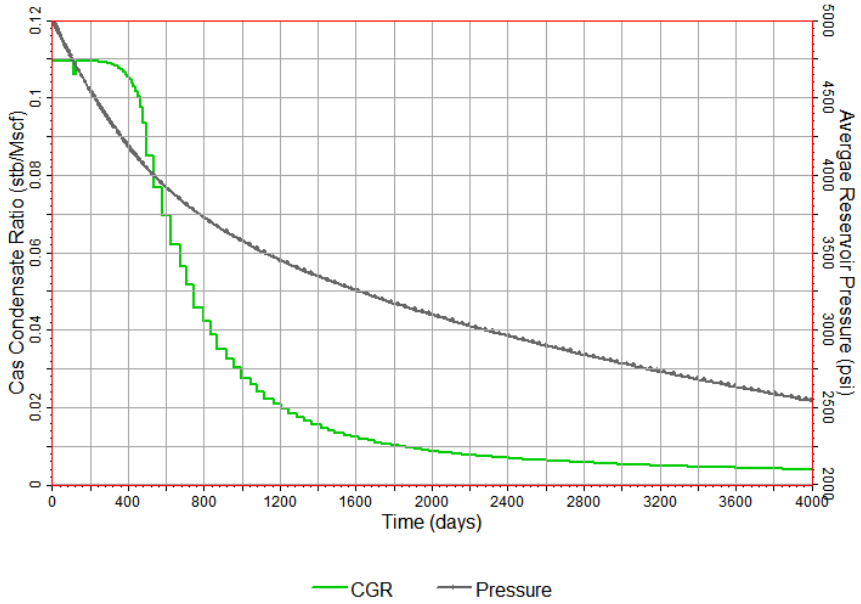

Figure 6.13: CGR and SRV average pressure.

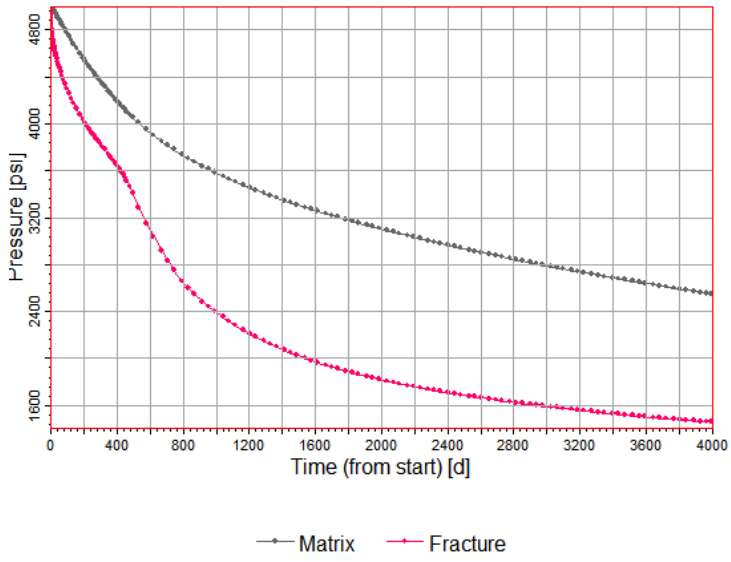

Figure 6.14: Average pressure for fracture and matrix.

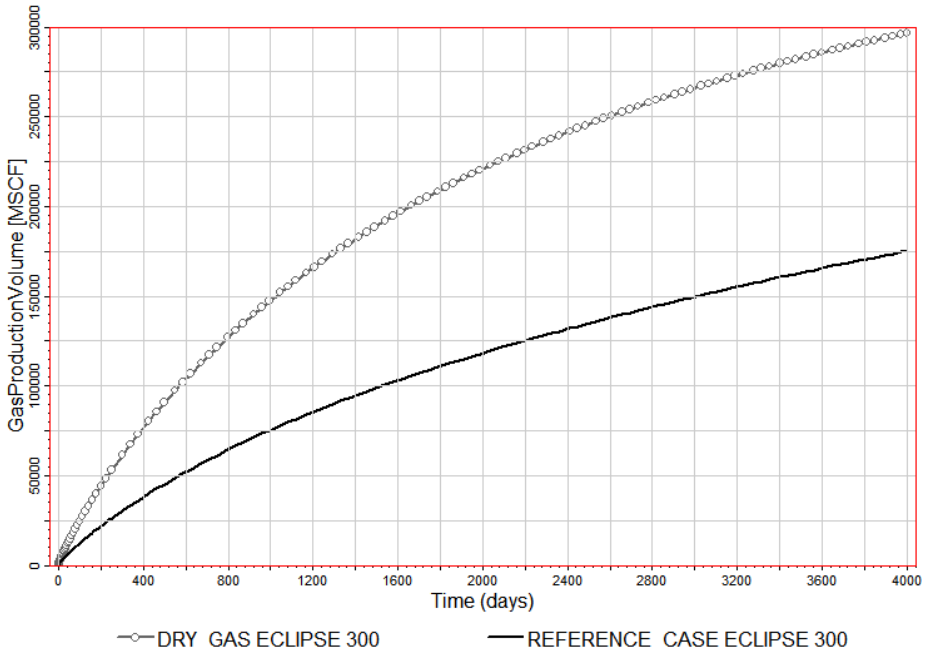

Figure 6.15: Gas cumulative production of Gas-condensate case (Reference case) vs. dry gas case showing the effect of condensate banking on production with reduction of 40%.

6.4.2 Effect of Stress-Dependent Permeability and Non-Darcy Flow

The effect of stress-dependent permeability was investigated by modelling the permeability reduction in the fracture network as function of pressure. The data used was derived from (Cipolla, Lolon et al. 2009). The stress-dependent permeability reduction function is applied only at fracture cells. Figure 6.16 gives the comparison of cumulative

gas production between Reference Case (without stress-dependent permeability) and STRESS-DEP-PERM (with stress-dependent permeability). The effect is about 10%. Non-Darcy flow has negative effect in shale, while in conventional reservoirs has a positive effect.

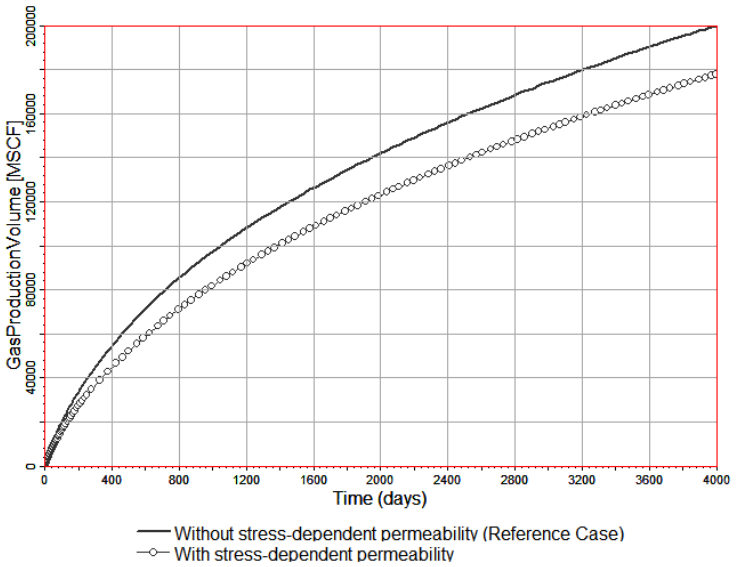

Figure 6.16: Effect of stress-dependent permeability: Reference Case (without stress-dependent permeability) vs. STRESS DEP PERM (with stress-dependent permeability)

6.4.3 Effect of Non-Darcy Flow

The non-Darcy flow is applied into the hydraulic fracture cells where the high gas velocity reduces the fracture conductivity. As the fracture width in the model is upscaled from intrinsic width of 0.001 ft to an effective width of 1 ft, the Forchheimer parameter β must be corrected. From equation (6.6) the non-Darcy differential pressure is written in terms of intrinsic fracture parameters

$$\left[\frac{dP}{dx}\right]_{ND} = \beta_{\infty}\,\rho\left(\frac{q}{w_{\infty}\,h}\right)^2 \tag{6.13}$$

where β_{∞} is the intrinsic Forchheimer parameter, w_{∞} is the intrinsic fracture width and h is the reservoir thickness.

Replacing intrinsic parameters in equation (6.13) with effective (upscaled) fracture parameters β_{eff} and w_{eff} results to

$$\beta_{eff} = \left(\frac{w_{eff}}{w_{\infty}}\right)^2 \beta_{\infty} \tag{6.14}$$

Using correlation from equation (6.6), β_{eff} can be expressed as

$$\beta_{eff} = \left(\frac{w_{eff}}{w_{\infty}}\right)^2 \frac{a}{{k_F}^b \phi^c} \tag{6.15}$$

In this study β_{eff} was estimated using Pursell and Blakeley (1988) correlation with proppant of 40/60-mesh sand (see Table 6.1). Figure 6.17a gives the cumulative production of Darcy flow vs. non-Darcy flow. The production reduction as a result of conductivity loss by non-Darcy flow is limited to 4%. Production loss in conventional reservoirs is much higher; being about 20% in high rate (120 MMscf/D) gas wells (Bybee 2006). Figure 6.17b shows the gas flowrate ratio of non-Darcy to Darcy flow. The effect of non-Darcy flow is more important at early production years when the gas flowrate is the highest. The lower non-Darcy effect in shale wells compared to conventional wells can be explained by the low gas flow rate in individual SRV compared to high gas flow that can be produced from hydraulically fractured wells.

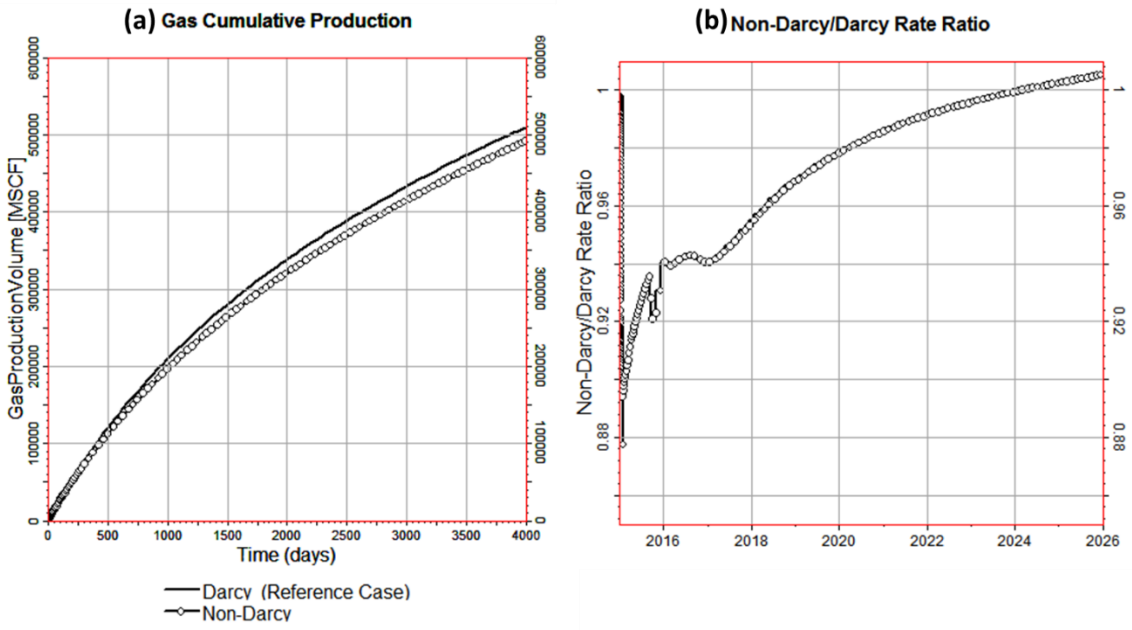

Figure 6.17: Darcy flow vs. non-Darcy flow: a) comparison of cumulative production and b) non-Darcy/Darcy gas rate ratio.

6.4.4 Effect of Fracture Network Spacing

The fracture network spacing D_x is the average distance between the hydraulic fractures in the SRV and it is equivalent to matrix block dimension. Sometimes, it is referred to as fracture network density which is the inverse of fracture network spacing. Figure 6.18 shows the results of sensitivity study of fracture network spacing D_x of 30, 65 and 100 ft. 65 ft spacing generates a production increase of 45 % and 30 ft spacing enhances the production by 140%; the lower fracture network spacing the higher the well productivity

Fracture network spacing has an important effect on well production which should be considered a high uncertainty factor in shale simulation. The level of uncertainty can be controlled by using the micro-seismic interpretation to estimate an average fracture network spacing D_x from the field.

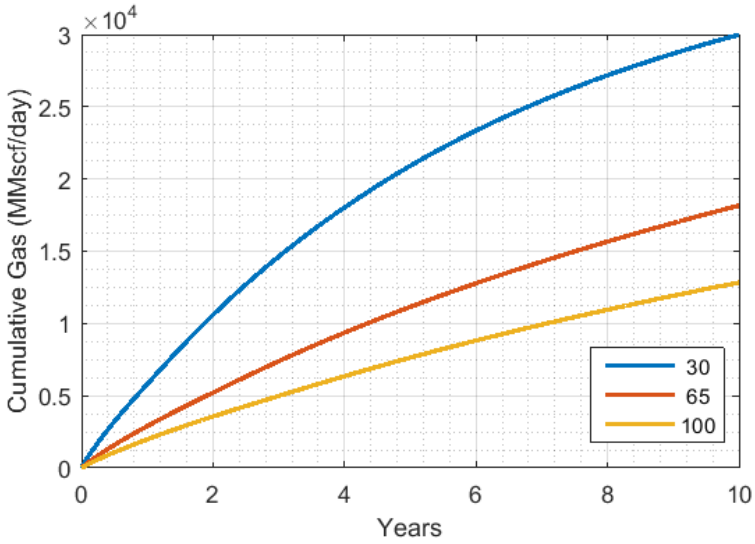

Figure 6.18: Effect of fracture network spacing D_x of 30, 65 and 100 ft.

6.5 Well Design Optimisation

As enhanced recovery techniques, including pressure maintenance and CO2 injection, are not yet proven to be effective for shale gas-condensate wells, the only available way to maximise their economic value is by optimising the well design. Furthermore, shale resources development are located at the higher part of field development CAPEX which includes long horizontal wells, multistage fracturing and re-fracturing. Minimising the production cost by Mscf is crucial to keep shale resources as competitive as possible with the other types of resources.

The most important factor in shale gas development is the hydraulic fracture spacing i.e. the distance between hydraulic fracture clusters. The shorter the spacing the higher the production and the higher the CAPEX. Table 6.5 lists the commercial factors (typical to the US shale plays) considered for economic optimisation of well design.

Table 6.5: Commercial coefficients used for optimisation

Fracturing Cost (M$/stage)	130
Gas Price ($/Mscf)	2.3
Discount Rate	10%
Operational Cost (USD/Mscf)	0.6
Drilling Cost with lateral length 5,500 (MM$)	3
Tax (%)	20
Condensate Price ($/bbl)	40
Production Period (years)	10

Figure 6.19 represents results of cumulative production for different fracture spacing from 100 to 600 ft with 100 ft increment. The cumulative production is inversely proportional to fracture spacing where the highest production is about 16,000 MMscf with 100 ft spacing. The first year of production represents 23-36% of total 10-years production because of the high decline rate of production from one year to another.

Figure 6.20 shows comparison of cash flow and NPV (Net Present Value) for different cases of fracture spacing. Lower fracture spacing 100 and 200 ft have the lowest payback period about 19 months. However higher spacings have longer payback periods that range from 2 to 4 years.

Although 100 ft spacing results in the highest production, when considering NPVs, fracture spacing 200 ft represents the optimum spacing with maximum NPV of 6.7 MM$.

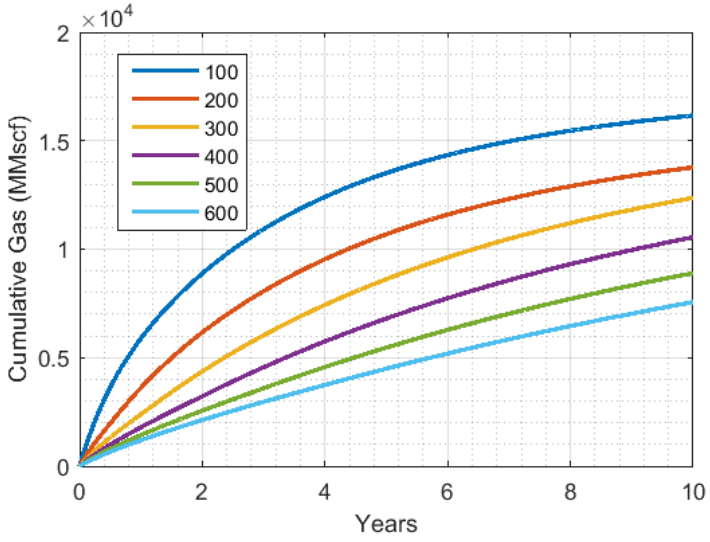

Figure 6.19: Cumulative Production sensitivity to hydraulic fracture spacing of 100, 200, 300,400, 500 and 600 ft

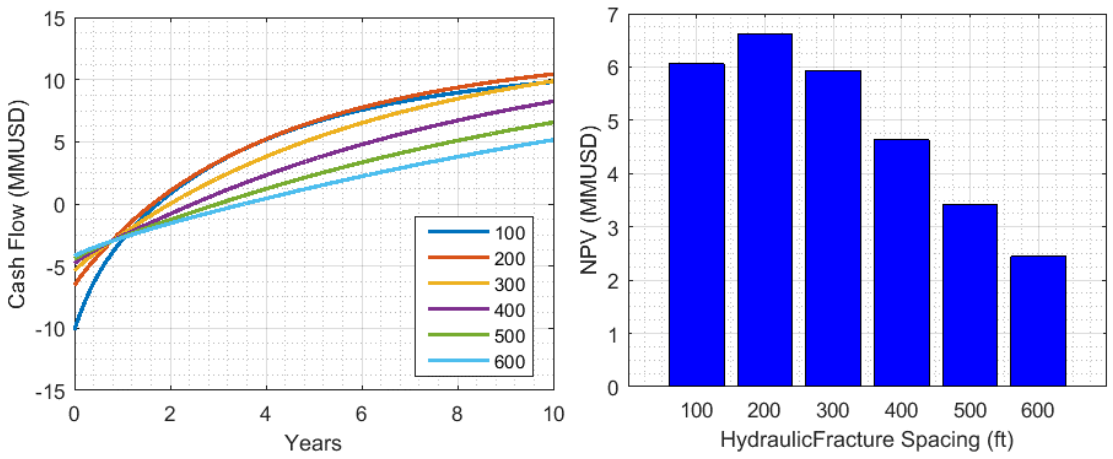

Figure 6.20: Cash flow and NPV vs. Fracture Spacing: a) cumulative production, b) NPV.

6.6 Summary

The hydraulic fracture network induced by well treatment in shale reservoirs are characterised by their extremely complex geometry that increases the contact between the wellbore and the reservoir creating a large SRV able to maintain acceptable level of production rate.

In this work, DK-LS-LGR technique is used to build a grid to deal with the fracture network complexity in the SRV. A proper relative permeability model was employed which takes into consideration the effect of high capillary pressure on two-phase flow of gas and condensate in the shale matrix. The generated condensate in the matrix is almost immobile while it blocks completely the smaller pores. Hence the gas relative permeability reduces significantly.

A compositional simulation was carried out for ¼ SRV with a constant bottomhole pressure using a commercial software.

Simulation results showed that condensate accumulation starts in the fractures and spread quickly into the nearby matrix due to the low bottomhole pressure. The condensate starts to form in the matrix as the pressure goes below the dew point from the outer zone (layer) which is in direct contact with depressurised fracture. Subsequently the condensate bank expands to the centre of the matrix block as pressure declines.

Even though the effect of condensate banking in shale reservoirs starts to manifest from the first days of production, it reaches a high level of productivity reduction when the condensate envelopes all the matrix block locking the free gas inside. For this simulation case, this phenomenon starts only one year after production meaning that the well stays

under the heavy condensate banking effect almost for its whole life. A comparison of gas-condensate with dry gas revealed that the effect of condensate banking on ultimate production is up to 40%.

Furthermore, as a result of the condensate immobility in the matrix the CGR decreases significantly by 90% after 4 years of production which leads to a condensate recovery factor three times less than the gas recovery factor.

The stress-dependent conductivity of fracture is an important factor in shale well performance evaluation. The reduction of fracture conductivity when the effective pressure increases as the reservoir pressure declines can lead to ultimate production loss of about 10%.

The non-Darcy flow effect on gas flow in fractures due to the high velocity has limited effect on production which can be explained by the low flow rate by SRV compared with high flow rate in conventional hydraulic fractured vertical well.

For the reason that no proven EOR techniques are available yet for shale gas-condensate reservoirs (e.g. gas recycling, CO_2 injection and "huff and puff" technology), well design optimisation is the only way possible to maximise the ultimate production. In addition, since multi-stage hydraulic fracturing represents an important part of the shale wells CAPEX, the hydraulic fracture spacing should be optimised using an economic approach rather than only technical evaluation. For the data set used in this study, results showed a 200 ft hydraulic spacing represents the optimum hydraulic fracture spacing.

CHAPTER 7: CONCLUSIONS AND RECOMMENDATIONS

Firstly, this chapter provides a summary of the research questions and it covers the key findings of this thesis and the main conclusions of the gas-condensate flow modelling in shale reservoirs. The developed models of flow behaviour and phase behaviour of gas-condensate fluids in shale matrix are described briefly and the results obtained from these models are discussed. Secondly, recommendations for the development of shale gas-condensate reservoirs are presented. Finally, the contributions to knowledge by this thesis are briefly presented.

7.1 Research Questions

Shale reservoirs are classified as unconventional reservoirs alongside tight gas sands and Coal Bed Methane (CBM). They are self-sourced reservoirs; the hydrocarbons are generated and stored in the same formation. They are mainly distinguished by their very small pore size leading to very low permeability and relatively low porosity. Only multistage fractured horizontal well can produce significant flow rates.

For shale gas-condensate reservoirs, the situation is more complicated where the high drawdown leads to rapid condensate build-up near the hydraulic fractures in the first months of production. The condensate banking affects the well productivity as the gas relative permeability declines sharply causing even lower recovery factor in comparison with dry gas wells. The condensate banking effect is controlled by phase behaviour and flow behaviour.

Shale wells are located at the top of development cost scale where accurate production prediction and production optimisation are key elements of shale development projects. Better understanding and evaluation of flow behaviour and phase behaviour is essential to build an accurate reservoir engineering tools.

7.1.1 Condensate effect on Knudsen Flow

In shale matrix, the gas flow in nanoscale pores deviates from conventional continuum Darcy flow to slip flow and transition flow, referred to as Knudsen flow. The Knudsen flow enhances the gas permeability and it is highly dependent on pore size and pore pressure.

The condensate saturation in shale gas-condensate reservoirs adds to the complexity of the problem because of the variation of pore size ranges available for gas flow as the condensate saturation varies with pressure. Currently, no models are available to describe the Knudsen flow of gas-condensate two-phase in shale matrix. Using the dry gas Knudsen flow models can lead an overestimation of the enhanced permeability by Knudsen flow and the ultimate recovery.

7.1.2 Phase Behaviour Deviation

The high capillary pressure induced by the very small pore size in shale matrix affects the phase behaviour of gas-condensate fluids. The pressure difference between gas and condensate (resulted from the capillary forces) generates the increase of dew point and condensate saturation in the reservoir compared to bulk conditions. This can aggravate the condensate banking effect. This phase behaviour deviation is dependent on pore size; different pore sizes exhibits different phase behaviour deviation.

The phase behaviour deviation of gas-condensate fluids is normally modelled using an average pore radius which can lead to inaccurate results. This modelling approach does not reflect the contribution of different pore sizes to the shale matrix phase behaviour according to their volumes. A more accurate modelling of pore size distribution effect on phase behaviour of gas-condensate fluids in shale matrix is needed.

7.2 Key Findings and Conclusions

On account of the research questions mentioned above, the key findings and conclusions of this thesis are discussed in the following Section.

7.2.1 Gas-Condensate Two-phase Knudsen Flow Modelling

In this work, 3D network model was used to evaluate gas flow in shale matrix under condensate banking effect using a log-normal pore size distribution. The apparent gas conductance model proposed by Bespoke and Karniadakis (1999) was used to describe Knudsen flow in single nano-pores. The network gas and condensate rates were used to estimate the permeability correction factor of shale matrix.

For gas condensate systems, the evaluation of Knudsen flow using pore network models is essential in order to implement: a) the changing flow contribution of pore sizes as a function of pressure; b) the condensate banking effect by eliminating the contribution of lower pore sizes blocked by condensate and its effect on the gas flow in connected higher pore sizes.

All the condensate generated in shale matrix remained trapped due to high capillary pressure. Consequently, only gas can flow in shale matrix below the dew point pressure.

In order to measure the effect of condensate blockage on Knudsen flow, a new parameter was proposed in this work; the "Relative Correction Factor" ξ_{rel} defined as the ratio of ξ_{GC} to ξ_{DG}. ξ_{rel} can be used in reservoir engineering tools to adjust ξ_{DG} as function of pressure and condensate saturation. ξ_{rel} can be easily incorporated to shale gas-condensate reservoir engineering tools in order to calculate the effective gas permeability under condensate banking effect using Equation (3.31).

Results showed that the condensate saturation in shale pores network influences the effect of Knudsen flow on apparent gas permeability. When condensate saturation increases in pore network it occupies the lowest possible range of pore size leaving only the upper range accessible by dry gas. As a result, the relative correction factor ξ_{rel} declines.

In addition, this work demonstrated that the relative correction factor ξ_{rel} is not only dependent on condensate saturation but also on reservoir pressure. This is caused by the effect of pressure on the contribution of the different pore size ranges in the Knudsen enhanced permeability. Thus, the effect of condensate banking on Knudsen flow is controlled by the reservoir pressure. A general formulation of ξ_{rel} as a function of condensate saturation and pressure was proposed in Equation (3.39).

Besides, varying the parameters of pore size distribution in terms of mean ν and standard deviation s indicated a stronger dependency of ξ_{rel} on standard deviation s compared to the mean parameter ν. The standard deviation s controls the dispersion of pore size distribution hence it controls the variation of the contribution of the different pore size ranges to the macro Knudsen flow. Accordingly, at higher s values the effect of condensate blocking the lower pore size ranges on Knudsen flow is more pronounced than at lower s values.

To describe this relationship between condensate saturation and Knudsen flow effect, shale porous media must be represented as a pore size distribution rather than a bundle of nanotubes with single pore size. Consequently, reservoir engineering tools for shale gas condensate reservoirs have to be equipped with fit for purpose models capable of describing the pore size distribution and its effect on the condensate saturation and Knudsen flow.

7.2.2 Phase Behaviour Deviation with Pore Size Distribution Modelling

The phase behaviour deviation of gas-condensate in shale matrix was investigated using Peng-Robinson EOS (Equation of State) and Parachor IFT (Interfacial Tension) model at the pore level. Numerical CVD (Constant Volume Depletion) experiments on individual nanotube showed a high dependency of phase behaviour deviation in terms of dew point pressure and condensate saturation on pore radius. The lower the pore radius the higher the deviation of dew point and condensate saturation from conventional phase behaviour.

Accordingly, at constant pore radius, the closer the reservoir temperature and pressure to the critical point in phase envelope the lower the phase behaviour deviation as the IFT decrease at the critical point.

In order to evaluate the phase behaviour deviation of gas-condensate fluids in shale matrix, a VLE model was proposed in this work capable of describing the interaction between the different pore radii and how they affect the macro phase behaviour. This model is a Connected Pore Space Model (CPSM) where condensate is assumed to start to form at the dew point in the smallest pore and then moves to the next free smallest pore as the saturation increases. It incorporates an iterative algorithm for the calculation of the equilibrium of thermodynamic forces and capillary forces interpreted as gas-condensate composition and volumes and interface pore radius respectively.

Results of CVD experiments revealed that phase behaviour deviation is more important in lean condensate fluids than rich condensate fluids. Lean condensate with lower maximum yield (compared to rich condensate) exhibits higher condensate saturation deviation as the IFT is higher at low pore interface radii. Furthermore, comparison of CPSM results with single nanotube with average radius indicated that describing shale porous media with single pore radius can underestimate the phase behaviour deviation.

7.2.3 Effect of Nanopores on Matrix Deliverability

The effects of flow behaviour deviation and phase behaviour deviation of gas condensate fluids in shale matrix were evaluated using a semi-analytical model of a single matrix block. The model assumes a constant fracture pressure and it covers both transient and pseudo-steady states in the matrix block.

Due to reduction of gas permeability in the matrix by the condensate banking in shale matrix, the well productivity is reduced by up to 30%. Thus, the development of this type of shale resources is considered challenging compared to oil and dry gas shale reservoirs.

Knudsen flow enhancement of gas apparent permeability contributes significantly to the ultimate recovery. The data set used in this work showed a production increase of 30%. It partially alleviated the production loss induced by condensate banking. Knudsen flow should be considered in reservoir engineering calculation in order to not underestimate the well potential. Nevertheless, the assumption of dry gas flow when modelling Knudsen enhanced permeability without correcting the apparent permeability to the condensate banking effect on Knudsen flow can lead to an overestimation (about 20%) of the production gain by Knudsen flow. Hence, the use of the Relative Correction Factor, ξ_{rel} proposed in this thesis is necessary to assess more accurately the effect of condensate banking on the performance of shale gas-condensate wells.

On the other hand, even though it was illustrated in Chapter 4 that the condensate saturation in shale matrix increases under capillary forces effect (compared to bulk conditions), the effect of this increase on cumulative production is insignificant (2.5 - 5%).

7.2.4 Shale Gas-Condensate Well Performance

The performance of shale gas-condensate wells was investigated with the use of 3D numerical simulation. The DK-LS-LGR technique was used to model the complexity of fracture network and its interaction with the shale matrix. A compositional simulation was carried out for ¼ SRV with a constant bottomhole pressure using a commercial software.

Numerical simulation results showed although the effect of condensate banking starts to manifest from the first production days/weeks, it reduces the well productivity significantly when all matrix blocks in the SRV are enveloped in condensate banking. In the example treated in this work, the full condensate banking effect starts after one year of production and continues during the rest of well life with reduction of 40% in production compared to a dry gas well.

Additionally, numerical simulations indicated that the non-Darcy flow effect on gas flow in fractures due to the high velocity has limited effect on production. The gas low flow rate in a single hydraulic fracture is relatively lower than gas rates experienced in conventional hydraulic fractured vertical well. Moreover, the stress-dependent conductivity of fracture should always be considered in shale well performance evaluation. The reduction of fracture conductivity due to the reservoir pressure decline can reduce considerably the ultimate production.

The gas-condensate reservoirs have been produced under natural decline mechanisms as no proven pressure maintenance or CO_2 injection techniques have been developed. The only way that gas-condensate asset value can be maximised is through well design optimisation.

Hydraulic fracture spacing is a key element of optimisation as the fracturing consists of a significant part of the well CAPEX. For the example presented in this work, it was concluded that a 200 ft hydraulic spacing allows for minimum condensate banking with maximum NPV (Net Present Value).

7.3 Recommendations for Development of Shale Gas-Condensate Reservoirs

The shale reservoirs are different hydrocarbon resources compared to other reservoir types in terms rock fabric, reservoir characteristics. Besides the poor reservoir quality and the high-cost completion techniques faced in shale reservoirs development, condensate banking effect represents a challenge to its commercial exploitation. The success of field development and management projects of gas-condensate reservoirs relies on the appropriate analysis methods, techniques and tools adapted to the shale reservoirs.

The analysis of pore structure and distribution of shale matrix should be a routine practice during exploration and development phases. As demonstrated in this work, the pore distribution has a major effect on the Knudsen flow under condensate banking. Thus, a good characterisation of pore distribution is vital to be able to predict accurately the apparent gas permeability under reservoir conditions in terms of pressure and condensate saturation. This can lead to more accurate production prediction for future wells and performance analysis of producing wells.

Furthermore, due to the high horizontal and vertical heterogeneity in shale reservoirs, targeting sweet spots at early stages can improve the field development outcome through optimisation of well location and fracture spacing. The pore size distribution should be considered as one of the sweet spot factors; the lower the standard deviation (dispersion) the lower negative effect of condensate banking on Knudsen flow.

In the absence of reliable multiphase flow experimental procedures, the 3D pore network modelling should be adopted as an alternative of core flooding experiments in order to deduce the flow behaviour of gas-condensate fluids in shale matrix. 3D pore network can be built synthetically from pore size distribution analysis or from pore space imaging.

The finding of this work in relation to Knudsen flow under condensate saturation suggests the use of water-free fracturing fluids rather than water-based fluids is more beneficial. The fracturing water that invades the shale matrix has a similar impact as Knudsen flow by blocking the lowest range of pores hence reducing the enhancement of dry gas permeability

by Knudsen flow. Moreover, the model presented in Equation (3.39) can be used to evaluate the change Knudsen flow effect with variation of the in situ water saturation in the shale matrix.

The well performance of shale gas-condensate reservoir should always be evaluated using compositional reservoir numerical simulation as it is the only available tool capable of dealing with the high degree of complexity of these systems. This complexity is generated by the compositional change of the gas-condensate fluids, the complexity of hydraulic fracture geometries, the matrix-fracture interaction, the transient regime in matrix and the permeability dependency with reservoir pressure decline. Nevertheless, the incorporation of the models for flow behaviour and phase behaviour deviation in shale matrix must be considered in order to capture the physics of gas-condensate flow in shale reservoirs.

7.4 Summary of Contributions to Knowledge

In Chapter 3, the Knudsen flow in shale gas-condensate reservoir is investigated through 3D pore network modelling and the effect of both condensate saturation and pressure was identified and formulated by introducing a new parameter, "*Relative Correction Factor*". A general correlation describing the *Relative Correction Factor* is proposed in Equation (3.39). This equation can be directly integrated to the existing shale reservoir engineering tools (numerical simulators and semi-analytical models). In addition, this thesis demonstrated the significance of the effect the *Relative Correction Factor* reduction on well ultimate recovery.

On the other hand, in 0 this work proposed a new modelling approach of the Vapour Liquid Equilibrium (VLE) of gas-condensate fluids in shale matrix which incorporates the effect of pore size distribution on the phase behaviour deviation caused by the capillary pressure. This model generates more accurate results than the average pore size method (using single tube with average pore radius) where the interaction between the different pore sizes and their contribution to the macro phase behaviour is accounted for. This study concluded that although the deviation of phase behaviour can be observed in matrix but its effect on ultimate recovery is limited.

CHAPTER 8: SUGGESTIONS FOR FUTURE WORK

In this chapter, key suggestion for future research are presented in order to continue the improvement of the understanding and modelling of gas –condensate flow in shale reservoirs.

8.1 Gas-Condensate Flow in Shale Matrix

In Chapter 3, a 3D pore network of nanotube was used to evaluate the gas-condensate flow in shale matrix with random pore size distribution following a log-normal law. The coordination number is constant (6 for all network). However, the coordination number in shale matrix is heterogeneous. In order to improve the network modelling, imaging techniques (such as Scanning Electron Microscopy and Transmission Electron Microscopy) of shale samples can be used to extract more accurate pore network description. This type of pore network models (extracted from imaging techniques) can be used to evaluate the gas-condensate flow and their results can be compared to this work.

In addition, in the pore network only tubes with circular cross-section were used as nanopores in organic matter. However, pores in non-organic matter have slit-like shape with a different capillary pressure-saturation function compared to circular organic nanopores. This limitation can be removed by using imaging techniques results to model the distribution of organic matter and non-organic matter in shale matrix.

While the 3D pore network can give an insight to the nature of multiphase flow of gas-condensate fluids in shale matrix as presented in this work, the direct measurement of relative permeability is still highly required in order to fully understand condensate banking effect on the gas flow in shale reservoirs. The same applies to other multi-phase flow in shale such as oil-water and oil-gas flow. The current core flooding techniques are highly challenging to be applied to the shale samples due to the extremely low permeability and the difficulty of saturation control and measurement. The development of apparatus able to measure directly the relative permeability in shale matrix, through an improved core flooding or alternative techniques is highly recommended for future work. This will not only improve significantly the understanding of the shale gas-condensate well performance

under natural depletion but it will help to develop appropriate enhanced recovery techniques.

8.2 Alternative Flow and Phase Behaviour Modelling

In this work, the Peng-Robinson EOS (Equation of State) was modified by including the effect of the capillary pressure to investigate the phase behaviour deviation of gas-condensate fluids in nanopores. However as mentioned in Section 4.4.2, condensate can occur at negative pressure induced by capillarity which cannot be handled by the equilibrium criteria expressed by Equation (4.2).

Molecular Simulation is a well-established technique in chemical physics, materials science and the biomolecules modelling where thermodynamic interaction of molecule-molecule and molecule-wall can be modelled at the molecular level. Thus, Molecular Simulation should be considered in future as an alternative to investigate the vapour liquid equilibrium of gas-condensate fluids in nanopores. A variety of fluid composition and rock properties should be used to convert the results into simple expressions to be integrated to reservoir simulation tools.

In this thesis, two models DPSM and CPSM were used to investigate the effect of pore size distribution on the phase behaviour deviation assuming no interaction and full interaction between nanopores. Imaging of pore space in organic and inorganic matter in shale matrix showed a non-uniform pore space (e.g. variation of radius in the same pore). This is an important parameter that controls how the condensate generates and accumulates in the pore space under the effect of capillary forces. The Level Set Method (LSM) which is a direct modelling approach to study capillary controlled displacement of fluids in porous media can be used for this purpose in future work (refer to Blunt et al. 2013). However, 3D high resolution models of the pore space at the nano-level must be generated to be able to deploy this method which could be challenging.

The methodology of evaluating the pore size distribution effect on phase behaviour, presented in this work, should be extended to oil shale reservoirs. Using a pore distribution will improve the VLE calculation under bubble point rather than using an average pore size. The oil-gas interface is expected to occur in higher pore radius than the average radius due to the high oil saturation (compared to condensate saturation in gas-condensate systems).

8.3 Effect of Flow and Phase Behaviour Deviation on Well Performance

In Chapter 4, a semi-analytical model was used to analyse the effect of Knudsen flow and phase behaviour deviation. The model was restricted to a single matrix block and constant fracture pressure. In addition, as the condensate remains almost immobile, CVD dynamic properties were used to generate the pseudo-pressure function.

The main challenge of extending the semi-analytical model to include both matrix and fracture is the linking of the two pseudo-pressure functions of matrix and fracture in Laplace domain. The two functions have different relative permeability models and the Knudsen flow existence only in matrix. Alternative mathematical modelling should be explored to be able to integrate matrix and fracture media into one gas-condensate (two-phase) flow model.

Additionally, it is highly recommended to build a 3D dual porosity/dual permeability compositional numerical simulator (or modifying an existing simulator) in order to incorporate the flow behaviour and the phase behaviour deviation. The results of this new (or modified) simulator will shed more light on their effect on the whole system including shale matrix, hydraulic fractures and wellbore.

Likewise, the numerical simulation will allow more accurate interaction between condensate and gas rather than semi-analytical which uses the CVD results. The CVD experiments are carried out at static condition i.e. gas and condensate don't flow during the experiment. However, in the shale matrix, the gas flows from the centre of the matrix block towards the outer layers bringing more heavy components which leads to higher condensate saturation levels than normally observed in CVD experiments. This may result in a more accurate estimation of the effect of phase behaviour deviation on well production than that reported in this work.

8.4 Shale Reservoir Simulation

8.4.1 Unstructured grid

The fracture network used in Chapter 6 has an idealised geometry with uniform matrix blocks and it covers all the SRV. In reality, hydraulic fractures propagate in shale reservoirs as branches with decreasing density away from the wellbore. The effect of non-uniform hydraulic fracture distribution and, as a result, the non-uniformity of matrix block shape through the SRV should be evaluated and compared against the uniform fracture network. This can be achieved by using micro-seismic mapping data to generate a high-resolution

unstructured grid for numerical simulation. This type of gridding could be applied for all shale wells including oil, dry gas and gas-condensate.

8.4.2 Dynamic Gridding

The fine gridding makes the numerical simulation of full field development studies with multiple shale wells expensive with high investment in computing power and parallel software licenses. The compositional simulation for shale gas-condensate reservoirs adds to the complexity of the problem. Thus, the dynamic gridding should be investigated as a means to reduce the calculation time and computing power needed for full field numerical simulation. The dynamic gridding can decrease the number of active cells as a function of time and pressure propagation in the reservoir.

8.5 Enhanced Recovery

As mentioned previously, reliable enhanced recovery techniques for shale gas-condensate reservoirs are still to be developed. In this work, all well performance calculation was carried out with the assumption of natural depletion. The relatively high development cost of shale reservoirs should be considered when dealing with enhanced recovery techniques. The economic context and the specificity of each shale play will be decisive for the enhanced recovery projects.

In conventional reservoirs, dry gas or CO_2 recycling techniques have been used successfully to increase the recovery of gas-condensate wells. Nevertheless, for shale reservoir, this technique should be investigated to evaluate its applicability. The low permeability in the shale matrix limits the direct contact between the condensate in the matrix and the injected dry gas or CO_2 in the fracture. Thus, a longer shut-in phase (soak) will be needed than in conventional reservoir to allow the condensate to evaporate. Laboratory experiments and field pilot project should be designed and executed to evaluate the cycle duration and the production gain.

REFERENCES

AL HINAI, A. et al., 2014. Comparisons of pore size distribution: a case from the Western Australian gas shale formations. *Journal of Unconventional Oil and Gas Resources,* 8, pp. 1-13

ALEXANDER, T., BAIHLY, J., BOYER, C., CLARK, B. and JOCHEN, V., 2011. Shale Gas Revolution. *Oilfield Review,* 3, p. 40-50

ARPS, J., 1945. Analysis of decline curves. *Transactions of the AIME,* 160(01), pp. 228-247

ARTHUR, J.D., BOHM, B. and LAYNE, M., 2009. Hydraulic fracturing considerations for natural gas wells of the Marcellus Shale.

ASADI, M., et al, 2015. Water-Free Fracturing: A Case History. In: *SPE/CSUR Unconventional Resources Conference.* 20-22 October 2015. Calgary, Alberta, Canada. Society of Petroleum Engineers.

BARENBLATT, G., ZHELTOV, I.P. and KOCHINA, I., 1960. Basic concepts in the theory of seepage of homogeneous liquids in fissured rocks [strata]. *Journal of Applied Mathematics and Mechanics,* 24(5), pp. 1286-1303

BARNUM, R., et al, 1995. Gas condensate reservoir behaviour: productivity and recovery reduction due to condensation. In: *SPE Annual Technical Conference and Exhibition.* 22-25 October 1995. Dallas, Texas. Society of Petroleum Engineers.

BELHAJ, H., et al, 2003. Numerical and experimental modeling of non-Darcy flow in porous media. In: *SPE Latin American and Caribbean Petroleum Engineering Conference.* 27-30 April 2003. Port-of-Spain, Trinidad and Tobago. Society of Petroleum Engineers.

BELLO, R.O. and WATTENBARGER, R.A., 2010. Multi-stage hydraulically fractured horizontal shale gas well rate transient analysis. In: *North Africa technical conference and exhibition.* 14-17 February. Cairo, Egypt Society of Petroleum Engineers.

BERTONCELLO, A., et al, 2014. Imbibition and water blockage in unconventional reservoirs: well management implications during flowback and early production. In: *SPE/EAGE European Unconventional Resources Conference and Exhibition.* 25-27 February 2014. Vienna, Austria.

BESKOK, A. and KARNIADAKIS, G.E., 1999. Report: a model for flows in channels, pipes, and ducts at micro and nano scales. *Microscale Thermophysical Engineering,* 3(1), pp. 43-77

BIOT, M.A., 1941. General theory of three-dimensional consolidation. *Journal of Applied Physics,* 12(2), pp. 155-164

BLUNT, M.J., 2001. Flow in porous media—pore-network models and multiphase flow. *Current opinion in colloid & interface science,* 6(3), pp. 197-207

BLUNT, M.J. et al., 2013. Pore-scale imaging and modelling. *Advances in Water Resources,* 51, pp. 197-216

BROWN, M. and OZKAN, E., 2009. Practical Solutions for Pressure Transient Responses of Fractured Horizontal Wells in Unconventional Reservoirs. Paper SPE 125043 presented at the SPE Annual Technical Conference and Exhbition, New Orleans, LA, 04-07 October. *Bull.US Bureau of Mines,* 228

BRUSILOVSKY, A.I., 1992. Mathematical simulation of phase behavior of natural multicomponent systems at high pressures with an equation of state. *SPE reservoir engineering,* 7(1), pp. 117-122

BUSTOS, C.I. and TOLEDO, P.G., 2003. Pore-level modeling of gas and condensate flow in two-and three-dimensional pore networks: Pore size distribution effects on the relative permeability of gas and condensate. *Transport in Porous Media,* 53(3), pp. 281-315

BYBEE, K., 2006. Non-Darcy flow in hydraulic fractures. *Journal of Petroleum Technology,* 58(03), pp. 58-59

CARMAN, P.C., 1956. *Flow of gases through porous media.* Academic press.

CIPOLLA, C.L. et al., 2010. Reservoir modeling in shale-gas reservoirs. *SPE reservoir evaluation & engineering,* 13(04), pp. 638-653

CIVAN, F., 2010. Effective correlation of apparent gas permeability in tight porous media. *Transport in Porous Media,* 82(2), pp. 375-384

CIVAN, F., 2010. A review of approaches for describing gas transfer through extremely tight porous media. In: *AIP Conference Proceedings.* 20–25 June 2010. Montecatini, Italy.

CIVAN, F., RAI, C.S. and SONDERGELD, C.H., 2011. Shale-gas permeability and diffusivity inferred by improved formulation of relevant retention and transport mechanisms. *Transport in Porous Media,* 86(3), pp. 925-944

CLUFF, R.M. and BYRNES, A.P., 2010. Relative Permeability In Tight Gas Sandstone Reservoirs-The" Permeability Jail" Model. In: *SPWLA 51st Annual Logging Symposium.* 19-23 June 2010. Perth, Australia Society of Petrophysicists and Well-Log Analysts.

COOKE, C., 1973. Conductivity of fracture proppants in multiple layers. *Journal of Petroleum Technology,* 25(09), pp. 1,101-1,107

COPIC, D., 2008. *A MEMS Knudsen pump for high gas flow applications.* ProQuest.

CROUSSE, L.C., et al, 2015. Unconventional Shale Pore System Characterization in El Trapial Area, Vaca Muerta, Argentina. In: 20-22 July 2015. San Antonio, Texas, USA. Unconventional Resources Technology Conference (URTEC).

CUI, X., BUSTIN, A. and BUSTIN, R.M., 2009. Measurements of gas permeability and diffusivity of tight reservoir rocks: different approaches and their applications. *Geofluids,* 9(3), pp. 208-223

CURTIS, M.E., AMBROSE, R.J. and SONDERGELD, C.H., 2010. Structural characterization of gas shales on the micro-and nano-scales. In: *Canadian Unconventional Resources and International Petroleum Conference.* 19-21 October 2010. Calgary, Alberta, Canada. Society of Petroleum Engineers.

DANESH, A., 1998. *PVT and phase behaviour of petroleum reservoir fluids.* Elsevier.

DU, Y., GUAN, L. and BAI, B., 2004. Well Deliverability Loss Analysis in the Gas Condensate Reservoir. In: *Canadian International Petroleum Conference.* 8-10 June 2004. Calgary, Alberta. Petroleum Society of Canada.

ECONOMIDES, M.J. et al., 2000. *Reservoir stimulation.* Wiley Chichester.

ECONOMIDES, M.J. andWANG, X., 2010. Design flaws in hydraulic fracturing. In: *SPE International Symposium and Exhibiton on Formation Damage Control.* 10-12 February 2010. Lafayette, Louisiana, USA. Society of Petroleum Engineers.

EIA, 2010. *EIA 2010 eagle ford play map.* [online] Available from: http://www.eia.gov/maps/pdf/EIA%20Eagle%20Ford%20Play%20update%2012-29-14.pdf

EIA, 2011. *Trends in eagle ford drilling highlight the search for oil and natural gas liquids.* [online] Available from: http://www.eia.gov/todayinenergy/detail.cfm?id=3770

EIA, 2014. *Shale oil and shale gas resources are globally abundant.* [online] Available from: http://www.eia.gov/todayinenergy/detail.cfm?id=14431

EIA, 2015. *U.S. crude oil and natural gas proved reserves.* [online] Available from: https://www.eia.gov/naturalgas/crudeoilreserves/ 2016]

EIA, 2016. *Shale in the united states.* [online] US Energy Information Administration. Available from: http://www.eia.gov/energy_in_brief/article/shale_in_the_united_states.cfm [Accessed 4/9 2016]

EL-BANBI, A.H. andWATTENBARGER, R.A., 1998. Analysis of linear flow in gas well production. In: *SPE Gas Technology Symposium.* 15-18 March. Calgary, Alberta, Canada. Society of Petroleum Engineers.

ESHKALAK, M.O., et al, 2014. Enhanced gas recovery by CO2 sequestration versus re-fracturing treatment in unconventional shale Gas reservoirs. In: *Abu Dhabi International Petroleum Exhibition and Conference.* 10-13 November 2014. Abu Dhabi, UAE Society of Petroleum Engineers.

ESPÓSITO, R., TAVARES, F. and CASTIER, M., 2005. Phase equilibrium calculations for confined fluids, including surface tension prediction models. *Brazilian Journal of Chemical Engineering,* 22(1), pp. 93-104

ESTES, R.K. and FULTON, P.F., 1956. Gas slippage and permeability measurements. *Journal of Petroleum Technology,* 8(10), pp. 69-73

FAN, L., THOMPSON, J.W. and ROBINSON, J.R., 2010. Understanding gas production mechanism and effectiveness of well stimulation in the Haynesville Shale through reservoir simulation. In: *Canadian Unconventional Resources and International Petroleum Conference.* Society of Petroleum Engineers.

FANG, F., et al, 1996. A Phenomenological modeling of critical condensate saturation. In: *SPE Annual Technical Conference and Exhibition.* Society of Petroleum Engineers.

FATT, I., 1956. The network model of porous media. 2. Dynamic properties of a single size tube network. *Transactions of the American institute of mining and metallurgical engineers,* 207(7), pp. 160-163

FEVANG, Ø and WHITSON, C.H., 1996. Modeling Gas-Condensate Well Deliverability. 11(4), pp. 221-221-230

FIRINCIOGLU, T., OZKAN, E. and OZGEN, C., 2012. Thermodynamics of Multiphase Flow in Unconventional Liquids-Rich Reservoirs. In: *SPE Annual Technical Conference and Exhibition.*

FIROOZABADI, A. and KATZ, D.L., 1988. Surface tension of reservoir crudeoil/gas systems recognizing the asphalt in the heavy fraction. *SPE Reservoir Engineering,* 3(01), pp. 265-272

FISHER, M.K., et al, 2002. Integrating fracture mapping technologies to optimize stimulations in the Barnett Shale. In: *SPE Annual Technical Conference and Exhibition.* Society of Petroleum Engineers.

FISHER, M. et al., 2004. *Optimizing Horizontal Completion Techniques in the Barnett Shale Using Microseismic Fracture Mapping.Paper SPE 90051 presented at the SPE Annual Technical Conference and Exhibition held in Houston, Texas, USA, 26-29 September 2004,*

FLEWELLING, S.A., TYMCHAK, M.P. and WARPINSKI, N., 2013. Hydraulic fracture height limits and fault interactions in tight oil and gas formations. *Geophysical Research Letters,* 40(14), pp. 3602-3606

FONSECA, E.R. and FARINAS, M.J., 2013. Hydraulic Fracturing Simulation Case Study and Post Frac Analysis in the Haynesville Shale. In: *SPE Hydraulic Fracturing Technology Conference.* Society of Petroleum Engineers.

FREEMAN, C., et al, 2012. Measurement, Modeling, and Diagnostics of Flowing Gas Composition Changes in Shale Gas Wells. In: *SPE Latin America and Caribbean Petroleum Engineering Conference.*

FULTON, P.F., 1951. The effect of gas slippage on relative permeability measurements. *Producers Monthly,* 15(12), pp. 14-19

GALLEGOS, T.J. and VARELA, B., 2015. *Trends in hydraulic fracturing distributions and treatment fluids, additives, proppants, and water volumes applied to wells drilled in the United States from 1947 through 2010: Data analysis and comparison to the literature,*

GLORIOSO, J. and RATTIA, A., 2012. Unconventional Reservoirs: Basic Petrophysical Concepts for Shale Gas. SPE Paper 153004. *Society of Petroleum Engineers, Richardson, Texas,*

GOGOTSI, Y., LIBERA, J.A. and YOSHIMURA, M., 2000. Hydrothermal synthesis of multiwall carbon nanotubes. *Journal of Materials Research,* 15(12), pp. 2591-2594

GÜNTHER, A. and JENSEN, K.F., 2006. Multiphase microfluidics: from flow characteristics to chemical and materials synthesis. *Lab on a Chip,* 6(12), pp. 1487-1503

HALLIBURTON, 2016a. *Eagle ford shale – an emerging gas play.* [online] Available from: http://www.halliburton.com/en-US/ps/solutions/unconventional-resources/shale-gas-oil/shale-plays/eagleford.page?node-id=hgjyd46z [Accessed Jan/19 2016]

HALLIBURTON, 2016b. *Fracturing fluids disclosure.* [online] Available from: http://www.halliburton.com/public/projects/pubsdata/hydraulic_fracturing/fluids_disclosure.html

HAVENS, J. and BATZLE, M., 2011. Minimum horizontal stress in the Bakken formation. In: *45th US Rock Mechanics/Geomechanics Symposium.* American Rock Mechanics Association.

HINCHMAN, S. and BARREE, R., 1985. Productivity loss in gas condensate reservoirs. In: *SPE Annual Technical Conference and Exhibition.* Society of Petroleum Engineers.

HUANG, X., BANDILLA, K.W. and CELIA, M.A., 2016. Multi-Physics Pore-Network Modeling of Two-Phase Shale Matrix Flows. *Transport in Porous Media,* 111(1), pp. 123-141

HUGHES, J.D., 2014. Drilling Deeper: A Reality Check on US Government Forecasts for a Lasting Tight Oil & Shale Gas Boom. *Santa Rosa, California: Post Carbon Institute,*

JAMIOLAHMADY, M. et al., 2000. A mechanistic model of gas-condensate flow in pores. *Transport in Porous Media,* 41(1), pp. 17-46

JANICEK, J.D. and KATZ, D.L.V., 1955. Applications of unsteady state gas flow calculations.

JAVADPOUR, F., 2009. Nanopores and apparent permeability of gas flow in mudrocks (shales and siltstone). *Journal of Canadian Petroleum Technology,* 48(8), pp. 16-21

JIN, Z. and FIROOZABADI, A., 2015. Thermodynamic modeling of phase behavior in shale media. *SPE Journal,*

JOEKAR-NIASAR, V. and HASSANIZADEH, S., 2012. Analysis of fundamentals of two-phase flow in porous media using dynamic pore-network models: a review. *Critical Reviews in Environmental Science and Technology,* 42(18), pp. 1895-1976

JONES, S., 1987. Using the inertial coefficient, b, to characterize heterogeneity in reservoir rock. In: *SPE Annual Technical Conference and Exhibition.* Society of Petroleum Engineers.

JOSHI, G., et al, 2015. Direct TOC Quantification in unconventional Kerogen-rich Shale Resource Play from Elemental Spectroscopy Measurements: A Case Study from North Kuwait. In: *SPE Middle East Unconventional Resources Conference and Exhibition.* Society of Petroleum Engineers.

JUN, H. and KEGANG, L., 2014. A New Method to Determine Biot Coefficients of Bakken Samples. American Rock Mechanics Association. In: *US Rock Mechanics / Geomechanics Symposium.* Minneapolis, MN, USA

KANFAR, M. and WATTENBARGER, R., 2012. Comparison of Empirical Decline Curve Methods for Shale Wells. In: *SPE Canadian Unconventional Resources Conference.* Society of Petroleum Engineers.

KAZEMI, H., 1969. Pressure transient analysis of naturally fractured reservoirs with uniform fracture distribution. *Society of petroleum engineers Journal,* 9(04), pp. 451-462

KING, G.E., 2014. 60 Years of Multi-Fractured Vertical, Deviated and Horizontal Wells: What Have We Learned? In: *SPE Annual Technical Conference and Exhibition.* Society of Petroleum Engineers.

KLINKENBERG, L., 1941. The permeability of porous media to liquids and gases. In: *Drilling and production practice.* American Petroleum Institute.

KOLODZIE JR, S., 1980. Analysis of pore throat size and use of the Waxman-Smits equation to determine OOIP in Spindle Field, Colorado. In: *SPE Annual Technical Conference and Exhibition.* Society of Petroleum Engineers.

KOROS, W. and FLEMING, G., 1993. Membrane-based gas separation. *Journal of Membrane Science,* 83(1), pp. 1-80

KUILA, U., 2013. *Measurement and interpretation of porosity and pore-size distribution in mudrocks: The hole story of shales.* Colorado School of Mines.

KURTOGLU, B., COX, S.A. and KAZEMI, H., 2011. Evaluation of Long-Term Performance of Oil Wells in Elm Coulee Field. In: *Canadian Unconventional Resources Conference.* Society of Petroleum Engineers.

KUUSKRAA, V. et al., 2011. *World shale gas resources: an initial assessment of 14 regions outside the United States.* Washington, DC, USA.: US Department of Energy.

KWON, O. et al., 2001. Permeability of Wilcox shale and its effective pressure law. *Journal of Geophysical Research: Solid Earth,* 106(B9), pp. 19339-19353

LEE, S. and CHIEN, M., 1984. A new multicomponent surface tension correlation based on scaling theory. In: *SPE Enhanced Oil Recovery Symposium.* Society of Petroleum Engineers.

LEWIS, R., et al, 2013. NMR T2 distributions in the Eagle Ford shale: Reflections on pore size. In: *SPE Unconventional Resources Conference-USA.* Society of Petroleum Engineers.

LEWIS, R., et al, 2004. New evaluation techniques for gas shale reservoirs. In: *Reservoir symposium.* Citeseer.

LI, D. and ENGLER, T.W., 2001. Literature review on correlations of the non-Darcy coefficient. In: *SPE Permian Basin Oil and Gas Recovery Conference.* Society of Petroleum Engineers.

LI, K. and FIROOZABADI, A., 2000. Phenomenological modeling of critical condensate saturation and relative permeabilities in gas/condensate systems. *SPE Journal,* 5(02), pp. 138-147

LOPEZ-HERNANDEZ, H., VALKO, P. and PHAM, T., 2004. Optimum Fracture Treatment Design Minimizes the Impact of Non-Darcy Flow Effects. Paper SPE 90195 presented at the SPE Annual Technical Conference and Exhibition, Houston, 26–29 September. *Society of Petroleum Engineers,*

LOYALKA, S. and HAMOODI, S., 1990. Poiseuille flow of a rarefied gas in a cylindrical tube: solution of linearized Boltzmann equation. *Physics of Fluids A: Fluid Dynamics (1989-1993),* 2(11), pp. 2061-2065

LUFFEL, D., HOPKINS, C. and SCHETTLER JR, P., 1993. Matrix permeability measurement of gas productive shales. In: *SPE Annual Technical Conference and Exhibition.* Society of Petroleum Engineers.

MAHADEVAN, J., SHARMA, M.M. and YORTSOS, Y.C., 2007. Capillary wicking in gas wells. *SPE Journal,* 12(04), pp. 429-437

MARTIN, J.J., 1979. Cubic equations of state-which? *Industrial & Engineering Chemistry Fundamentals,* 18(2), pp. 81-97

MARTINS, J., MILTON-TAYLER, D. and LEUNG, H., 1990. The effects of non-Darcy flow in propped hydraulic fractures. In: *SPE Annual Technical Conference and Exhibition.* Society of Petroleum Engineers.

MATTIA, D. and GOGOTSI, Y., 2008. Review: static and dynamic behavior of liquids inside carbon nanotubes. *Microfluidics and Nanofluidics,* 5(3), pp. 289-305

MAXWELL, S. et al., 2002. Microseismic imaging of fracture complexity in the Barnett Shale: SPE 77440.

MEHMANI, A., PRODANOVIĆ, M. and JAVADPOUR, F., 2013. Multiscale, multiphysics network modeling of shale matrix gas flows. *Transport in Porous Media,* 99(2), pp. 377-390

NELSON, B., et al, 2014. Predicting Long-term Production Behavior of the Marcellus Shale. In: *SPE Western North American and Rocky Mountain Joint Meeting.* Society of Petroleum Engineers.

NOJABAEI, B., JOHNS, R.T. and CHU, L., 2013. Effect of capillary pressure on phase behavior in tight rocks and shales. *SPE Reservoir Evaluation & Engineering,* 16(03), pp. 281-289

NUR, A. and YILMAZ, O., 1985. Pore pressure in fronts in fractured rock systems. *Dept.of Geophysics, Stanford U., Stanford, CA,*

ONDARÇUHU, T. and AIMÉ, J., 2013. *Nanoscale Liquid Interfaces: Wetting, Patterning and Force Microscopy at the Molecular Scale.* CRC Press.

ORANGI, A., et al, 2011. Unconventional shale oil and gas-condensate reservoir production, impact of rock, fluid, and hydraulic fractures. In: *SPE Hydraulic Fracturing Technology Conference.* Society of Petroleum Engineers.

PANG, J., et al, 2013. Effect of Porous Media on Saturation Pressures of Shale Gas and Shale Oil. In: *IPTC 2013: International Petroleum Technology Conference.*

PASSEY, Q. et al., 2010. From oil-prone source rock to gasproducing reservoir—geologic and petrophysical characterization of shale-gas reservoirs: SPE 131350.

PATEL, N.C. and TEJA, A.S., 1982. A new cubic equation of state for fluids and fluid mixtures. *Chemical Engineering Science,* 37(3), pp. 463-473

PATEL, P., et al, 2014. Analysis of US Hydraulic Fracturing Fluid System and Proppant Trends. In: *SPE Hydraulic Fracturing Technology Conference.* Society of Petroleum Engineers.

PEARSON, K., 2012. *Geologic models and evaluation of undiscovered conventional and continuous oil and gas resources: Upper Cretaceous Austin Chalk,*

PENG, D. and ROBINSON, D.B., 1976. A new two-constant equation of state. *Industrial & Engineering Chemistry Fundamentals,* 15(1), pp. 59-64

PURSELL, D. and BLAKELEY, D., 1988. Laboratory Investigation of Inertial Flow in High-Strength Fracture Proppants. In: *SPE Annual Technical Conference and Exhibition.* Society of Petroleum Engineers.

RAGHAVAN, R. and CHIN, L., 2002. Productivity changes in reservoirs with stress-dependent permeability. In: *SPE Annual Technical Conference and Exhibition.* Society of Petroleum Engineers.

RASSENFOSS, S., 2013. In search of the waterless fracture. *Journal of Petroleum Technology,* 65(06), pp. 46-54

REDLICH, O. and KWONG, J.N., 1949. On the thermodynamics of solutions. V. An equation of state. Fugacities of gaseous solutions. *Chemical reviews,* 44(1), pp. 233-244

RENO, G.J. and KATZ, D.L., 1943. Surface tension of n-heptane and n-butane containing dissolved nitrogen. *Industrial & Engineering Chemistry,* 35(10), pp. 1091-1093

RODRIGUEZ, L., et al, 2015. Quantitative and Comparative Evaluation of Mineralogy and TOC Analysis from Cores, Cuttings and Logs in Vaca Muerta Unconventional Shale Play. In: *Unconventional Resources Technology Conference.* Society of Petroleum Engineers.

ROSE, W.D., 1948. Permeability and gas-slippage phenomena. *28th Annual Mtg.Topical Committee on Production Technology,*

ROSS, D.J. and BUSTIN, R.M., 2009. The importance of shale composition and pore structure upon gas storage potential of shale gas reservoirs. *Marine and Petroleum Geology,* 26(6), pp. 916-927

RUBIN, B., 2010. Accurate simulation of non Darcy flow in stimulated fractured shale reservoirs. In: *SPE Western Regional Meeting.* Society of Petroleum Engineers.

RUSHING, J., NEWSHAM, K. and FRAASSEN, K., 2003. Measurement of the two-phase gas slippage phenomenon and its effect on gas relative permeability in tight gas sands. In: *SPE Annual Technical Conference and Exhibition.*

RUTQVIST, J. et al., 2002. A modeling approach for analysis of coupled multiphase fluid flow, heat transfer, and deformation in fractured porous rock. *International Journal of Rock Mechanics and Mining Sciences,* 39(4), pp. 429-442

SAIDIAN, M., 2014. Porosity and pore size distribution in mudrocks: a comparative study for Haynesville, Niobrara, Monterey, and Eastern European Silurian Formations. In: Unconventional Resources Technology Conference (URTEC).

SAMPATH, K. and KEIGHIN, C.W., 1982. Factors affecting gas slippage in tight sandstones of cretaceous age in the Uinta basin. *Journal of Petroleum Technology,* 34(11), pp. 2,715-2,720

SCHECHTER, D. and GUO, B., 1998. Parachors based on modern physics and their uses in IFT prediction of reservoir fluids. *SPE Reservoir Evaluation & Engineering,* 1(03), pp. 207-217

SCHMIDT, G. and WENZEL, H., 1980. A modified van der Waals type equation of state. *Chemical Engineering Science,* 35(7), pp. 1503-1512

SCHÖN, J., 2011. Rocks—Their Classification and General Properties. *Handbook of Petroleum Exploration and Production,* 8, pp. 1-16

SHAW, J., 2011. Benefits and application of a surface controlled sliding sleeve for frac applications. In: *SPE Annual Technical Conference and Exhibition.* Society of Petroleum Engineers.

SHENG, J.J., 2015. Increase liquid oil production by huff-n-puff of produced gas in shale gas condensate reservoirs. *Journal of Unconventional Oil and Gas Resources,* 11, pp. 19-26

SIGMUND, P. et al., 1973. Retrograde condensation in porous media. *Old SPE Journal,* 13(2), pp. 93-104

SILIN, D., 2011. Pore-scale mechanisms of gas flow in tight sand reservoirs. *Lawrence Berkeley National Laboratory,*

SOAVE, G., 1972. Equilibrium constants from a modified Redlich-Kwong equation of state. *Chemical Engineering Science,* 27(6), pp. 1197-1203

SOBOLEV, V. et al., 2000. Surface tension and dynamic contact angle of water in thin quartz capillaries. *Journal of colloid and interface science,* 222(1), pp. 51-54

SPEIGHT, J.G., 2013. *Shale gas production processes.* Gulf Professional Publishing.

STALGOROVA, K. and MATTAR, L., 2013. Analytical model for unconventional multifractured composite systems. *SPE Reservoir Evaluation & Engineering,* 16(03), pp. 246-256

STECKELMACHER, W., 1986. Knudsen flow 75 years on: the current state of the art for flow of rarefied gases in tubes and systems. *Reports on Progress in Physics,* 49(10), pp. 1083

STEHFEST, H., 1970. Algorithm 368: Numerical inversion of Laplace transforms [D5]. *Communications of the ACM,* 13(1), pp. 47-49

TAS, N.R. et al., 2003. Capillarity induced negative pressure of water plugs in nanochannels. *Nano Letters,* 3(11), pp. 1537-1540

TEK, M., COATS, K. and KATZ, D., 1962. The effect of turbulence on flow of natural gas through porous reservoirs. *Journal of Petroleum Technology,* 14(07), pp. 799-806

TEXAS RRC, *Texas RRC - public GIS viewer.* [online] Available from: http://wwwgisp.rrc.state.tx.us/GISViewer2/ 2016]

TIAB, D. and DONALDSON, E.C., 2015. *Petrophysics: theory and practice of measuring reservoir rock and fluid transport properties.* Gulf professional publishing.

TORRES, L., YADAV, O.P. and KHAN, E., 2016. A review on risk assessment techniques for hydraulic fracturing water and produced water management implemented in onshore unconventional oil and gas production. *Science of The Total Environment,* 539, pp. 478-493

TUCKER, M.E., 2009. *Sedimentary petrology: an introduction to the origin of sedimentary rocks.* John Wiley & Sons.

UNIVERSITY OF KENTUCKY, *Shales and fireclays.* [online] Available from: http://www.uky.edu/KGS/pubs/SappCoreBook

VENGOSH, A. et al., 2014. A critical review of the risks to water resources from unconventional shale gas development and hydraulic fracturing in the United States. *Environmental science & technology,* 48(15), pp. 8334-8348

WANG, F.P. andREED, R.M., 2009. Pore networks and fluid flow in gas shales. In: *SPE Annual Technical Conference and Exhibition.* Society of Petroleum Engineers.

WANG, Q. et al., 2014. Natural gas from shale formation–the evolution, evidences and challenges of shale gas revolution in United States. *Renewable and Sustainable Energy Reviews,* 30, pp. 1-28

WARREN, J. and ROOT, P.J., 1963. The behavior of naturally fractured reservoirs. *Society of Petroleum Engineers Journal,* 3(03), pp. 245-255

WASAKI, A. and AKKUTLU, I.Y., 2015. Permeability of organic-rich shale. *SPE Journal,*

WILLIAMS, K.E., 2012. PS The Permeability of Overpressure Shale Seals and of Source Rock Reservoirs is the Same.

WU, Q. et al., 2014. Optic imaging of two-phase-flow behavior in 1D nanoscale channels. *SPE Journal,* 19(05), pp. 793-802

ZHAO, J., YANG, H. and LI, Y., 2013. China developing strategy for horizontal fracturing technology. *Oil & Gas Journal,* 111(7), pp. 70-70

ZHAO, T., et al, 2015. TOC estimation in the Barnett Shale from triple combo logs using support vector machine. In: *2015 SEG Annual Meeting.* Society of Exploration Geophysicists.

ZIARANI, A.S. and AGUILERA, R., 2012. Knudsen's permeability correction for tight porous media. *Transport in Porous Media,* 91(1), pp. 239-260

ZOLFAGHARI, A., et al, 2015. Advances in Flowback Chemical Analysis of Gas Shales. In: *SPE Annual Technical Conference and Exhibition.* Society of Petroleum Engineers.

APPENDIX A: INPUT DATA FILE OF NUMERICAL SIMULATION - ECLIPSE E300

```
-----------------------------------------------------------------------
-- 1/4 SRV
-----------------------------------------------------------------------
RUNSPEC
TITLE
1/4 SRV
DIMENS
    181    121   1  /
WATER
ISGAS
FIELD
COMPS
5/
FULLIMP
EQLDIMS
    1  100    2    1   20 /
TABDIMS
    2    1   100   100    2  /
REGDIMS
    1    1    1*  1*  1*    1  /
WELLDIMS
    5   13    1    2 /
START
  1 'JAN' 2015  /
HWELLS
UNIFOUT
--NOSIM
GRID      ================================================================
INIT
INCLUDE
'F:/ECLIPSE PHD/Eclipse/V3/FILES/DXV_Dx100.INC'/
INCLUDE
'F:/ECLIPSE PHD/Eclipse/V3/FILES/DYV_Dx100.INC'/
DZ
21901*300 /
TOPS
21901*6000 /
PERMX
21901*50e-6/
PORO
21901*0.08/
INCLUDE
'F:/ECLIPSE PHD/Eclipse/V3/FILES/BOX_10_CF20.TXT'/
COPY
PERMX PERMY/
PERMX PERMZ/
/
-------------------------------
BOX
122 181  1 121  1 1/
ACTNUM
20328*0/
ENDBOX
BOX
1 181  38 121  1 1/
ACTNUM
20328*0/
ENDBOX
EDIT
```

```
PROPS     ================================================================
INCLUDE
'F:/ECLIPSE PHD/Eclipse/V3/FILES/GC@370K.pvo'/
INCLUDE
'F:/ECLIPSE PHD/Eclipse/V3/FILES/RELPERM1.INC'/
ROCK
 1.01325  0 /
GRAVITY
    40.0000             0.99000           0.678 /
PVTW
-- Pressure (bar)      Bw        Cw          Ug      du/dp
    1.034           1.00370    0    .60700    0.00E+00 /
REGIONS ========================================================
INCLUDE
'F:/ECLIPSE PHD/Eclipse/V3/FILES/SATNUM.TXT'/
INCLUDE
'F:/ECLIPSE PHD/Eclipse/V3/FILES/FIPNUM.TXT'/

SOLUTION   ================================================================
--- depth press   oil-water   pcow    gas-oil  pcgo  black  N  type
RPTRST
BASIC=3 FREQ=3 SOIL PRESSURE KRG KRO/
EQUIL
6000    4500   10000     0     10000    0     2*    1*   1  /
--SWAT
--21901*0.2 /
--SGAS
--21901*0.8 /
--PRESSURE
--21901*4500 /
--INCLUDE
--'../FILES/SWAT.TXT'/
SUMMARY    ============================================================
FGIP
FGPT
FGPR
FOPR
FGOR
FOGR
FOIP
FOPT
FPR
FOSAT
-- REGION
RGIP
/
RGPT
/
RGPR
/
ROPR
/
RGOR
/
ROGR
/
RPR
/
RGE
/
ROSAT
/
WGPR
/
WOPR
/
WOGR
/
```

```
WBHP
/

WXMF
'X1' 1 /
'X1' 2 /
'X1' 3 /
'X1' 4 /
'X1' 5 /
/
--BPR
--1 35 1/
RUNSUM
SEPARATE
EXCEL
SCHEDULE   ============================================================
WELSPECS
'X1'  'G'   1  1  1*  'GAS'/
/
COMPDAT
'X1'   1  1 1 1   'OPEN'   0  0  0.583333  0   0.0  0 'X' 0 /
/
-- Production
WCONPROD
'X1' 'OPEN' 'BHP'  5*  500/
/
INCLUDE
'F:/ECLIPSE PHD/Eclipse/V3/FILES/TSTEP.INC'/
END
INCLUDE Files
BOX
1 181 1 1 1 1/
PERMX
181*20/
PORO
181*0.001/
ENDBOX
BOX
1 181 13 13 1 1/
PERMX
181*2/
PORO
181*0.001/
ENDBOX
BOX
1 181 25 25 1 1/
PERMX
181*2/
PORO
181*0.001/
ENDBOX
BOX
1 181 37 37 1 1/
PERMX
181*2/
PORO
181*0.001/
ENDBOX
BOX
1 181 49 49 1 1/
PERMX
181*2/
PORO
181*0.001/
ENDBOX
BOX
1 181 61 61 1 1/
PERMX
```

```
181*2/
PORO
181*0.001/
ENDBOX
BOX
1 181 73 73 1 1/
PERMX
181*2/
PORO

181*0.001/
ENDBOX
BOX
1 181 85 85 1 1/
PERMX
181*10/
PORO
181*0.001/
ENDBOX
BOX
1 181 97 97 1 1/
PERMX
181*2/
PORO
181*0.001/
ENDBOX
BOX
1 181 109 109 1 1/
PERMX
181*2/
PORO
181*0.001/
ENDBOX
BOX
1 181 121 121 1 1/
PERMX
181*2/
PORO
181*0.001/
ENDBOX
------------------------------------------------
BOX
1 1 1 121 1 1/
PERMX
121*2/
PORO
121*0.001/
ENDBOX

BOX
13 13 1 121 1 1/
PERMX
121*2/
PORO
121*0.001/
ENDBOX
BOX
25 25 1 121 1 1/
PERMX
121*2/
PORO
121*0.001/
ENDBOX
BOX
37 37 1 121 1 1/
PERMX
121*2/
PORO
```

```
121*0.001/
ENDBOX
BOX
49 49 1 121 1 1/
PERMX
121*2/
PORO
121*0.001/
ENDBOX
BOX
61 61 1 121 1 1/
PERMX
121*2/
PORO
121*0.001/
ENDBOX
BOX
73 73 1 121 1 1/
PERMX
121*2/
PORO
121*0.001/
ENDBOX
BOX
85 85 1 121 1 1/
PERMX
121*2/
PORO
121*0.001/
ENDBOX
BOX
97 97 1 121 1 1/
PERMX
121*2/
PORO
121*0.001/
ENDBOX
BOX
109 109 1 121 1 1/
PERMX
121*2/
PORO
121*0.001/
ENDBOX
BOX
121 121 1 121 1 1/
PERMX
121*2/
PORO
121*0.001/
ENDBOX
BOX
133 133 1 121 1 1/
PERMX
121*2/
PORO
121*0.001/
ENDBOX
BOX
145 145 1 121 1 1/
PERMX
121*2/
PORO
121*0.001/
ENDBOX
BOX
157 157 1 121 1 1/
PERMX
```

```
121*2/
PORO
121*0.001/
ENDBOX
BOX
169 169 1 121 1 1/
PERMX
121*2/
PORO
121*0.001/
ENDBOX
BOX
181 181 1 121 1 1/
PERMX
121*2/
PORO
121*0.001/
ENDBOX
--------------------------------------------------------------------------------
----------------------------------------
DXV
1      4.396  5.796  7.646  10.086 13.299 17.542 13.299 10.086 7.646  5.796  4.396
1      4.396  5.796  7.646  10.086 13.299 17.542 13.299 10.086 7.646  5.796  4.396
1      4.396  5.796  7.646  10.086 13.299 17.542 13.299 10.086 7.646  5.796  4.396
1      4.396  5.796  7.646  10.086 13.299 17.542 13.299 10.086 7.646  5.796  4.396
1      4.396  5.796  7.646  10.086 13.299 17.542 13.299 10.086 7.646  5.796  4.396
1      4.396  5.796  7.646  10.086 13.299 17.542 13.299 10.086 7.646  5.796  4.396
1      4.396  5.796  7.646  10.086 13.299 17.542 13.299 10.086 7.646  5.796  4.396
1      4.396  5.796  7.646  10.086 13.299 17.542 13.299 10.086 7.646  5.796  4.396
1      4.396  5.796  7.646  10.086 13.299 17.542 13.299 10.086 7.646  5.796  4.396
1      4.396  5.796  7.646  10.086 13.299 17.542 13.299 10.086 7.646  5.796  4.396
1      4.396  5.796  7.646  10.086 13.299 17.542 13.299 10.086 7.646  5.796  4.396
1      4.396  5.796  7.646  10.086 13.299 17.542 13.299 10.086 7.646  5.796  4.396
1      4.396  5.796  7.646  10.086 13.299 17.542 13.299 10.086 7.646  5.796  4.396
1/
--------------------------------------------------------------------------------
----------------------------------------
DYV
1      4.396  5.796  7.646  10.086 13.299 17.542 13.299 10.086 7.646  5.796  4.396
1      4.396  5.796  7.646  10.086 13.299 17.542 13.299 10.086 7.646  5.796  4.396
1      4.396  5.796  7.646  10.086 13.299 17.542 13.299 10.086 7.646  5.796  4.396
1      4.396  5.796  7.646  10.086 13.299 17.542 13.299 10.086 7.646  5.796  4.396
1      4.396  5.796  7.646  10.086 13.299 17.542 13.299 10.086 7.646  5.796  4.396
1      4.396  5.796  7.646  10.086 13.299 17.542 13.299 10.086 7.646  5.796  4.396
1      4.396  5.796  7.646  10.086 13.299 17.542 13.299 10.086 7.646  5.796  4.396
1      4.396  5.796  7.646  10.086 13.299 17.542 13.299 10.086 7.646  5.796  4.396
1      4.396  5.796  7.646  10.086 13.299 17.542 13.299 10.086 7.646  5.796  4.396
1      4.396  5.796  7.646  10.086 13.299 17.542 13.299 10.086 7.646  5.796  4.396
1      4.396  5.796  7.646  10.086 13.299 17.542 13.299 10.086 7.646  5.796  4.396
1      4.396  5.796  7.646  10.086 13.299 17.542 13.299 10.086 7.646  5.796  4.396
1      4.396  5.796  7.646  10.086 13.299 17.542 13.299 10.086 7.646  5.796  4.396
1      4.396  5.796  7.646  10.086 13.299 17.542 13.299 10.086 7.646  5.796  4.396
1/
--------------------------------------------------------------------------------
----------------------------------------
ECHO
-- Units: F
RTEMP
--
-- Constant Reservoir Temperature
--
         310
/

EOS
```

```
--
-- Equation of State (Reservoir EoS)
--
   PR3
/

NCOMPS
--
-- Number of Components
--
       8
/
PRCORR
--
-- Modified Peng-Robinson EoS
--
CNAMES
--
-- Component Names
--
   'C1+'
   'C2+'
   'C3+'
   'C4+'
   'NC4+'
   'NC5+'
   'C5+'
   'C8+'
/
MW
--
-- Molecular Weights (Reservoir EoS)
--
         16.043
          30.07
         44.097
         58.124
         58.124
         72.151
   80.4474962852898
   138.414661265984
/

OMEGAA
--
-- EoS Omega-a Coefficient (Reservoir EoS)
--
   0.457235529
   0.457235529
   0.457235529
   0.457235529
   0.457235529
   0.457235529
   0.457235529
   0.457235529
/

OMEGAB
--
-- EoS Omega-b Coefficient (Reservoir EoS)
--
   0.077796074
   0.077796074
   0.077796074
   0.077796074
   0.077796074
   0.077796074
   0.077796074
```

```
   0.077796074
/

-- Units: R
TCRIT
--
-- Critical Temperatures (Reservoir EoS)
--
        343.08
       549.774
        665.64
        734.58
        765.36
        845.28
   879.833934552316
   1115.43516941397
/

-- Units: psia
PCRIT
--
-- Critical Pressures (Reservoir EoS)
--
   667.78169597908
   708.342379977809
   615.75820998071
   529.052399983426
   550.655372982749
   488.785633984687
   483.3915458675
   368.36609540811
/

-- Units: ft3 /lb-mole
VCRIT
--
-- Critical Volumes (Reservoir EoS)
--
   1.56980902280093
   2.37073199361773
   3.20369188326721
   4.21285482649638
   4.08470715116569
   4.98174087848051
   5.33469120413819
   8.7540339422573
/

ZCRIT
--
-- Critical Z-Factors (Reservoir EoS)
--
   0.284729476628582
   0.284634795100356
   0.276164620041118
   0.28273695875079
   0.273855549100576
   0.268438914149838
   0.273120392161015
   0.269395317521124
/

SSHIFT
--
-- EoS Volume Shift (Reservoir EoS)
--
   -0.144265618878948
   -0.103268354016888
```

```
   -0.0775013814750784
   -0.0619837251487845
   -0.0542248969856375
   -0.0302778964820975
   -0.029248003030088
   0.0269664054127404
/

ACF
--
-- Acentric Factors (Reservoir EoS)
--
         0.013
        0.0986
        0.1524
        0.1848
         0.201
         0.251
   0.253150360024959
   0.446411529282408
/

BIC
--
-- Binary Interaction Coefficients (Reservoir EoS)
--
       0
       0       0
       0       0       0
       0       0       0       0
       0       0       0       0       0
       0       0       0       0       0       0
 0.0406496616630927    0.01    0.01       0       0       0       0
/

PARACHOR
--
-- Component Parachors
--
            77
           108
         150.3
         181.5
         189.9
         231.5
   252.383346210996
   394.027687006592
/

-- Units: ft3 /lb-mole
VCRITVIS
--
-- Critical Volumes for Viscosity Calc (Reservoir EoS)
--
   1.56980902280093
   2.37073199361773
   3.20369188326721
   4.21285482649638
   4.08470715116569
   4.98174087848051
   5.33469120413819
   8.7540339422573
/

ZCRITVIS
--
-- Critical Z-Factors for Viscosity Calculation (Reservoir EoS)
--
```

```
   0.284729476628582
   0.284634795100356
   0.276164620041118
   0.28273695875079
   0.273855549100576
   0.268438914149838
   0.273120392161015
   0.269395317521124
/

LBCCOEF
--
-- Lorentz-Bray-Clark Viscosity Correlation Coefficients
--
    0.1023 0.023364 0.058533 -0.040758 0.0093324
/

ZI
--
-- Overall Composition
--
       0.68722
       0.08337
        0.0467
       0.01045
       0.01825
       0.00791
       0.02019
       0.12591
/
------------------------------------------------------------------------------
SGOF
--Sg   Krg    Krog   Pcog
0      0      0      0
0.08   0.0000001    0      0
0.16   0.0000128    0      0
0.24   0.0002187    0      0
0.32   0.0016384    0      0
0.4    0.0078125    0      0
0.48   0.0279936    0      0
0.56   0.0823543    0      0
0.64   0.2097152    0      0
0.72   0.4782969    0      0
0.8    1      0      0 /
0      0      1      0
1      1      0      0 /

SWOF
--Sw   Krw    Krow   Pcow
0.2    3.34E-49     0      0
0.28   0.001  0      0
0.36   0.008  0      0
0.44   0.027  0      0
0.52   0.064  0      0
0.6    0.125  0      0
0.68   0.216  0      0
0.76   0.343  0      0
0.84   0.512  0      0
0.92   0.729  0      0
1      1      0      0 /
0      0      1      0
1      1      0      0 /
------------------------------------------------------------------------------
------------------------------------------
BOX                                       ENDBOX
1 181 1 1 1 1/                            BOX
SATNUM                                    1 181 13 13 1 1/
181*2/                                    SATNUM
```

```
181*2/
ENDBOX
BOX
1 181 25 25 1 1/
SATNUM
181*2/
ENDBOX
BOX
1 181 37 37 1 1/
SATNUM
181*2/
ENDBOX
BOX
1 181 49 49 1 1/
SATNUM
181*2/
ENDBOX
BOX
1 181 61 61 1 1/
SATNUM
181*2/
ENDBOX
BOX
1 181 73 73 1 1/
SATNUM
181*2/
ENDBOX
BOX
1 181 85 85 1 1/
SATNUM
181*2/
ENDBOX
BOX
1 181 97 97 1 1/
SATNUM
181*2/
ENDBOX
BOX
1 181 109 109 1 1/
SATNUM
181*2/
ENDBOX
BOX
1 181 121 121 1 1/
SATNUM
181*2/
ENDBOX
------------------------------------
------------
BOX
1 1 1 121 1 1/
SATNUM
121*2/
ENDBOX
BOX
13 13 1 121 1 1/
SATNUM
121*2/
ENDBOX
BOX
25 25 1 121 1 1/
SATNUM
121*2/
ENDBOX
BOX
37 37 1 121 1 1/
SATNUM
121*2/
ENDBOX
BOX
49 49 1 121 1 1/
SATNUM
121*2/
ENDBOX
BOX
61 61 1 121 1 1/
SATNUM
121*2/
ENDBOX
BOX
73 73 1 121 1 1/
SATNUM
121*2/
ENDBOX
BOX
85 85 1 121 1 1/
SATNUM
121*2/
ENDBOX
BOX
97 97 1 121 1 1/
SATNUM
121*2/
ENDBOX
BOX
109 109 1 121 1 1/
SATNUM
121*2/
ENDBOX
BOX
121 121 1 121 1 1/
SATNUM
121*2/
ENDBOX
BOX
133 133 1 121 1 1/
SATNUM
121*2/
ENDBOX
BOX
145 145 1 121 1 1/
SATNUM
121*2/
ENDBOX
BOX
157 157 1 121 1 1/
SATNUM
121*2/
ENDBOX
BOX
169 169 1 121 1 1/
SATNUM
121*2/
ENDBOX
BOX
181 181 1 121 1 1/
SATNUM
121*2/
ENDBOX
------------------------------------
------------------------------------
------------------------------------
------------
BOX
1 181 1 1 1 1/
FIPNUM
```

```
181*2/
ENDBOX
BOX
1 181 13 13 1 1/
FIPNUM
181*2/
ENDBOX
BOX
1 181 25 25 1 1/
FIPNUM
181*2/
ENDBOX
BOX
1 181 37 37 1 1/
FIPNUM
181*2/
ENDBOX
BOX
1 181 49 49 1 1/
FIPNUM
181*2/
ENDBOX
BOX
1 181 61 61 1 1/
FIPNUM
181*2/
ENDBOX
BOX
1 181 73 73 1 1/
FIPNUM
181*2/
ENDBOX
BOX
1 181 85 85 1 1/
FIPNUM
181*2/
ENDBOX
BOX
1 181 97 97 1 1/
FIPNUM
181*2/
ENDBOX
BOX
1 181 109 109 1 1/
FIPNUM
181*2/
ENDBOX
BOX
1 181 121 121 1 1/
FIPNUM
181*2/
ENDBOX
------------------------------------
------------
BOX
1 1 1 121 1 1/
FIPNUM
121*2/
ENDBOX
BOX
13 13 1 121 1 1/
FIPNUM
121*2/
ENDBOX
BOX
25 25 1 121 1 1/
FIPNUM
121*2/
ENDBOX
BOX
37 37 1 121 1 1/
FIPNUM
121*2/
ENDBOX
BOX
49 49 1 121 1 1/
FIPNUM
121*2/
ENDBOX
BOX
61 61 1 121 1 1/
FIPNUM
121*2/
ENDBOX
BOX
73 73 1 121 1 1/
FIPNUM
121*2/
ENDBOX
BOX
85 85 1 121 1 1/
FIPNUM
121*2/
ENDBOX
BOX
97 97 1 121 1 1/
FIPNUM
121*2/
ENDBOX
BOX
109 109 1 121 1 1/
FIPNUM
121*2/
ENDBOX
BOX
121 121 1 121 1 1/
FIPNUM
121*2/
ENDBOX
BOX
133 133 1 121 1 1/
FIPNUM
121*2/
ENDBOX
BOX
145 145 1 121 1 1/
FIPNUM
121*2/
ENDBOX
BOX
157 157 1 121 1 1/
FIPNUM
121*2/
ENDBOX
BOX
169 169 1 121 1 1/
FIPNUM
121*2/
ENDBOX
BOX
181 181 1 121 1 1/
FIPNUM
121*2/
ENDBOX
------------------------------------
------------------------------------
```

```
-----------------------------------
------------
TSTEP
0.00001
1.22018E-06
1.36907E-06
1.53612E-06
1.72356E-06
1.93386E-06
2.16983E-06
2.43459E-06
2.73165E-06
3.06496E-06
3.43895E-06
3.85856E-06
4.32938E-06
4.85764E-06
5.45036E-06
6.11541E-06
6.8616E-06
7.69884E-06
8.63825E-06
9.69227E-06
1.08749E-05
1.22018E-05
1.36907E-05
1.53612E-05
1.72356E-05
1.93386E-05
2.16983E-05
2.43459E-05
2.73165E-05
3.06496E-05
3.43895E-05
3.85856E-05
4.32938E-05
4.85764E-05
5.45036E-05
6.11541E-05
6.8616E-05
7.69884E-05
8.63825E-05
9.69227E-05
0.000108749
0.000122018
0.000136907
0.000153612
0.000172356
0.000193386
0.000216983
0.000243459
0.000273165
0.000306496
0.000343895
0.000385856
0.000432938
0.000485764
0.000545036
0.000611541
0.00068616
0.000769884
0.000863825
0.000969227
0.001087491
0.001220185
0.00136907
0.001536121
0.001723556
0.001933862
0.002169829
0.002434588
0.002731653
0.003064965
0.003438947
0.003858562
0.004329378
0.004857642
0.005450364
0.006115409
0.006861602
0.007698844
0.008638245
0.00969227
0.010874906
0.012201845
0.013690696
0.015361213
0.017235565
0.019338622
0.02169829
0.024345882
0.027316529
0.03064965
0.034389473
0.038585623
0.043293781
0.048576422
0.054503641
0.061154092
0.068616019
0.07698844
0.08638245
0.096922703
0.108749062
0.122018454
0.136906957
0.153612133
0.172355648
0.193386218
0.216982905
0.243458824
0.273165293
0.3064965
0.343894729
0.385856232
0.432937813
0.485764216
0.545036415
0.611540916
0.686160193
0.769884399
0.863824503
0.969227034/
RPTRST
BASIC=3 FREQ=3 SOIL PRESSURE KRG
KRO/
TSTEP
1.087490619
1.220184543
1.369069575
1.536121328
1.723556478
1.933862176
2.169829049
2.434588236
2.731652929
```

```
3.064964998                              13.69069575
3.438947289                              15.36121328
3.858562322                              17.23556478
4.329378132                              19.33862176
4.85764216                               21.69829049
5.450364148                              24.34588236
6.115409156                              27.31652929
6.861601929                              30*124
7.69884399                               28.81135685/
8.638245034                              ------------------------------------
9.692270341                              ------------------------------------
10.87490619                              -
12.20184543
```

APPENDIX B: ABSTRACTS OF PUBLISHED AND SUBMITTED PAPERS

SPE Journal

Modelling of Gas-Condensate Flow in Shale Matrix

Journal:	*SPE Journal*
Manuscript ID	SJ-0616-0013
Manuscript Type:	Technical Paper
Date Submitted by the Author:	09-Jun-2016
Complete List of Authors:	Labed, Ismail; Robert Gordon University, School of Engoneering Oyeneyin, Mufutau; The Robert Gordon University, School of Engineering Oluyemi, Gbenga; Robert Gordon University, School of Engineering
Keywords:	Shale Reservoirs, Gas-condensate, Knudsen Flow, Condensate Banking

Abstract

Condensate banking is the most challenging engineering problem in gas-condensate reservoirs development where condensate accumulation in the reservoirs reduces dramatically the gas permeability resulting into loss of well productivity. Assessment of condensate banking effect is important to predict well productivity and to diagnose well performance.

Traditionally, Darcy law combined with relative permeability models have been used for modelling of condensate banking effect in conventional reservoirs; this approach is also widely adopted in reservoir engineering commercial tools. However, for shale gas-condensate reservoirs, the gas flow deviates from Darcy flow to micro-flow known as Knudsen flow due to the very small pore size in shale matrix (3-300 nm) compared to conventional reservoirs (10 -200 μm). This gas flow is highly dependent on pore size distribution and reservoir pressure.

In this paper, the effect of condensate saturation on Knudsen flow in shale matrix kerogen is investigated using a 3D pore network with a random pore size distribution. The Knudsen flow is incorporated at the pore level and gas permeability is evaluated for the whole network. In addition, the pore distribution effect in terms of log-normal median and standard deviation is investigated. The concept of relative permeability in Darcy flow is

extended to Knudsen flow by defining a new parameter called relative correction factor ξ_{rel} in order to evaluate the effect of condensate banking on Knudsen flow. This parameter can be employed directly in reservoir engineering tools.

Simulation results showed that the relative correction factor is not only dependent on condensate saturation but also on pressure. This is due to the impact of pressure on the contribution of pore size ranges into the gas flow. In addition, results showed the effect of pore size distribution where the standard deviation controls mainly the behaviour of Knudsen flow under condensate saturation. Disregarding this effect can lead to an overestimation of Knudsen flow contribution in well production under condensate banking effect.

SPE-175475-MS

Hydraulic Fracture Spacing Optimisation for Shale Gas-Condensate Reservoirs Development

Ismail Labed, Babs Oyeneyin, and Gbenga Oluyemi, Robert Gordon University

This paper was prepared for presentation at the SPE Offshore Europe Conference & Exhibition held in Aberdeen, Scotland, UK, 8–11 September 2015.

Abstract

Condensate banking is one of the most challenging problems in shale gas exploitation as it acts as flow choke around hydraulic fractures reducing the drainage of shale matrix. Thus, fracture spacing optimisation is a key element of shale gas and condensate field development. For shale gas reservoirs, more accurate models are needed to describe the gas-condensate flow in the shale matrix where the flow mechanism and phase behaviour are different from those of conventional reservoirs.

In this paper, new models developed for flow behaviour and phase behaviour to estimate well productivity as function of time are presented. The Knudsen flow was used to model apparent gas permeability in shale matrix as a function of pressure and pore size distribution. A modified Peng-Robinson EOS was used to evaluate the condensate saturation in the matrix under capillary pressure effect. A semi-analytical well model was also developed to evaluate well productivity under constant pressure.

The results show substantial difference and impact with the application of Knudsen flow when compared with conventional Darcy law. Using conventional Darcy flow **instead** of Knudsen flow for gas-condensate reservoir development can lead to a underestimation of well production up to 30%. Although capillary pressure has an effect on phase behaviour its impact on well production is insignidficant.

This study shows the importance of using flow behaviour deviation model in well completion optimisation for shale gas-condensate fields. Using conventional flow models can undermine the economic viability of gas-condensate shale reservoirs by underestimation of optimum fracture spacing.